

INFRARED TRANSMITTANCE STUDY OF GaAs: MAPPING
STRESS, DISLOCATION, AND EL2 DISTRIBUTIONS

Paolo Dobrilla
Laurea in Fisica, University of Milan, Italy, 1980

A dissertation submitted to the faculty
of the Oregon Graduate Center
in partial fulfillment of the
requirements for the degree
Doctor of Philosophy
in
Applied Physics

April, 1986

The dissertation "Infrared transmittance study of GaAs: mapping stress, dislocation, and EL2 distributions" by Paolo Dobrilla has been examined and approved by the following Examination Committee:

John S. Blakemore, Thesis Advisor
Professor

Wallace B. Leigh
Assistant Professor

Thomas M. Loehr
Professor

Richard Y. Koyama
Adjunct Associate Professor

ACKNOWLEDGMENTS

Recognition is due to a number of individuals and companies that have made this project possible.

Richard Reynolds, director of the Defense Science Office (DARPA), first gave the impetus to undertake the kind of measurements here described.

The members of my SPC and of my thesis committee have been invaluable in their guidance and stimulation.

John Blakemore has been both a friend and a supervisor. His intellectual ingenuity and deep knowledge have been an inexhaustible source of inspiration.

Russ Kremer and Wally Leigh, with different degrees of loquacity, have helped me with advice, good judgement, and scientific insight.

During this project I have occasionally asked for the assistance of almost everybody in the Department of Applied Physics and Engineering. All have been extremely responsive, but special thanks are due to Fred Holmes, Dick Elliott, John Hunt, Jack Biles and Don Emmons.

Farzin Amzajerjian has kindly tried to impose a

reasonable schedule to my lunches.

A number of companies have provided me with the samples used in this work: Cominco Ltd., Spectrum Technology Inc., Aracor, and Westinghouse.

Richard Koyama, of TriQuint, has played the double role of supplier of samples and welcome critic of the methodology and results. His suggestions and comments have always been more than useful.

Finally I should recognize the efficient but costly services of AT&T that have enabled my wife Mariarosa and me to be always in touch despite the great distance between us. Her loving attention has never failed during this period.

This work has been supported by the National Science Foundation through Grant DMR-8305731.

TABLE OF CONTENTS

	Page
ACKNOWLEDGMENTS.....	iii
LIST OF TABLES.....	vii
LIST OF FIGURES.....	viii
ABSTRACT.....	xii
Chapter	
1. INTRODUCTION.....	1
References.....	14
2. EXPERIMENTAL TECHNIQUES.....	18
A. Introduction.....	18
B. EL2 mapping.....	20
C. Stress mapping.....	34
D. Infrared transmittance mapping system.....	46
E. Vapor phase KOH dislocation etch.....	61
F. Etch pit density evaluation.....	66
G. Dislocation mapping.....	70
References.....	80
3. DISLOCATION, STRESS AND EL2 DISTRIBUTIONS.....	84
A. Introduction.....	84
B. Stress and dislocation distributions.....	85
C. EL2 distribution.....	109
References.....	137

Chapter	Page
4. EL2, DISLOCATIONS AND DEVICES.....	139
A. Introduction.....	139
B. Experimental procedures and results.....	141
C. Discussion.....	152
References.....	157
5. CONCLUSIONS.....	159
References.....	163
VITA.....	165

List of Tables

Table	Page
I: Refractive index, normal reflectance, and transmittance for various optical densities of a GaAs slab.....	28
II: List of graphic symbols used in the EL2 or transmittance maps.....	57
III: Stress information for sequences of wafers cut from two different ingots.....	93

List of Figures

FIGURE	PAGE
1-1: Carrier density and electrical conductivity of GaAs vs. Fermi energy position.....	3
1-2: EL2 map.....	6
1-3: Dislocation map.....	8
1-4: Stress contour map.....	11
2-1: GaAs refractive index vs. photon energy.....	23
2-2: GaAs spectral reflectivity and maximum transmittance.....	24
2-3: EL2 absorption cross-section vs. photon energy.....	33
2-4: Stress-induced birefringence maps.....	39
2-5: Polarization vectors in a birefringent crystal.....	40
2-6: Mechanism for stress-induced interference within the exploring beam.....	45
2-7: IR transmittance mapping system.....	47
2-8: Schematic of the IR mapping system.....	49
2-9: EL2 map, screen of APPLE II monitor.....	55
2-10: EL2 map, hard copy.....	56
2-11: EL2 maps from different systems.....	58
2-12: EL2 maps from different systems.....	59
2-13: Etch pits on GaAs, after etching in molten KOH.....	62

FIGURE	PAGE
2-14: Etch pit density vs. micrograph exposure time.....	68
2-15: Macrographs of etched GaAs wafers.....	71
2-16: Macrograph and dislocation map of an etched sample.....	73
2-17: Evaluation of the resolving power of the dislocation mapping technique.....	75
2-18: Cellular structure of dislocations.....	76
2-19: A/B produced etch pits.....	79
3-1: Stress components in a LEC-grown ingot.....	88
3-2: Experimental and theoretical stress contours.....	90
3-3: Stress contours.....	95
3-4: Stress contours.....	96
3-5: Stress and dislocation maps.....	98
3-6: Dislocation maps.....	99
3-7: Stress map.....	101
3-8: Stress maps.....	102
3-9: Dislocation map.....	103
3-10: Stress and dislocation maps.....	105
3-11: Stress map.....	106
3-12: Stress and dislocation maps.....	107
3-13: EL2 concentration plot.....	110

FIGURE	PAGE
3-14: EL2 concentration vs. As fraction in the melt.....	112
3-15: EL2 maps.....	113
3-16: EL2 and ingot radius profiles.....	115
3-17: EL2 maps.....	117
3-18: EL2 map.....	119
3-19: Cooling cycle of an LEC ingot.....	121
3-20: EL2 maps.....	123
3-21: Dislocation lineages.....	124
3-22: EL2 map.....	125
3-23: Stress and EL2 maps.....	129
3-24: Dislocation and EL2 maps.....	130
3-25: Dislocation and EL2 maps.....	131
3-26: EL2 maps.....	133
3-27: EL2 maps.....	134
3-28: EL2 maps.....	135
4-1: Dislocation, EL2, and threshold voltage maps for the same GaAs wafer.....	143
4-2: Set of micrographs of an etched wafer, indicating an uniform dislocation distribution.....	145
4-3: EL2, threshold voltage, and saturation current maps for the wafer of Fig. 4-2.....	146
4-4: Scatter plots of threshold voltage and saturation current vs. EL2 concentration.....	147

FIGURE	PAGE
4-5: X-ray topograph and EL2 distribution for an In-doped GaAs wafer.....	149
4-6: Threshold voltage and saturation current maps for devices built in wafer of Fig. 4-5.....	150
4-7: Threshold voltage vs. EL2 concentration.....	151

ABSTRACT

Infrared Transmittance Study of GaAs: Mapping Stress, Dislocation and EL2 Distributions

Paolo Dobrilla, Ph.D.

Oregon Graduate Center, 1986

Supervising Professor: John S. Blakemore

Semi-insulating (SI) GaAs is currently the object of active investigation due to its applications in microwave and digital technology. The SI status of "undoped" GaAs derives from the electrical compensation of acceptors by an intrinsic donor labeled EL2. Thus the material uniformity is expected to depend, among other parameters, on the EL2 spatial fluctuations.

GaAs substrates used in the integrated circuit industry are usually grown by the liquid encapsulated Czochralski (LEC) method, and are heavily dislocated. Dislocations may affect the electrical uniformity of the substrates either directly or indirectly, acting as sinks and sources for EL2.

Because of the high cost of SI GaAs, it is appropriate

to develop nondestructive techniques to evaluate the uniformity of the material and the relations between different parameters such as EL2 and dislocations.

High resolution transmittance measurements of GaAs wafers of customary thickness (0.5 mm) have been performed in this study to gain knowledge of the EL2 concentration and its spatial distribution in the material. A computer controlled system has been originally developed to map the EL2 distribution inferring its local concentration from transmittance data in the 0.95-1.1 μm range. The same experimental set-up has then been used to map nondestructively the residual stress in the wafers, as well as to get qualitative information about the dislocation pattern in chemically etched wafers.

Stress in LEC grown GaAs crystals produce dislocations and may even lead to the cracking of the ingot. While the stress distribution is usually destructively deduced from the dislocation pattern, the measurement system here developed makes it possible to detect nondestructively weak photoelastic interferograms equivalent to contours of equal stress. These measurements have provided the first experimental verification of theoretical thermoelastic

models of the stress distribution in LEC ingots.

More than a hundred GaAs wafers from various commercial suppliers have been mapped, and the results of this study can be summarized as follows: (a) in only about 50% of the samples the EL2 and stress/dislocation distributions are qualitatively similar in that they have the same four-fold crystallographic symmetry; (b) these extrinsic parameter distributions appear to be independent, since each can be individually detected in the absence of the other; (c) in the presence of linear clusters of dislocations, commonly known as lineages, enhanced EL2 can be found segregated about them.

The spatial coincidence of EL2 and dislocations makes it difficult to differentiate the effect they individually have on devices built in GaAs substrates. A few wafers, whose EL2 and dislocation patterns were known to be different, have been processed to yield arrays of field effect transistors (FETs). The results suggest that EL2 fluctuations, rather than dislocation nonuniformities, are responsible for the electrical inhomogeneity of FETs implanted in SI GaAs substrates.

CHAPTER 1

INTRODUCTION

Undoped, semi-insulating (SI) gallium arsenide (GaAs) is acquiring great importance because of the role it may play in the future development of the integrated circuit (IC) industry. When SI GaAs is used as a substrate for the fabrication of ICs it is possible to obtain good intrinsic device insulation and low interconnecting capacitance. Together with the high electron mobility of GaAs, these features allow high clock rates in digital ICs and provide high frequency capabilities for analog devices.

The high resistivity of undoped GaAs is due to the electrical compensation of the main acceptor level, carbon, by a deep donor labelled EL2. Shallower acceptor and donor levels are present in smaller concentrations and have a much less important effect on the Fermi level, which is then locked at the EL2 midgap level (-0.8 eV below the conduction band). This position of the Fermi level, as indicated in

Fig. 1-1, induces a very low carrier concentration in the material, and hence its high resistivity.

The identity of EL2 is not yet fully established. It can be said nevertheless that EL2 is clearly an intrinsic defect and not an impurity since, for example, it can be created by implantation of different ions [1,2]. All available data indicate that the EL2 concentration (N_{EL2}) is increased by a nonstoichiometric As excess during crystal growth [3-9]. As a result, it is generally assumed that EL2 is associated with the As antisite defect As_{Ga} [3,10,11], which is an As atom occupying the site of a Ga atom. Despite this general agreement, some results are reported [12], which make this identification not yet firm. Furthermore, some aspects of EL2, such as its photoquenching behavior [13], cannot be understood if one assumes it is composed exclusively of the As_{Ga} defect.

The GaAs extrinsic optical absorption related to EL2 was identified by Martin [13] in 1981, and the calibration of the absorption coefficient with respect to the defect concentration was also given. Another calibration curve was later proposed [14], which agrees with the first one in shape and is in tolerable numerical agreement also.

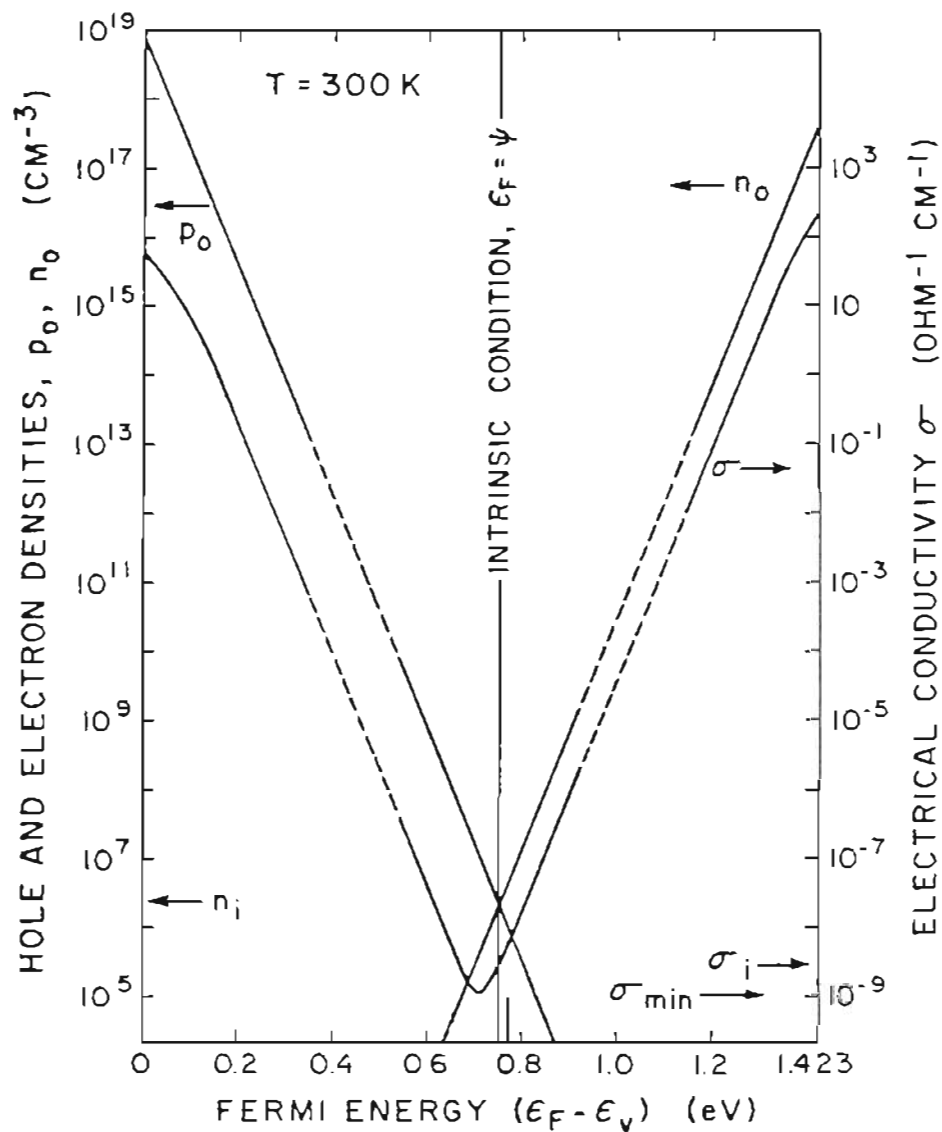


Figure 1-1: Concentration of carriers and resulting conductivity in GaAs as a function of the Fermi level position. The EL2 level, responsible for the low conductivity of nominally undoped GaAs, is indicated.

Some researchers [e.g. 15,16] have utilized this absorption band to reveal the local concentration of the defect by transmittance measurements in the near-infrared. They did not attempt to correlate the EL2 distribution with other electrical parameters of the material, and no correlation of N_{EL2} with device characteristics built in SI substrates was possible either, due to the thickness (~5 mm) of the slabs used to investigate the EL2 distribution.

The successful development of ICs in SI GaAs substrates requires crystals that are extremely uniform with respect to all relevant parameters. Among such parameters, this work initially dealt only with the spatial uniformity of EL2, detecting its local concentration by optical absorption measurements in SI GaAs wafers of thickness customary for IC processing (0.5 mm). The original calibration by Martin [13] was and still is used, as in most investigations of EL2 based on optical absorption methods.

The detection of EL2 in the volume of a 2" or 3" diameter wafer of thickness ranging from 350 to 650 μm is a challenging problem, because of the very small optical density of such a sample. In many cases the mean transmittance is only 1% lower than the maximum set by

reflection losses alone; a good resolution of local changes of the EL2 content, which itself may be constant within 10% of the mean value, requires a discrimination of 0.1% variations of the mean transmittance. The required spatial resolution, about 0.5 mm, calls for a sequential scanning over about 2,000 points on the wafer, in a reasonably short time.

The first crude attempt yielded a machine which was capable of good resolution of wafer transmittance. Some 400 points in an area 40x40 mm² were scanned in more than two hours. Further improvements have produced a system that scans about 2,000 points covering the entire wafer area in less than 20 minutes under control of an Apple II computer. The experimental data are then plotted in the fashion shown in figure 1-2. This apparatus and its theoretical foundations are described in detail in Chapter 2 of this dissertation.

For some time this was the only apparatus anywhere capable of such performances. Similar set-ups have been made, with our advice, at Varian Associates and Spectrum Technology.

Practically all the wafers analyzed in the course of this work are made of SI GaAs grown by the liquid

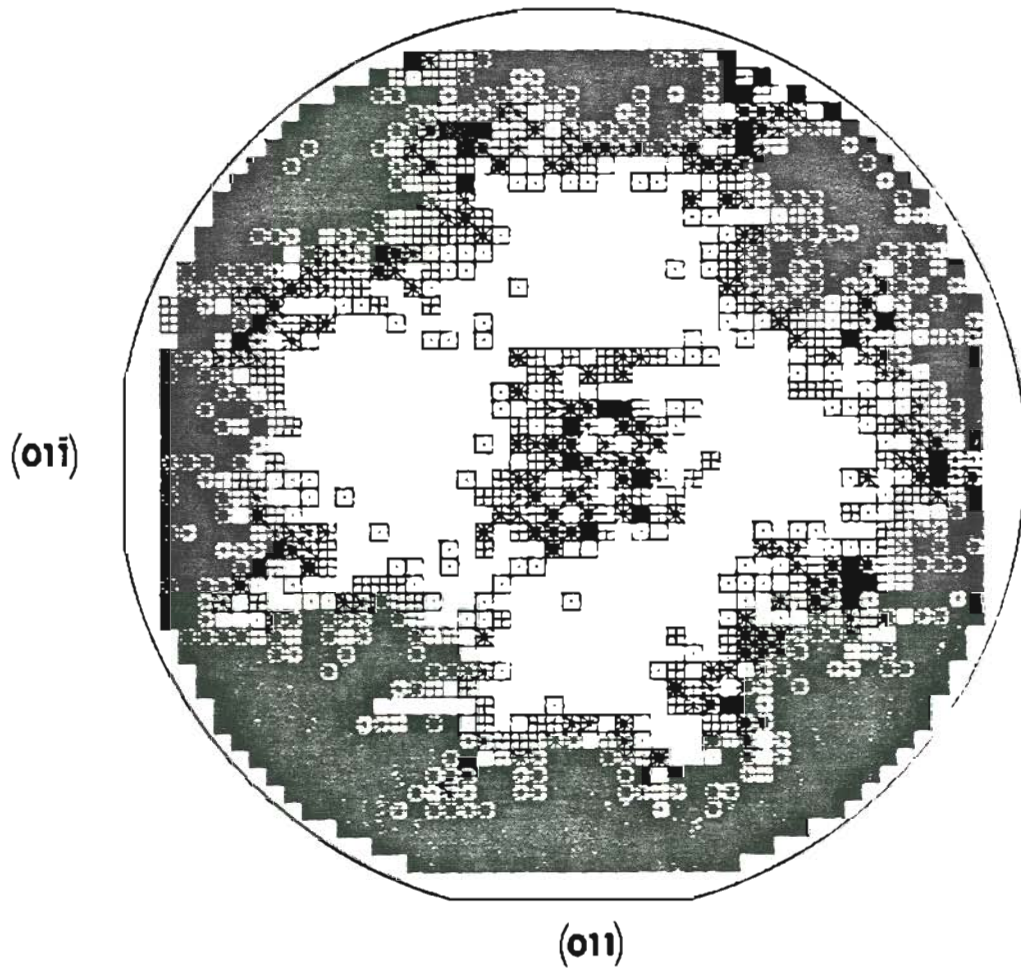


Figure 1-2: EL2 map obtained from infrared absorption measurements. The local EL2 concentration is proportional to the shading level of each pixel. The flats identify two (110) planes.

encapsulated Czochralski (LEC) method [17]. With the LEC process, a GaAs crystal is slowly pulled from the melt while crystal and crucible rotate, usually in opposite directions. The major advantage of a LEC system is the ability to grow crystals in the [100] direction with high yield. (Only wafers cut parallel to the non-polar (100) plane are used by the IC industry).

The LEC technique produces heavily dislocated material, with the characteristic dislocation pattern that can be seen in Fig. 1-3. The dislocations are more numerous in the [100] class of directions than in the [110] directions, with local minima at about midpoint from the center. This distribution was explained by Jordan et al. [18] in terms of stress generated by the nonuniform temperature distribution during the post-growth cooling phase.

Since the EL2 pattern is often found to be spatially connected to the distribution of dislocations, it was deemed necessary to have a capability to reveal, and possibly map, the dislocation pattern in our samples. Dislocations are usually revealed by etching the sample in a bath of molten potassium hydroxide (KOH) [19]; a dislocation intersecting the wafer surface is seen as a concave pyramidal pit. The

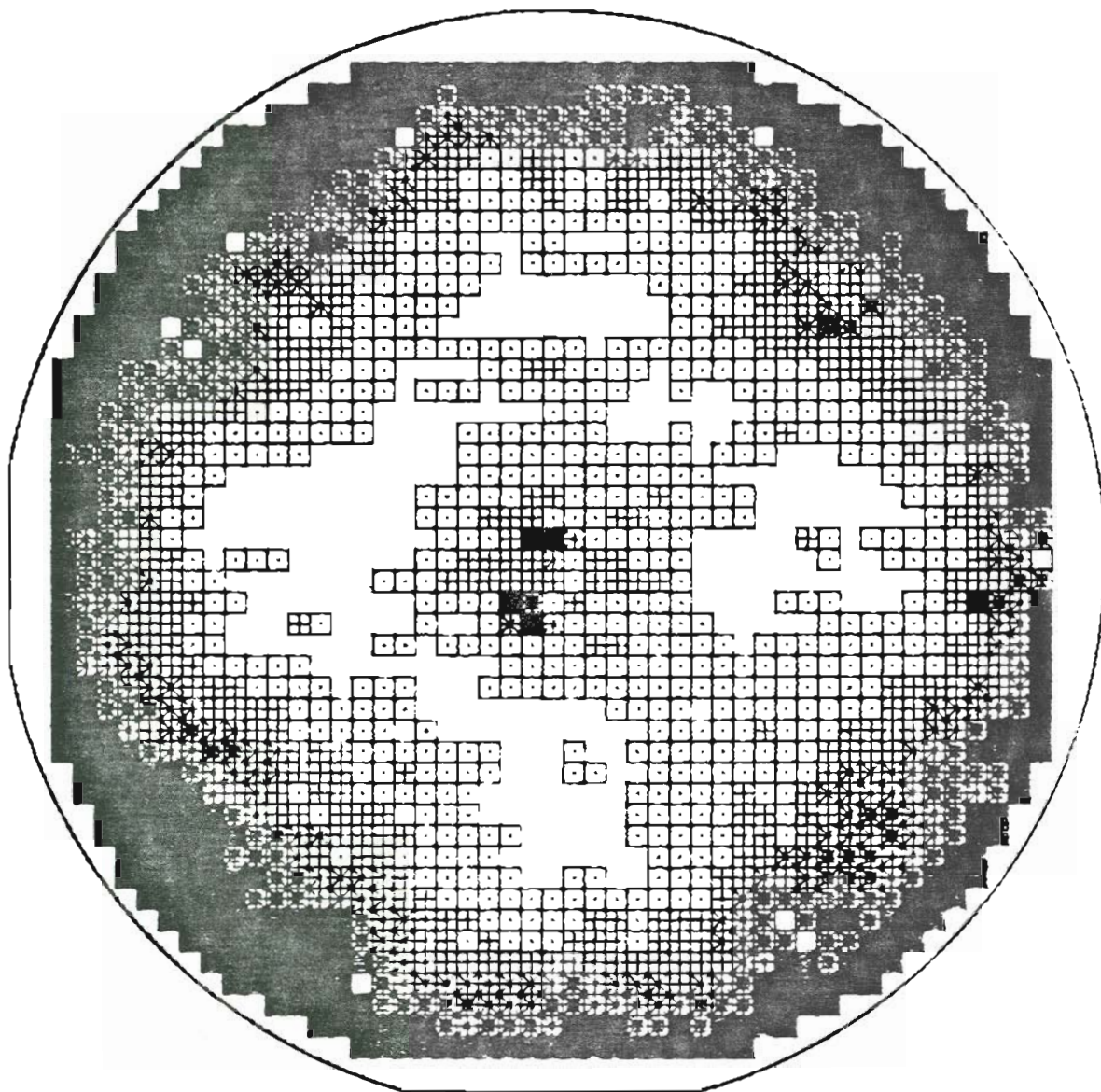


Figure 1-3: Dislocation density map obtained from infrared transmittance measurements. The dislocation density is lower in the white lobes along the $[110]$ directions.

dislocation density is then calculated counting the number of pits seen in a micrograph of the surface at convenient magnification [20].

This standard technique has been improved in the counting process as well as in the actual etching phase. The count of pits has been made simpler and more accurate on the basis of the observation that the correct exposure of a micrograph varies linearly with the density of pits. It was later found that vapor from the KOH melt is energetic enough to slowly etch an exposed GaAs surface, so that the destructive dip into the melt can be avoided.

The use of molten KOH is in any case far from being convenient. Thus the A/B etch [21], a mixture of water, hydrofluoric acid, silver nitrate and chromium trioxide can replace KOH as selective etchant. The A/B etch can be used at room temperature, and although these two etchants act in different fashion, as will be discussed in Chapter 2, for mapping purposes they give the same results. Once etched, the wafer is optically mapped (at $1.45 \mu\text{m}$, typically, far beyond the EL2-related absorption band) providing a qualitative map of the dislocations.

Dislocations arise as a result of mechanical stress in

the material, and in the presence of stress even normally optically isotropic crystals acquire to some extent the optical properties of anisotropic crystals. This is the case for gallium arsenide [22], as well as for silicon [23]. As a result, stressed wafers of GaAs grown by the LEC method show photoelastic patterns when scanned with radiation for which the material is transparent. The set-up normally used for EL2 mapping can detect weak stress related interference figures, of the kind displayed in Fig. 1-4 when the wafer is mapped at a suitable wavelength, yielding the first direct confirmation of the thermoelastic stress models by Jordan et al. [18] and by other researchers [24,25].

Like all the techniques used or developed in the course of this work, these procedures are described in Chapter 2, while results concerning the stress and EL2 distributions are shown and discussed in Chapter 3.

The frequent coincidence of EL2 and dislocation patterns has produced a number of proposals [5,10,15,26,27] which causally link EL2 to the presence of dislocations by means of a stress enhanced EL2 formation or production of EL2 by dislocation climb.

From the data collected here, a conclusion has been

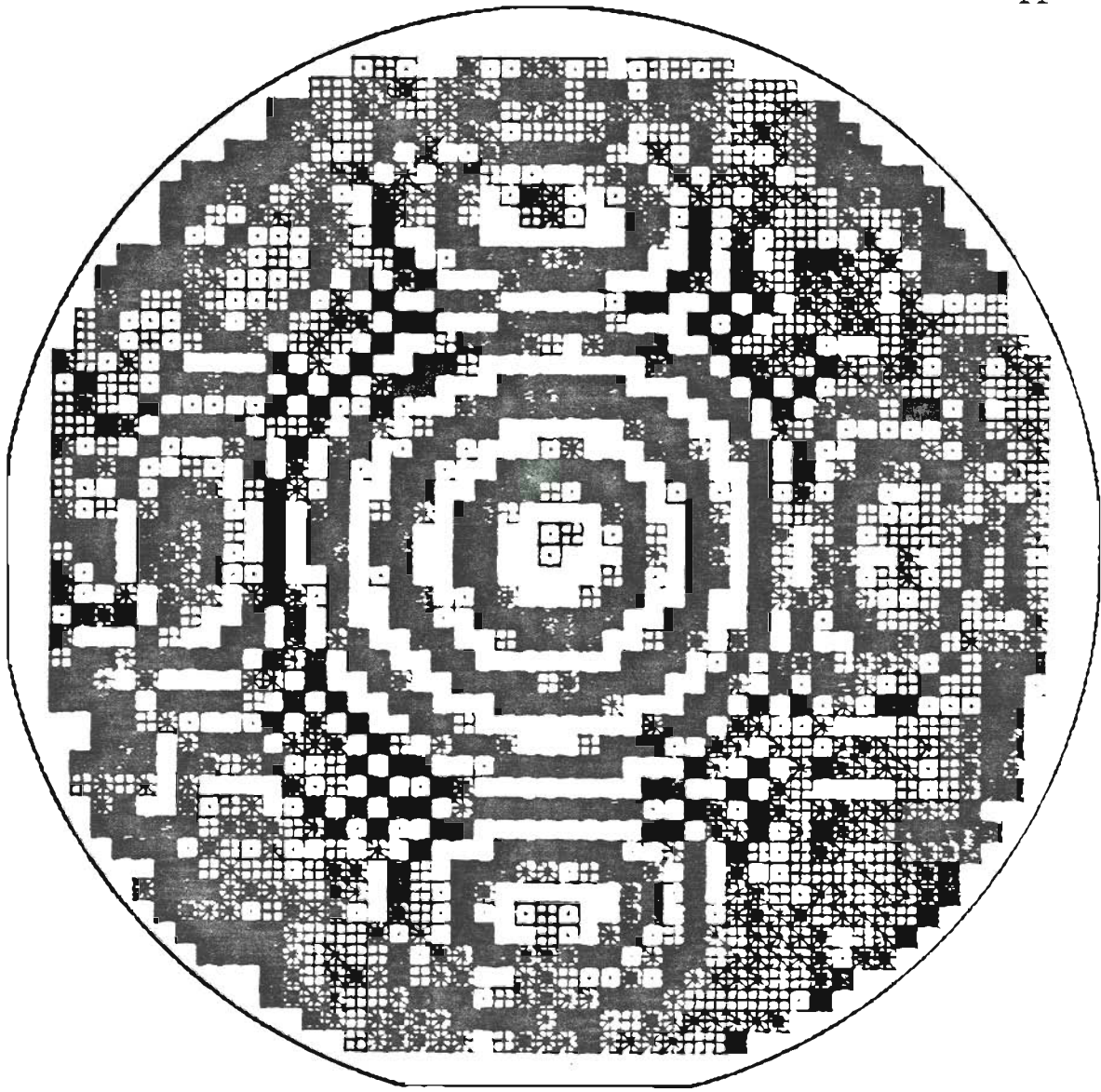


Figure 1-4: Interferometric contours of constant stress, with four-fold symmetry.

reached that dislocations play a secondary role in local variations of NEL2 only through a gettering effect. In fact, apart from a statistical coincidence between NEL2 and dislocation density, no quantitative relationship exists between NEL2 and dislocations within a wafer as well as from wafer to wafer.

The generally accepted procedure of testing wafers from only seed and tail portions of each ingot (on the assumption that such wafers are representative of the whole crystal) produces results that do not show any general trend. On the contrary when a series of wafers cut from equally spaced positions along an ingot has been mapped, NEL2 may be found to be quite constant for most of the length of the crystal, while only the top and bottom wafers show significant variations. Such results are discussed in Chapter 3.

The ability to map EL2 in thin wafers has provided a possibility of correlating these maps with similar ones of the performances of devices made in SI GaAs substrates, as shown in Chapter 4. Due to the lack of sensitivity of EL2 systems elsewhere, such correlation had never been made before. Studies that were targeted to the effect of dislocations on FETs lacked any knowledge of the actual

EL2 distribution. While a group of researchers [28-30] consistently claimed a strong correlation between FET properties and vicinity to a dislocation, others [31] ruled out that such correlation exists.

In fact when EL2 and dislocation patterns coincide - and in some cases they do - it cannot unambiguously be proven that either parameter is the cause of changes of performances of devices. Among the samples analyzed, some were found in which EL2 and dislocation distributions are decoupled, and EL2 then appeared to control parameters such as the FET threshold voltage (V_{th}) and saturation current (I_{dss}). The same researchers that claimed a cause-effect relationship between dislocations and FET parameters [28-30], found such correlation less demonstrable when the wafers were annealed at high temperature. Since it is known that EL2, contrary to dislocations, redistributes upon annealing, this appears to confirm the arguments advanced in this dissertation.

REFERENCES

1. T. R. Jervis, D. W. Woodward, and L. F. Eastman, *Electron. Lett.* 20, 620 (1979)
2. T. Ikoma, M. Takikawa, and M. Taniguchi, *Inst. Phys. Conf. Ser.* 63, 191 (1982)
3. S. Makram-Ebeid, P. Langlade, and G. M. Martin, in *Semi-Insulating III-V Materials: Kah-nee-ta 1984*, edited by D. C. Look and J. S. Blakemore, (Shiva, Nantwich, UK, 1984), p. 184
4. D. E. Holmes, R. T. Chen, K. R. Elliott, C. G. Kirkpatrick, and P. W. Yu, *IEEE Trans. El. Dev.* 29, 1045 (1982)
5. D. E. Holmes, R. T. Chen, K. R. Elliott, and C. G. Kirkpatrick, *Appl. Phys. Lett.* 40, 46 (1982)
6. M. D. Miller, G. H. Olsen, and M. Ettenberg, *Appl. Phys. Lett.* 31, 538 (1977)
7. E. E. Wagner, D. E. Mars, G. Hom, and G. B. Stringfellow, *J. Appl. Phys.* 51, 5434 (1980)
8. L. Samuelson, P. Omling, H. Titze, and H. G. Grimmeiss, *J. Cryst. Growth* 55, 164 (1981)

9. M. O. Watanabe, A. Tanaka, T. Nakanisi, and Y. Zohta, Jap. J. Appl. Phys. 20, L429 (1981)
10. K. R. Elliott, R. T. Chen, S. G. Greenbaum, and R. J. Wagner, in Semi-Insulating III-V Materials:Kah-nee-ta 1984, edited by D. C. Look and J. S. Blakemore (Shiva, Nantwich, UK, 1984), p.239
11. U.Kaufmann, J. Windscheif, M. Baeumler, J. Schneider, and F. Kohl, in Semi-Insulating III-V Materials:Kah-nee-ta 1984, edited by D. C. Look and J. S. Blakemore (Shiva, Nantwich, UK, 1984), p.246
12. B. K. Meyer, J. M. Spaeth, and M. Scheffler, Phys. Rev. Lett. 52, 851 (1984)
13. G. M. Martin, Appl. Phys. Lett. 39, 747 (1981)
14. M. Kaminska, M. Skowronski, J. Lagowski, J. M. Parsey, and H. C. Gatos, Appl. Phys. Lett. 43, 802 (1983)
15. D. E. Holmes, R. T. Chen, K. R. Elliott, and C. G. Kirkpatrick, Appl. Phys. Lett. 43, 305 (1983)
16. M. S. Skolnick, M. R. Brozel, L. J. Reed, I. Grant, D. J. Stirland, and R. M. Ware, J. El. Mat. 13, 107 (1984)
17. R. K. Willardson, in Semi-Insulating III-V Materials:Kah-nee-ta 1984, edited by D. C. Look and J. S. Blakemore (Shiva, Nantwich, UK, 1984), p.96

18. A. S. Jordan, R. Caruso, and A. R. Von Neida, Bell Syst. Tech. J. 59, 593 (1980)
19. J. G. Grabmaier and C. B. Watson, Phys. Stat. Solidi, 32, K13 (1969)
20. Annual Book of Standards, Part 43 (Electronics), Standard Test Method F47-70 (ASTM, Philadelphia, 1981) p. 285
21. M. S. Abrahams and C. J. Buicocchi, J. Appl. Phys. 36, 2285 (1965)
22. C. W. Higginbotham, M. Cardona, and F. H. Pollak, Phys. Rev. 184, 821 (1969)
23. S. R. Lederhandler, J. Appl. Phys. 30, 1631 (1959)
24. N. Kobayashi and T. Iwaki, J. Cryst. Growth 73, 96 (1985)
25. G. Szabo, J. Cryst. Growth 73, 131 (1985)
26. D. E. Holmes and R. T. Chen, J Appl. Phys. 55, 3588 (1984)
27. M. R. Brozel, I. Grant, R. M. Ware, D. J. Stirland, and M. S. Skolnick, J. Appl. Phys. 56, 1109 (1984)
28. Y. Ishii, S. Miyazawa, and S. Ishida, IEEE Trans. El. Dev. ED-31, 800 (1984)
29. S. Miyazawa, Y. Ishii, S. Ishida, and Y. Nanishi, Appl.

- Phys. Lett. 43, 853 (1983)
30. Y. Nanishi, S. Miyazawa, and Y. Matsuoka, in Defect Recognition and Image Processing in III-V Compounds: Montpellier, 1985, edited by J. P. Fillard (Elsevier, Amsterdam, NL, 1985), p. 225
31. H. W. Winston, A. T. Hunter, H. M. Olsen, R. P. Bryan, and R. E. Lee, Appl. Phys. Lett. 45, 447 (1984)

CHAPTER 2

EXPERIMENTAL TECHNIQUES

A. Introduction

This chapter describes the experimental techniques, and their theoretical foundations, developed in the course of this study.

The experimental work can be roughly divided in two parts, the first grouping together two non-destructive measurements, i.e. EL2 and stress mapping, while the second one describes the observation of dislocations in chemically etched GaAs wafers.

The non-destructive measurements are based on the apparatus for mapping the local near-infrared (near-IR) transmittance of thin GaAs wafers that was built in the course of this research. This system has been utilized for EL2 mapping, converting the sample transmittance at about $1\mu\text{m}$ into the equivalent absorption coefficient, and for

residual stress mapping, from transmittance data at $1.37 \mu\text{m}$. Sections B and C of this chapter describe these topics.

The second part (sections C, D, and E) consists of a novel development of the standard etching technique in molten KOH, a simple quantitative measurement of the dislocation density, and the use of the IR transmittance set-up for qualitative mapping of the dislocation distribution.

B. EL2 mapping

Near-infrared absorption measurements at room temperature are feasible for the concentration determination of deep flaw species in SI GaAs. The material does not have to be SI, but it is necessary that the Fermi energy be far enough from either band to ensure negligible competition from free carrier absorption [1]. That can be assured if the Fermi level position (E_f) is controlled by the EL2 midgap donor defect in a nominally undoped crystal.

The numerical information obtainable from transmittance mapping of an entire wafer should be distinguished from the qualitative information derivable from transmittance microscopy in the near IR. In this case images can be captured either on IR-sensitive film, or with a silicon vidicon as the receptor array [2-4], or with a silicon Reticon device[5]. These detectors have a field of view from a few mm² to a few cm², depending on the magnification used.

Despite the usefulness [2-6] and visual appeal of a transmission micrograph it serves a different purpose from a quantitative whole-wafer map, and does not replace the

latter. It is improbable in fact that all receptor elements in a vidicon or other multi-element detector can be matched closely enough, in linearity and responsivity, for a quantitative measurement of the absorption coefficient α to be made through the field of view- especially under the stringent circumstances of $\alpha t \ll 1$. Only a selected single-element detector can resolve 0.05% changes of transmittance in wafers as thin as 0.035 cm.

It is assumed in what follows that a sample to be mapped is of uniform thickness t , with faces that are plane, parallel, and both polished. This is illuminated from one side, with a flux of near-IR photons focussed on a small area. The incident flux is almost paraxial, using a focussing lens of large f -number, so that the reflection coefficient of concern is that for normal incidence.

Since the EL2 absorption is extrinsic and weak, we can safely ignore any influence of the extinction coefficient k on the reflectance; since $k = (\alpha\lambda/4\pi)$, the requirement that $k \ll 1$ is equivalent to $\alpha \ll 10^5 \text{ cm}^{-1}$ in the near IR range, more than amply satisfied in our case.

Then the reflectance for normal incidence reduces to

$$R = [(n - 1)/(n + 1)]^2 \quad (1)$$

at both the front (air:semiconductor) and rear (semiconductor:air) faces of the sample, determined exclusively by the real part n of the refractive index. This normal reflectance is quite large for GaAs, because of the high refractive index.

Figure 2-1 shows n as a function of $h\nu$ for three temperatures, in the immediate sub-bandgap spectral range of GaAs. The figure reproduces data points and curves from the prism refraction work of Marple [7]. These 300 K values were shown by Stillman *et al.* [8] to be in good agreement with those of two subsequent room temperature studies.

J.S. Blakemore has pointed out, in a review of GaAs properties [1], that the 300 K refractive index data are a good fit to

$$n_{300}(h\nu) = \{7.10 + 3.78[1 - 0.18(h\nu)^2]^{-1}\}^{\frac{1}{2}} \quad (2)$$

The curve in Fig. 2-2 rising from left to right shows the variation with $h\nu$ of the room temperature normal reflectance for GaAs, as provided by Eq. (1) when n_{300} is

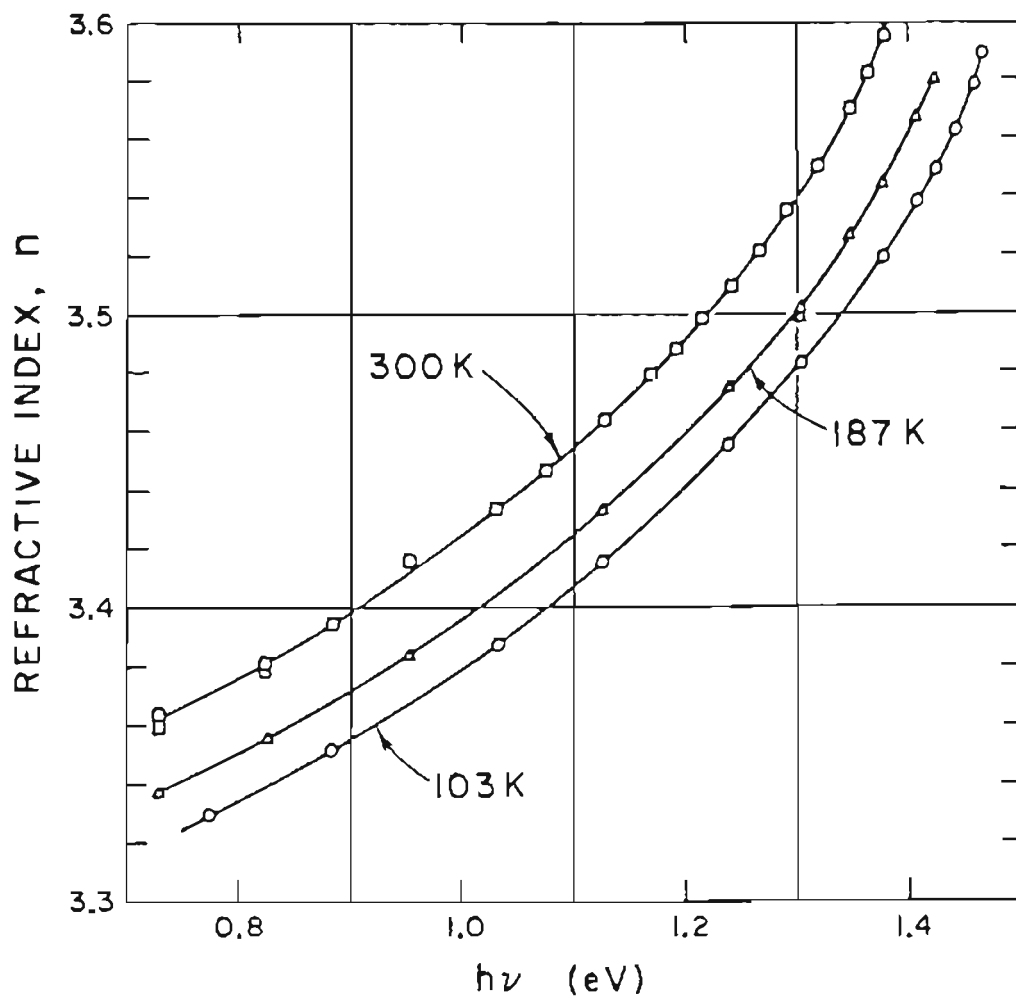


Figure 2-1: GaAs refractive index versus photon energy at different temperatures, after Marple [7].

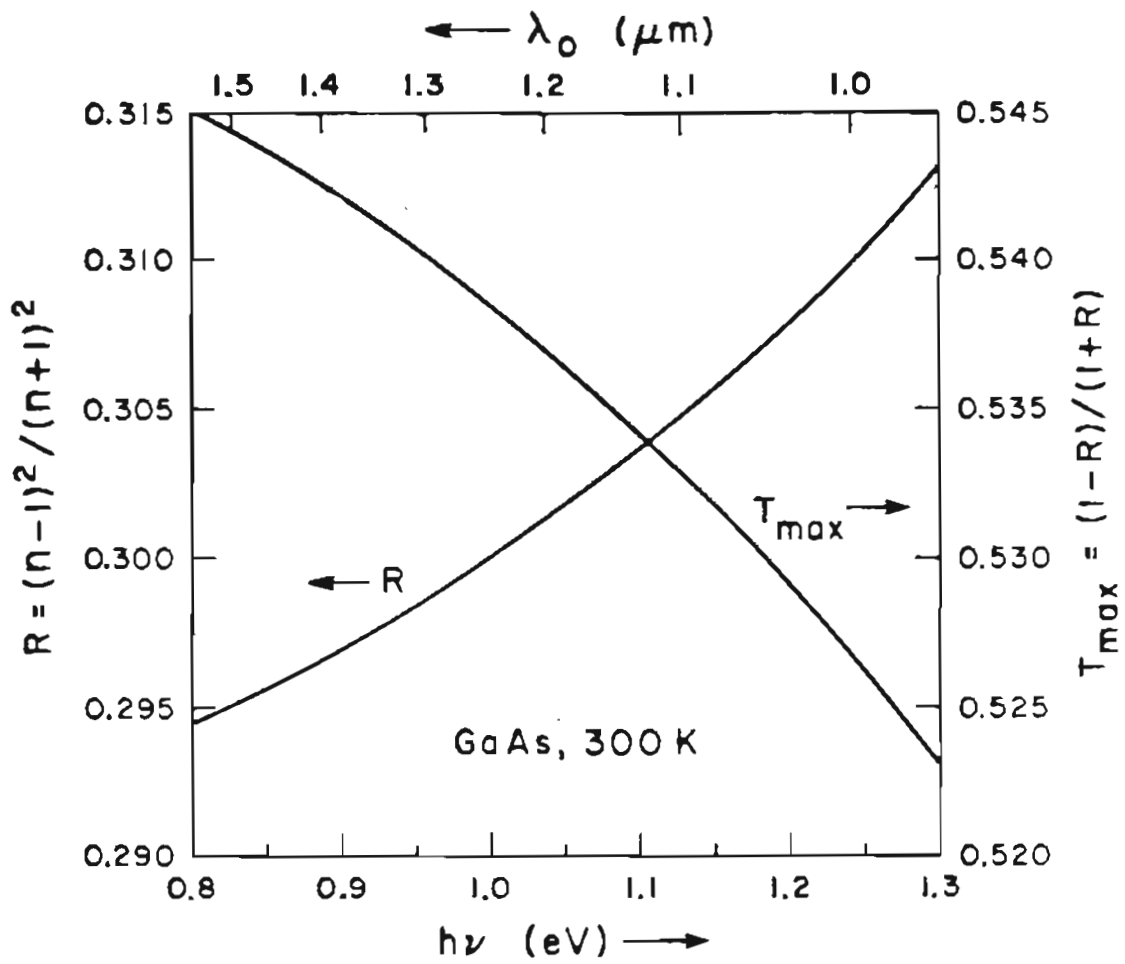


Figure 2-2: GaAs spectral reflectivity and maximum transmittance.

modeled by Eq. (2). The abscissa here covers the spectral range $0.8 < h\nu < 1.3$ eV of the greatest concern for optical transmittance mapping of midgap flaws in general and of EL2 in particular.

One wishes for the illuminating photons to be approximately monochromatic, so that a specific value of the spectrally dependent α is appropriate. At the same time, it is desirable that the spectral width be sufficient so that the optical coherence length is small compared with the sample thickness. The spectral width below which interference effects can be detected is given by the relation

$$\Delta\lambda = \lambda^2 / (2nt) \quad (3)$$

which identifies the period of the fringes ($\Delta\lambda$) in terms of wavelength. For a 0.5 mm thick GaAs wafer explored by radiation at $\lambda = 1.0 \mu\text{m}$, Eq. (3) gives $\Delta\lambda = 0.3$ nm, which is well below the spectral width of our experimental system.

When a paraxial incident photon flux I_0 satisfies these conditions, the flux I_t emerging from the back side is not affected by coherent interference considerations. Multiple

internal reflections will still contribute towards I_t , but their effects are determined by addition of intensities, rather than of complex amplitudes. This results in a fractional transmittance

$$T = (1 - R)^2 \exp(-\alpha t) [1 - R^2 \exp(-2\alpha t)]^{-1} \quad (4)$$

which is a quadratic equation for $\exp(\alpha t)$, with the positive root

$$\exp(\alpha t) = [(1 - R)^2 / 2T] \{ 1 + [1 + 4R^2 T^2 (1 - R)^{-4}]^{1/2} \} \quad (5)$$

The minicomputer of the measurement system stores Eqs. (1), (2), and (5), so that for a sample of known t and selected $h\nu$, a measured value of T can immediately be expressed as the equivalent value of α .

That intermediate result is then converted into $N\epsilon L_2$ by means of assumptions about the EL2 optical cross-sections, as discussed below.

The transmitted flux is severely attenuated if absorption is powerful enough to make $\alpha t \gg 1$, but measurement difficulties for that situation are quite

different from those of present concern. As indicated in Table 1, measurements for GaAs at a wavelength $\lambda = 1.10 \mu\text{m}$ and an optical thickness $\alpha t = 0.25$ yield $T = 0.40$, and for that comfortable situation the transmitted energy falls by 1% for an increase of 4% in αt . This will be the case for an undoped SI GaAs slab some 3 mm thick with $N_{EL2} = 10^{16} \text{ cm}^{-3}$, and that is why polished GaAs slabs with thicknesses in the range 3-5 mm have been used for the great majority of transmittance studies reported for EL2 in this material [2-6,9,10].

Suppose, however, that the sample thickness is considerably smaller, and/or that N_{EL2} is well below the 10^{16} cm^{-3} range. Either or both of these will move the measurement situation towards the "optically thin" limiting conditions of $\alpha t \ll 1$. All values of T then lie within a narrow range, with an upper limiting value

$$T_{\text{max}} = (1 - R)/(1 + R) \quad (6)$$

for a sample which has the unavoidable reflection losses, but zero absorption.

The variation of T_{max} with $h\nu$ for GaAs at 300 K is

shown in Fig. 2-2, as the curve which falls as $h\nu$ rises. This curve is drawn on the same premise as the curve for R in that figure, assuming n of Eq. (2) in then evaluating R of Eq. (1), and hence T_{\max} of Eq. (6).

It will be seen from Fig. 2-2 that reflection losses amount to about 50% for a polished GaAs sample, at any near-IR wavelength. Table 1 quotes actual numbers for two wavelengths (1.00 and 1.10 μm) that have been used in many EL2 transmittance studies.

TABLE I

Wavelength (μm)	1.1000	1.0000
Photon energy (eV)	1.1271	1.2398
Refractive index n [Eq.(2)]	3.4642	3.5108
Normal reflectance R [Eq.(1)]	0.3047	0.3098
T, for $at = 0$ [Eq.(6)]	0.5329	0.5269
T, for $at = 0.05$ [Eq.(4)]	0.5021	0.4962
T, for $at = 0.25$ [Eq.(4)]	0.3990	0.3939

One can observe that $(T_{\max} - T) = 0.0063$ when $at =$

0.01, which means that detection of a 10% change in optical density under those conditions entails detection of a $\Delta T = 0.0006$.

As for the optical absorption related to EL2, consider "undoped" GaAs containing such defect, of concentration N^0 in the neutral ground state, and N^+ ionized by the presence of some kind of acceptor level in the lower half of the gap. Hence $N^0 + N^+ = N_{EL2}$.

Then the total absorption coefficient, for a near-IR extrinsic $h\nu$, can be written as

$$\alpha = \sigma_n N^0 + \sigma_p N^+ + \alpha_0 \quad (7)$$

The scaling parameter for the first term on the right side of Eq. (7) is σ_n , the optical absorption cross-section for neutral EL2 sites. The spectral form of this as measured by photocapacitance was attributed by Chantre et al. [11] entirely to photoionization (to the various conduction bands), though Kaminska et al. [12] showed a decomposition of σ_n into a photoionization continuum plus a Gaussian intracenter transition band.

It appears necessary to write something about the two

remaining terms on the right of Eq. (7). The middle term is scaled by the photoneutralization cross-section σ_p , for the process whereby an ionized EL2 center annihilates a photon and creates a free hole; while the final term α_0 lumps together any absorption process unrelated to EL2. The term α_0 must be quite small for room temperature measurements in "undoped" LEC SI GaAs of good quality, at near-IR wavelengths. Free carrier absorption [1] can be ignored in view of the SI status, and for the wavelengths typically used for EL2 mapping $h\nu$ is large enough to also make any multiphonon lattice absorption negligible [1].

Should either of the wafer surfaces be inadequately polished, this will cause optical scattering, of which the consequence for the received signal can be regarded as contributions towards α_0 . (This is, in fact, the basis of the measurement of the dislocation distribution in etched wafers). However, we have measured mirror-polished SI wafers from commercial sources with transmittance behavior at different wavelengths suggesting that the quantity α_0 was negligibly small.

A similar assurance cannot be given that the term σ_p will be a very small contributor towards α for SI GaAs,

though numbers for σ_p are elusive. Chantre et al. [11] show the spectral form for σ_p as deduced from photocapacitance measurements (without absolute size information) having a threshold near 0.6 eV, peaking near 0.9 eV, and then a decline until about 1.25 eV. A further rise indicated for $h\nu > 1.25$ eV might have been affected by extraneous processes. However, more important here is how large σ_p is for $1.10 < h\nu < 1.25$ eV. That assessment was attempted by Martin [13], using photocurrent transient spectroscopy, and he concluded that σ_p might be as large as $0.3\sigma_n$ at 1.17 eV.

Our measurements of the spectral dependence of α for SI samples from various sources, and likely differing extents of EL2 compensations, leads to a conclusion that the scale of σ_p is likely to be substantially smaller than that of σ_n .

Knowledge of the true scale for σ_p thus still awaits a definitive study, whereas that for σ_n is reasonably firmly based. Martin [14] measured the transmittance spectra at 300 K, 85 K, and < 10 K, for undoped GaAs samples which by their negative Hall coefficient and intermediate resistivity evidenced that E_F was appreciably above midgap. Thus these samples should have had negligible free carrier absorption,

but all EL2 sites could be expected to be filled with electrons: $N^0 \gg N^+$, to make the right side of Eq. (7) dominated by the first term.

Figure 2-3 is based on Martin's first figure [14], in showing absorption coefficient data for 300 K and 85 K. Martin had provided with an arbitrary ordinate scale, but he had also shown calibration of α versus N^0 consistent with $\sigma_n(1.13 \text{ eV}) = 8.5 \times 10^{-17} \text{ cm}^2$ for $T = 300 \text{ K}$, and with $\sigma_n(1.24 \text{ eV}) = 1.2 \times 10^{-16} \text{ cm}^2$ both for 300 K and cryogenic temperatures. These enable us to provide the numerical ordinate scale shown in Fig. 2-3, with these two calibration points marked by the pairs of broken lines. Of the curves in Fig. 2-3, the 300 K one interests us most immediately for the simplicity of room temperature EL2 mapping, in that optical access over the entire area of a wafer cooled to liquid nitrogen temperature presents a few experimental complications.

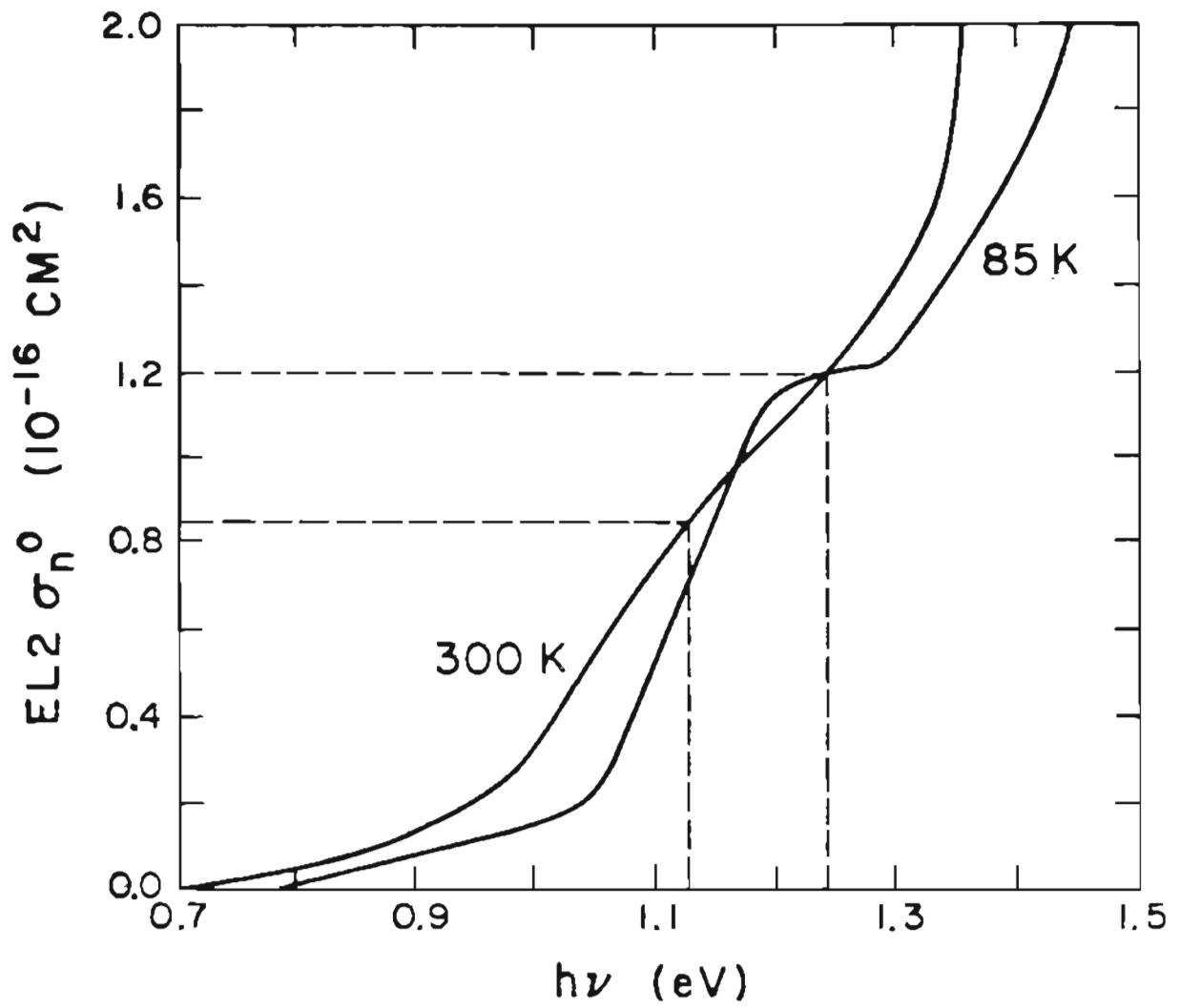


Figure 2-3: EL2 absorption cross-section versus photon energy, after Martin [14].

C. STRESS MAPPING

The thermal stress produced in a single crystal by the temperature gradient during post growth cooling deforms the crystal plastically and generates dislocations when the shear stress exceeds a critical value. The fraction of the stress relieved by dislocations at high temperature reappears, opposite in magnitude, when the temperature gradient fades at room temperature.

Brittle materials -such as GaAs- may even crack upon cooling after growth. Apart from these extremes there is a special need to produce dislocation-free GaAs of large diameter for optoelectronic devices, while the effect of dislocations on FETs built on SI GaAs substrates is subject of lively discussion and will be treated in detail in Chapter 4 of this dissertation.

Some detailed calculations [15-17] of the stress field in cylindrical crystals grown by the Czochralski method have been performed, but such efforts have not been matched by similarly sophisticated experimental techniques. The usual KOH etching process [18] and its improvements discussed at

and Si in their unstressed state.

2: Crystals with 2 crystallographically equivalent directions in one plane: these crystals, from trigonal, tetragonal, and hexagonal systems are called uniaxial. The plane containing the equivalent directions is perpendicular to the (optical) axis of 3,4, and 6 fold symmetry.

GaAs is described by the point group $\bar{4}3m$, which means that the crystal enjoys (reversed) tetragonal symmetry about [100] directions, trigonal about [111] ones and mirror symmetry about [110] directions. Accordingly the crystal is optically uniaxial only for stresses along either [100] or [111] directions .

3: Crystals without 2 crystallographically equivalent directions: defined as biaxial materials, this is the case of GaAs subject to stress along arbitrary directions [24].

The optical properties of the three types of crystals are described by the index ellipsoid. That for a crystal belonging to the first class is just a sphere. The ellipsoid has two axes equal and one unequal in the case of uniaxial

crystals, and the three axes have unequal lengths in crystals belonging to the third class. The terms uniaxial and biaxial refer to the number of optic axes, that is the number of diameters with the property that a plane section at right angle to them through the center of the ellipsoid is a circle. The character of the solid describing the index of refraction of a material can be probed by observing the sample under illumination with convergent polarized light.

Supposing these experimental conditions are satisfied, what is the appearance of a biaxial crystal?

An anisotropic crystal will divide an entering beam of monochromatic light into two beams having orthogonal polarizations. With the exception of two specific directions, identified by the optic axes, the beams will propagate along different paths with different speeds. While one of the two beams is called ordinary (since it behaves as any ordinary light beam), the other is called extraordinary, in that it does not follow Snell's rule.

When viewing a biaxial crystal between crossed polarizers with converging light entering the sample from any direction not coincident with either optic axis it can be shown with lengthy calculations [23] that points of

minimum transmittance form a cross, when the polarizer axis lies in the plane containing the optical axes, and two hyperbolae with asymptotes in the directions of the polarizer/analyzer axes when the polarizer axis is at 45° from such plane. Images of this kind are shown in figure 2-4, where the polarizer axis is parallel to the $[011]$ direction in part (a), and at 45° from the $[011]$ direction in part (b). From this figure, we are immediately able to recognize that the optic axes lie in the $(01\bar{1})$ plane. Such images can be understood with the aid of Fig. 2-5, where the directions of polarization are identified. The shaded areas represent parts of the sample where the polarization of either ray is orthogonal to one of the polarizers. An uniaxial crystal would show a cross in both cases, although its arms would always be parallel to the polarizer/analyzer pair axes [25].

Because of the crystalline nature of the material and the use of plane-polarized light, this measurement probes the geometry of the index ellipsoid. The topology of the ellipsoid, determined by the point group describing the material, does not change with the stress intensity or direction, as long as it is not parallel to $[100]$ or $[111]$

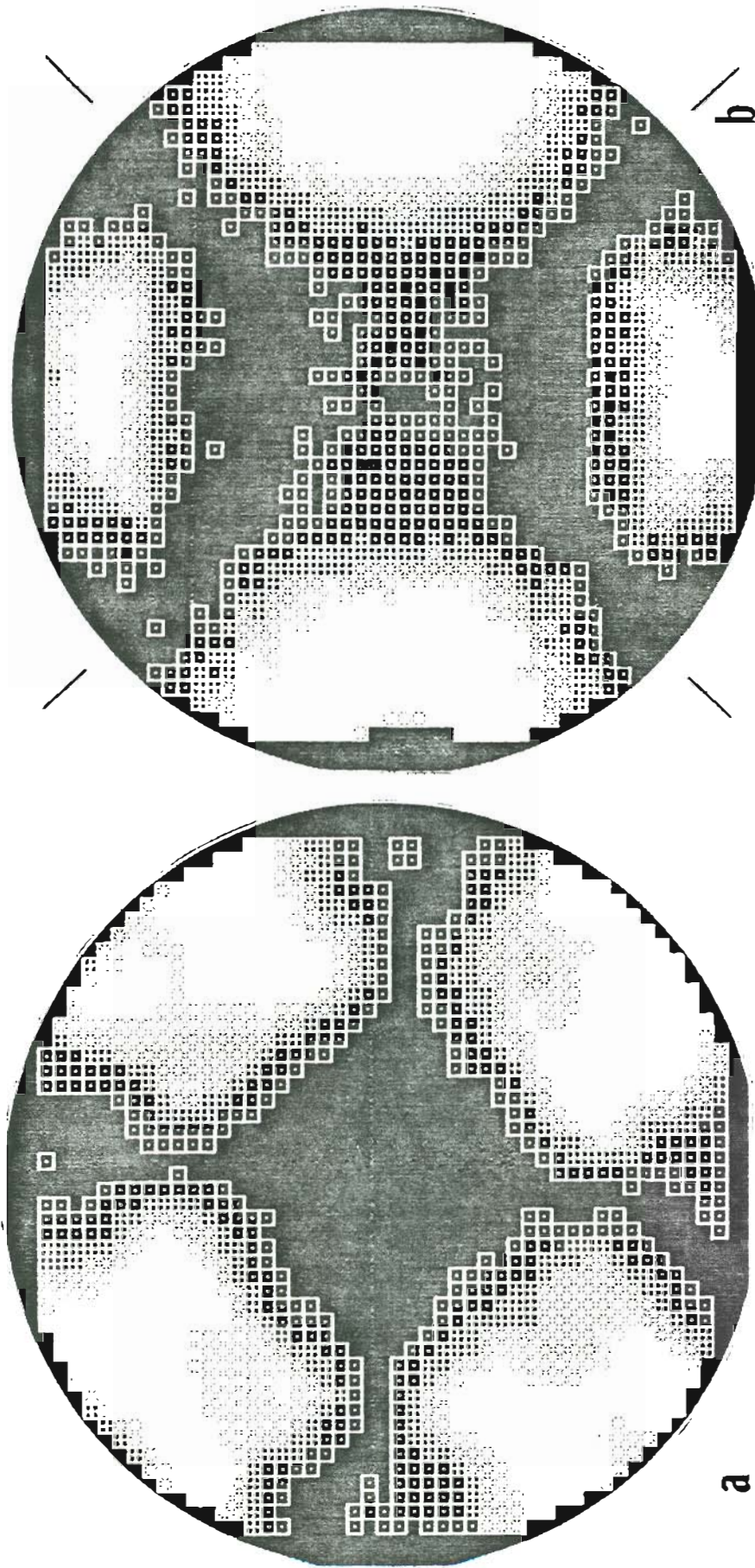


Figure 2-4: Transmittance map of a LEC grown GaAs wafer between crossed polarizers, illuminated by radiation at $\lambda = 1.4 \mu\text{m}$. (a) Polarizer axis parallel to [011]. (b) Polarizer axis parallel to [001], 45° from the previous position.

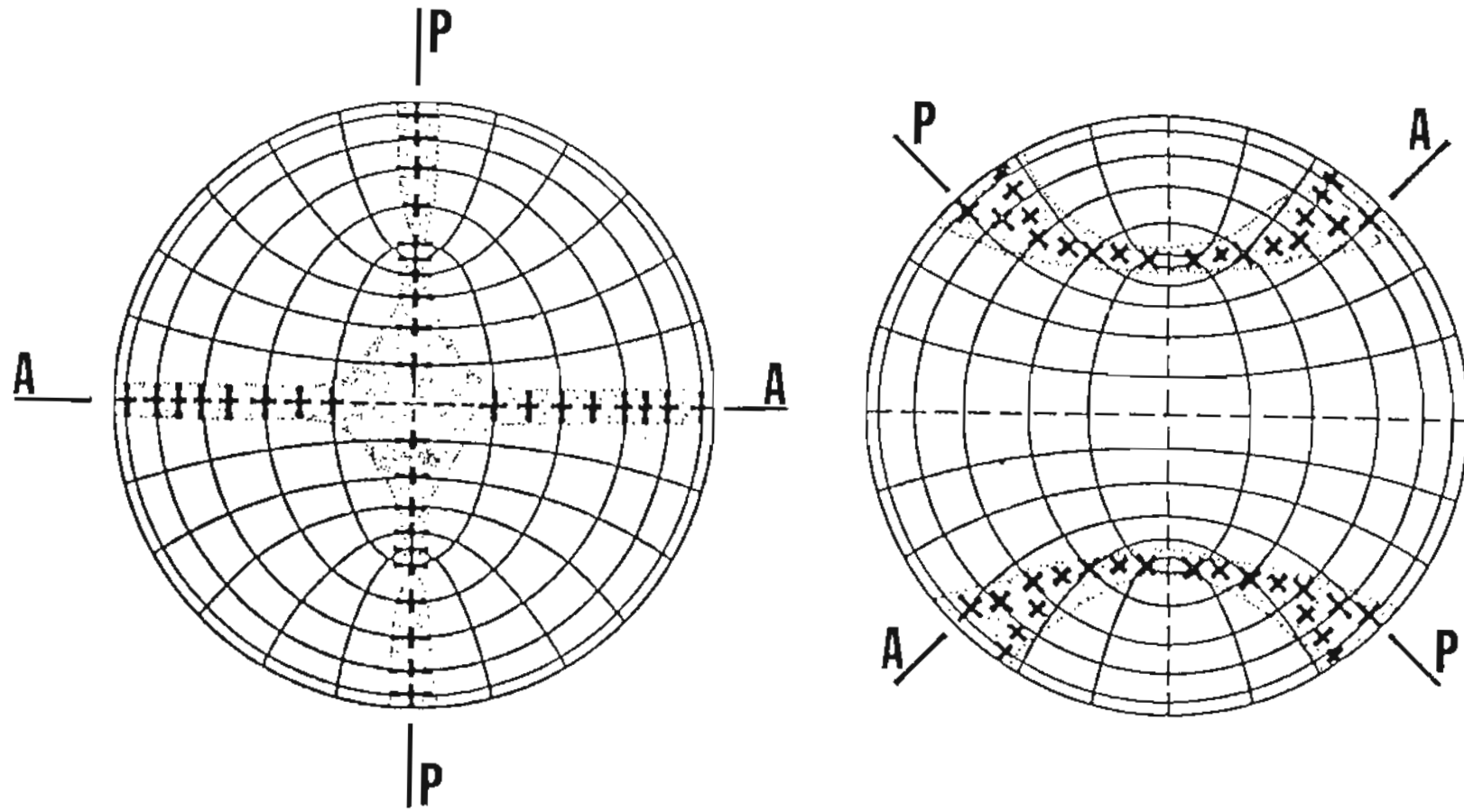


Figure 2.5: Polarization vectors of ordinary and extraordinary rays in a biaxial crystal, from Ref. 25 . The shaded trajectories correspond to the points of minimum transmittance in the experimental maps of Fig. 2-4.

classes of directions. Then a measure of the optical characteristic of a normally isotropic crystal is quite sensitive to the presence of stress, but does not provide information about the local stress configuration. The geometric features of the index ellipsoid are the controlling factor, and this is constant through the sample, being determined by the intrinsic properties of the material. As a result, the symmetry of the pattern obtained experimentally relates to the symmetry of the material, and not to the symmetry of the stress field.

A more important experiment can be done exploring the sample with a paraxial unpolarized beam of monochromatic light. While in the previous case the results are determined by the combination of the (externally imposed) initial state of polarization, by the interaction of the beam with the material and by the final state of polarization (again partially controlled by the analyzer), now the polarization of the beam is controlled only by the stressed material, no external constraints being applied. As a result a map of the local state of stress can be obtained.

Consider a paraxial beam of monochromatic light impinging normally to the surface of a wafer of GaAs of

thickness t . Given the orientation of LEC grown wafers, the beam propagation is then parallel to the [100] growth axis that, as will be shown in Chapter 3, is one of the principal stress axes.

Let the wavelength λ of the radiation be such that no absorption occurs in the sample.

Traveling in the sample, the originally unpolarized beam will be split in two sub-beams, each polarized along the direction of one of the two principal stresses in the plane perpendicular to the propagation direction. The index of refraction of the material is stress-dependent so that the two beams, traveling at different speeds will accumulate a relative retardation which can be described as [21,23]

$$\Delta = 2\pi t(n_1 - n_2)/\lambda \quad (8)$$

in terms of the two in-plane indexes of refraction or

$$\Delta = 2\pi t C_o(\sigma_1 - \sigma_2)/\lambda \quad (9)$$

in terms of the principal stresses.

The relative retardation Δ is the magnitude of the

relative angular phase shift developed between components of a light beam propagating in the direction of the third principal stress. The term C_o is known as the stress-optic coefficient, $C_o = (n_1 - n_2)/(\sigma_1 - \sigma_2)$ [21].

The relative retardation Δ is then proportional to the difference between the two principal stresses perpendicular to the path of propagation of the light beam, this difference being twice the maximum sustainable shear stress τ in the sample [21,23].

The third principal stress, having a direction parallel to the path of propagation of the light beam, has no effect on the relative retardation.

The stresses in a cylindrical boule of GaAs will be shown in Chapter 3 to be principal in a cylindrical coordinate system. As shown in Fig. 2-6, then, within the finite extension of the exploring beam, the polarization vector determined by (say) σ_1 in a portion of the beam does have a component ($\sigma_{1(2)}$) along the polarization vector parallel to σ_2 in a different part of the beam. Accordingly interference can be produced between these two components. In presence of interference, the intensity of the light reaching the detector is in general expressed as

$$I = I_1 + I_2 \cos(\Delta) \quad (10)$$

so that $I = I_{\min}$ for $\cos(\Delta) = -1$, or

$$2\pi t C_0 (\sigma_1 - \sigma_2) / \lambda = (2m + 1) \quad , \quad m = 0, 1, 2 \dots (11)$$

Inverting Eq. (11), destructive interference will take place at points of the sample where the difference between principal stresses, or shear stress, progressively satisfies

$$\frac{1}{2}(\sigma_1 - \sigma_2) \equiv \tau = \lambda(2m + 1) / (4tC_0) \quad (12)$$

for a wafer of thickness t , explored at a wavelength λ . The coefficient $C_0 = 1.5 \times 10^{-10} \text{ cm}^2 \text{ dyne}^{-1}$ is the appropriate stress-optic coefficient, as measured by Higginbotham et al. in 1965 [24].

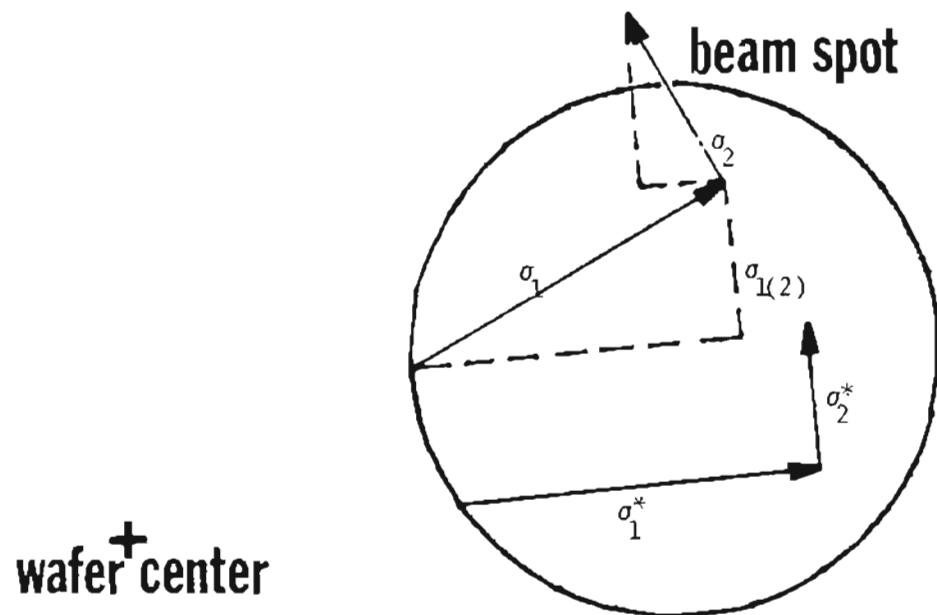


Figure 2-6: The component $\sigma_{1(2)}$ of the polarization vector σ_1 is parallel to σ_2^* , and the two beams can interfere. Similar interference takes place between $\sigma_{2(1)}$ and σ_1^* .

D. Infrared transmittance mapping system

The measurement system, whose physical configuration can be seen in figure 2-7, is basically very simple: a source of moderately monochromatic photons, a means to focus these as a paraxial cone onto a small area of the sample, collection and detection of the fraction transmitted, and a method to translate the sample with respect to the optical path.

The light source is a 40 W tungsten filament lamp (quartz-iodine bulb), energized by a DC power supply with remote sensing of the load voltage. The more conventional constant current operation had at first been tried, but proved inferior due to the lack of thermal stability of the sensing resistor. On the contrary, this constant voltage operation provides a photon flux constant within 0.05% after 1 hour of warmup time.

The lamp output is rendered "near-monochromatic" using a grating monochromator, with a 675 line/mm grating blazed for $1.00\ \mu\text{m}$, and for which the instrument has a direct calibration over the $0.7 - 1.50\ \mu\text{m}$ range. With 1 mm slit opening, a fractional spectral width $(\Delta\lambda/\lambda) = 0.012$ is

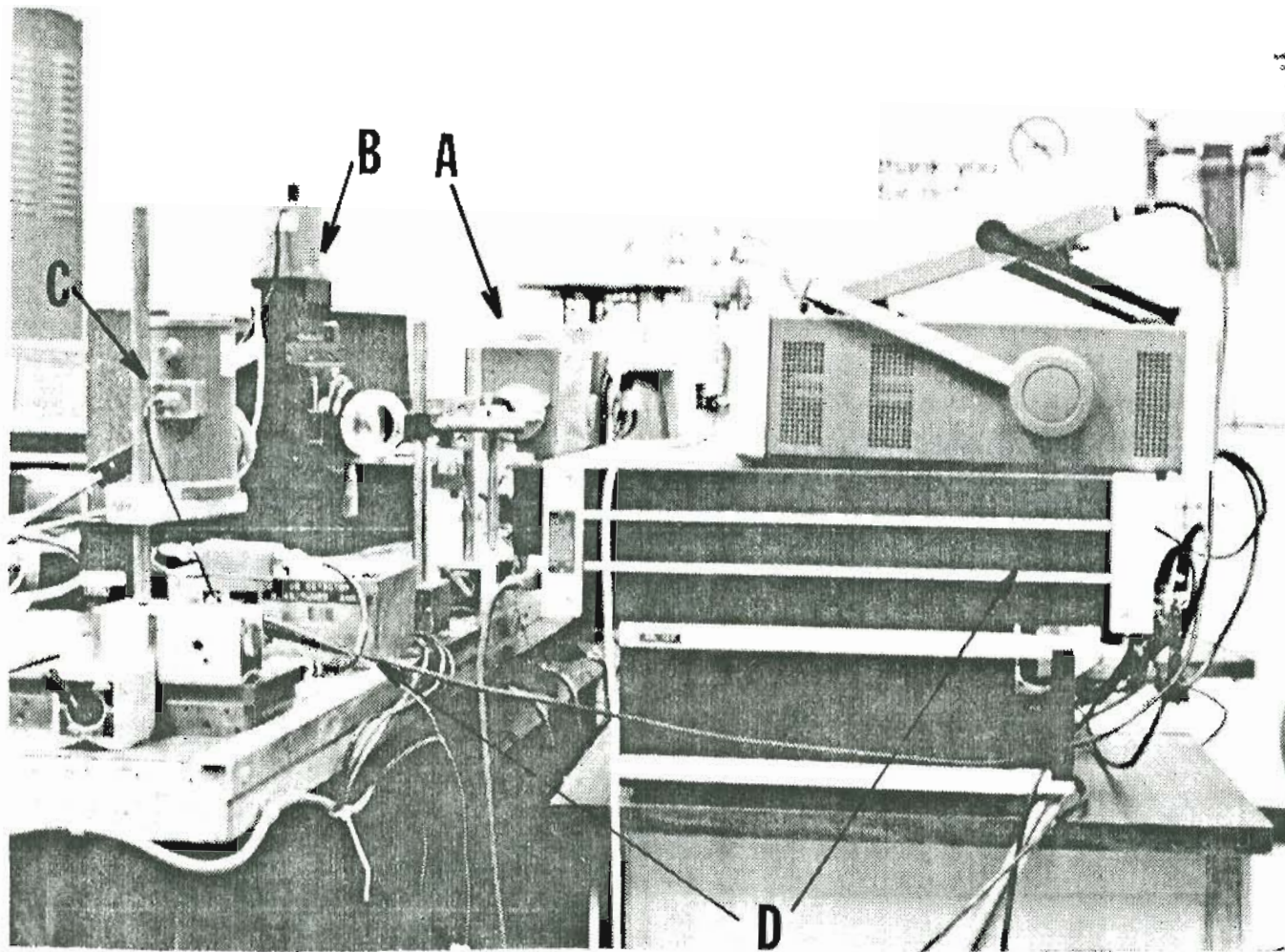


Figure 2-7: View of the near IR transmittance mapping system. A: monochromator; B: stepper motors assembly; C: Ge detector; D: electronics.

obtained for operation at 1.10 μm . Any higher order grating output is eliminated by a long-pass filter, with cut-off wavelength at 0.78 μm .

1.00 μm and 1.10 μm have been reported in the literature as used for EL2 mapping; we have used both, with the addition of 0.95 μm for samples with very low EL2. A wavelength of 1.37 μm has been used for stress mapping.

A number of different detectors have been tested: PbS photoconductive, pyroelectric, silicon photovoltaic, until a liquid N₂ cooled Ge photovoltaic detector has proved to guarantee the best performances.

Before photons can reach the detector, they must first travel a path through the sample. The monochromator exit slit in our system has been replaced by a circular hole, and radiation emerging from this is focussed on the wafer, to a beam spot < 0.5 mm in diameter, with a converging cone of optical aperture f/8 to provide paraxial conditions. Photons transmitted by the sample are collected by a lens, and brought to focus on the central part of the detector's receiving area.

Figure 2-8, a schematic of the apparatus, shows the sample wafer attached to a "wafer translation stage",

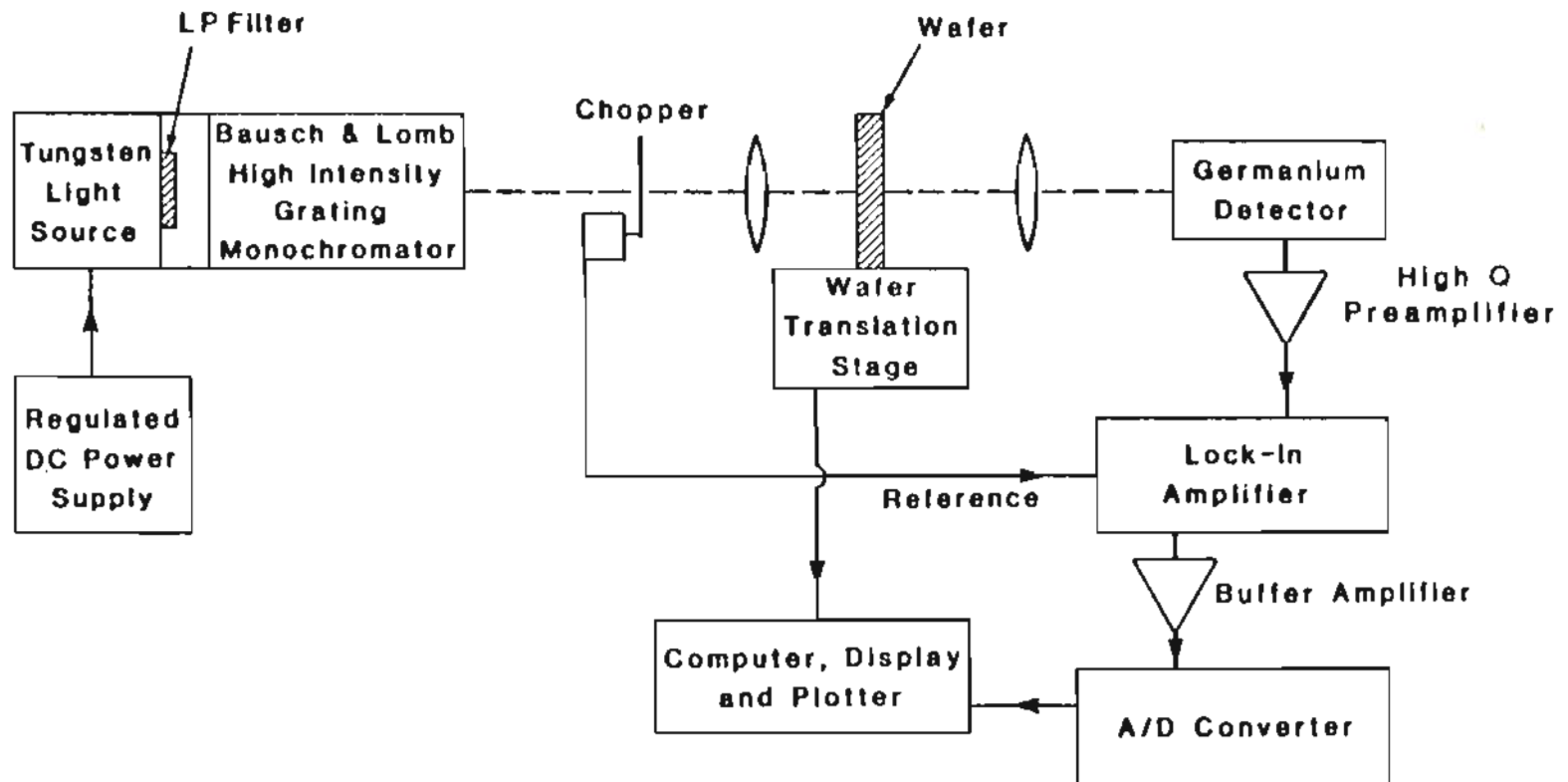


Figure 2-8: Schematic of the mapping system. For operation with polarized light polarizers are inserted between the sample and the lenses.

possessing several degrees of freedom. The X and Y displacements of the wafer in a plane normal to the optical path are effected by stepping motors assemblies having 100 mm travel range in 10 μm steps, these movements being under computer control. The cradle holding the wafer is also rotatable to make the sample surface exactly normal to the optical axis (alignment carried out by removing the long-pass filter and using the reflection from the wafer of the 2' order grating output), and the sample assembly can be electrically moved along the Z axis to the optimum focus.

After a 100:1 preamplification by a built-in amplifier, the signal is fed into a tuned amplifier (Q factor = 5) peaked at the chopping frequency of 630 Hz. The light chopper is a small vibrating fork that, apart from being extremely stable, provides a sinusoidal signal with extremely reduced harmonic content. This results in the best operational use of the following lock-in amplifier. Because of the first narrow band amplification at this point of the signal path, the measured signal to noise ratio is greater than 80 dB. The signal is then processed by a lock-in amplifier, whose output is a DC voltage proportional to the rms value of the AC signal. This DC voltage is then acquired

by the computer controlling the measurement by means of a 12 bit A/D converter.

The procedure developed for the analysis of a sample wafer is as follows:

- (1) the X-Y coordinates of the center of the wafer are established with reference to X-Y values in various directions at which a computer program recognizes the wafer edge. The geometric center is so established to $50 \mu\text{m}$.
- (2) The transmittance I_{r0} at the wafer center is measured, with 200 values digitized, averaged, stored. The sample is then translated out of the way, and the value of I_0 similarly recorded as an average over 200 digitized values. Thus the value $T = I_{r0}/I_0$ is now well known at one location.
- (3) The lock-in gain is now boosted by a factor G , which may (depending on how constant EL2 is over the area) be set to be 5,10, up to 100. The lock-in offset control is used to set its output to zero. This baseline subtraction has the effect of freeing bits in the A/D converter and thus increasing digitizer accuracy and improving the overall signal to noise ratio of the

system by allowing relatively high gain operation.

- (4) The wafer mapping can then begin. Our Apple II minicomputer stores digitized values ΔT of the amount by which the lock-in output changes from zero as various locations on the sample are visited in sequence.

The voltage range of ΔT is of course proportional to the factor G by which the lock-in gain was raised. During the latter part of each 0.2 second dwell time at a measurement location, 25 samples are collected for digitizing. These values of ΔT can then be converted into corresponding values of

$$T = (I_{T_0} + \Delta T/G)/I_0 \quad (13)$$

for the various locations in the chosen mapping array. Such data can then be reexpressed as the absorption coefficient through Eq. (7), and so to the "equivalent neutral EL2 concentration". Use of the gain factor G in measuring the change of transmittance between the designated central location and the various other locations is essential to provide an increase in the precision with which N^0 and its spatial variations can be determined under "optically thin"

conditions, to an extent that inevitably becomes eventually limited by the detector noise.

The mapping sequence typically makes measurements for a 49x49 array at about 2000 locations, the order being from left to right along rows taken in sequence from top to bottom. The interval between points is 1 mm when mapping 2" wafers, and is increased to 1.5 mm for 3" wafers. The 49x49 square grid is ideally overlaid on to the circular wafer, and the controlling program ignores those points falling outside the wafer surface. This point by point scan can be completed in less than 20 minutes, by carefully timing the translation motor instructions with respect to the lock-in time constant (10 ms) and to the A/D conversion cycle.

One program, which has been compiled for faster execution handles all the available options: 2" or 3" wafers, transmission mapping (for stress analysis) and absorption coefficient mapping (for EL2 measurements).

When the scan is completed the set of data representing either the local absorption coefficient, in units of cm^{-1} , or the fractional transmittance, are stored on a floppy disk, along with information identifying the sample. The results are immediately available as a three shading map on

the computer screen, as shown by Fig. 2-9; the data on the diskette are then usually plotted on paper, as a six level map of the kind shown in Figure 2-10.

This figure typifies the format with which all maps are presented. Above the actual wafer map one can read, from top to bottom, the identification of the sample, followed by its diameter and thickness. Then the wavelength at which the measurement was done is reported, as well as the mean absorption coefficient across the wafer, the calculated mean EL2 concentration and the experimental mean transmittance. For transmission maps mean absorption coefficient and EL2 are obviously not given. When information about EL2 are pertinent, one can see below the wafer map the shading step used for the map, in units of inverse cm, the lower and upper shading levels, in inverse cm and EL2 concentration.

The two portions of straight line that interrupt the circumference of the wafer indicate the position of the flats on the wafer: they are used as orientation marks, since they are perpendicular to the $[011]$ (major flat) and $[01\bar{1}]$ (minor flat) directions.

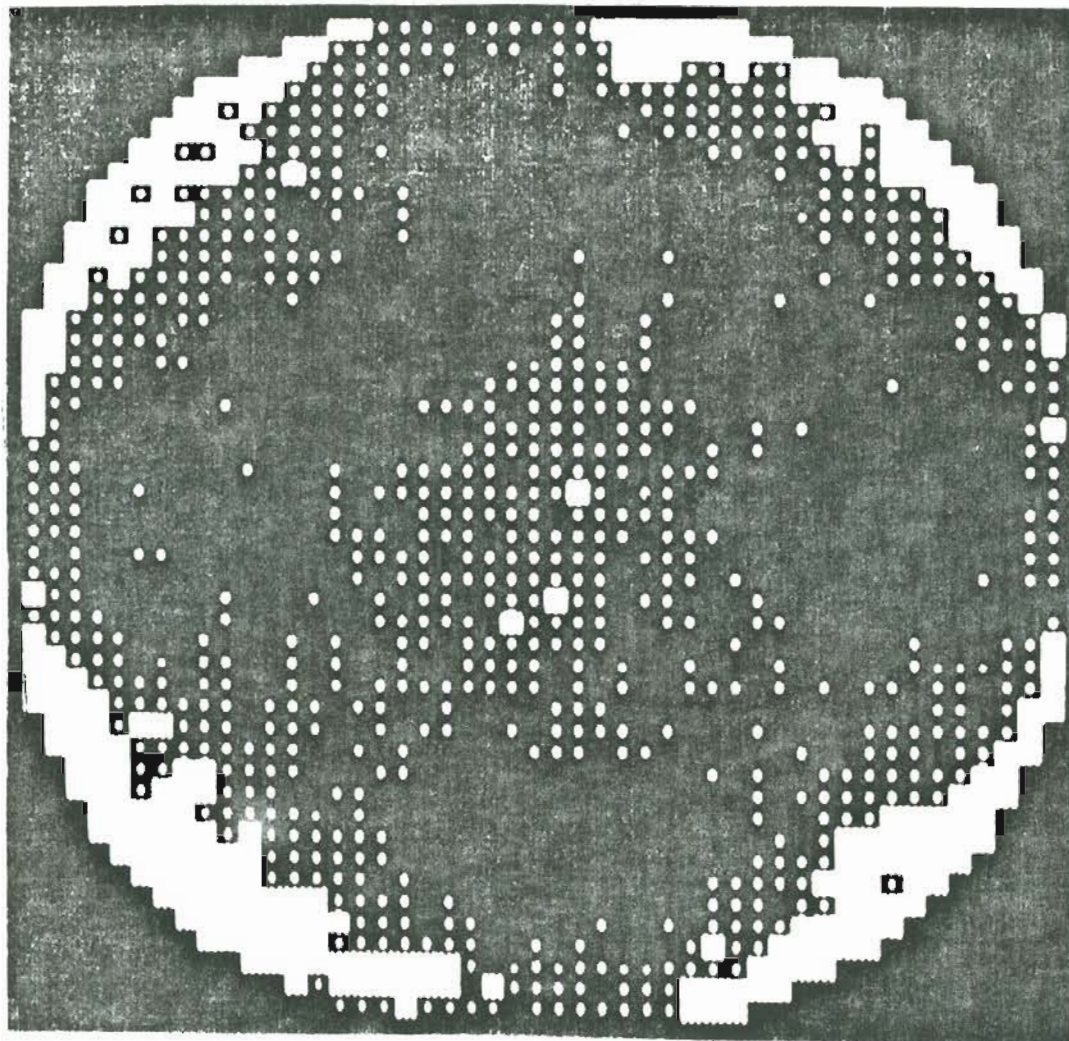
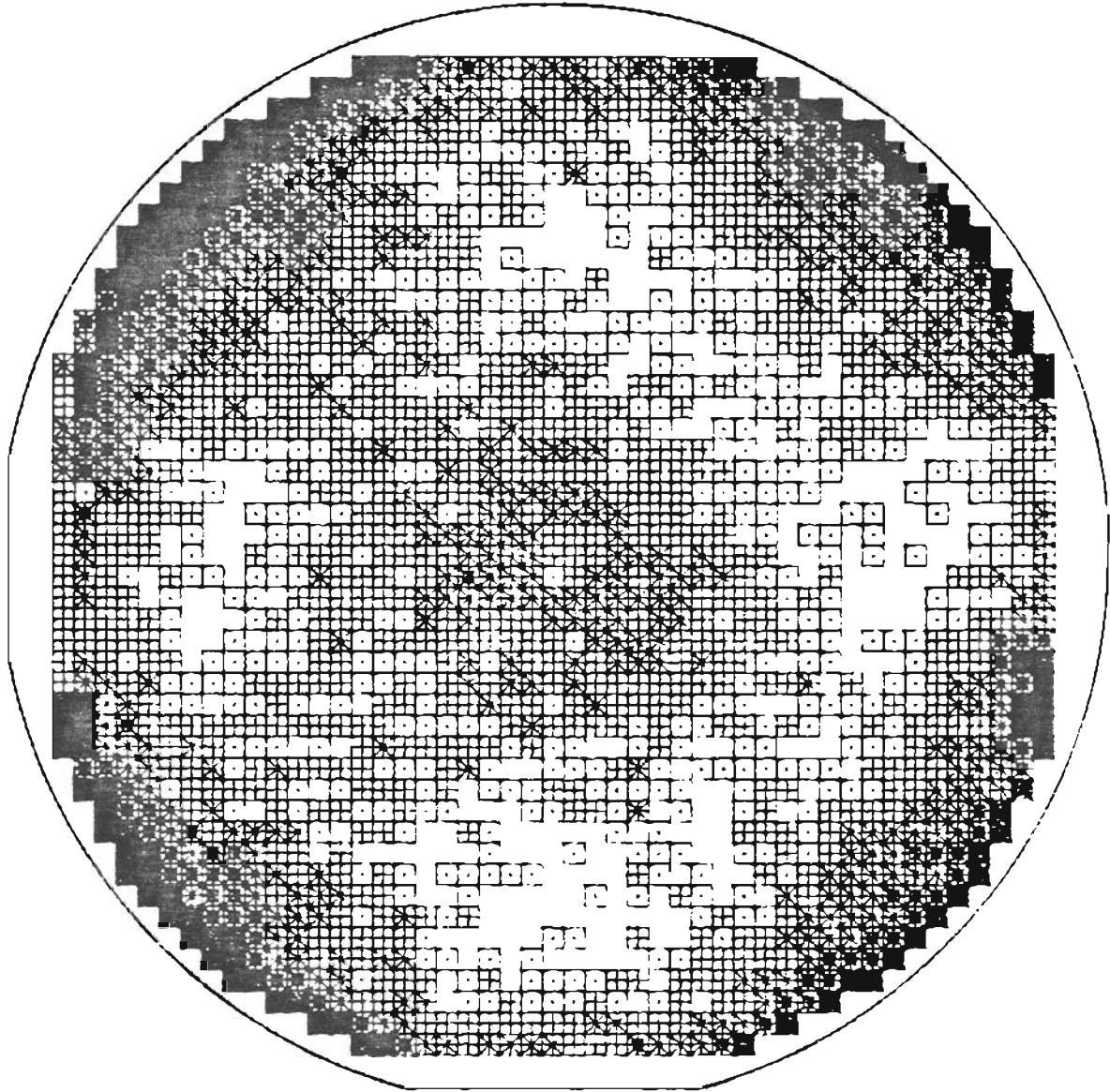


Figure 2-9: EL2 map visible on the screen of the Apple Monitor. Black areas correspond to low EL2, while increasing white dot sizes imply higher EL2.

WAFER SUM1501232/B2
DIAMETER : 76 mm
THICKNESS : .52 mm
WAVELENGTH : 1000 nm
MEAN ABS. COEFF. : 1.353 cm⁻¹
MEAN EL2 : 11.27 E15 CM⁻³
AVERAGE TRANSMISSION : .484

56



6 LEVEL SCALE, STEP = .02 cm⁻¹
□ ABS. COEFF. < 1.31 cm⁻¹ EL2 < 10.81E15 cm⁻³
■ ABS. COEFF. > 1.39 cm⁻¹ EL2 > 11.58E15 cm⁻³

Figure 2-10: EL2 map, as printed by the HP plotter of the system. The six level shading, from white to completely dark pixels, indicates increasing EL2 concentration. The limit values of α and NEL2 are reported in the lower left corner of the plot.

TABLE II

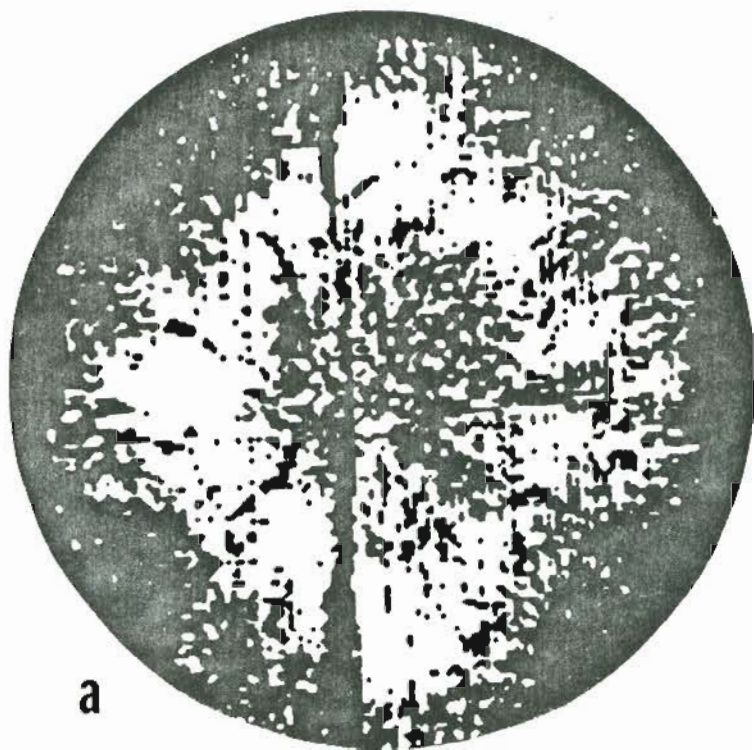
Symbols used in the EL2 maps, MV = mean value, ST = step

	$x < MV - 2ST$		$MV \leq x < MV + ST$
	$MV - 2ST \leq x < MV - ST$		$MV + ST \leq x < MV + 2ST$
	$MV - ST \leq x < MV$		$MV + 2ST \leq x$

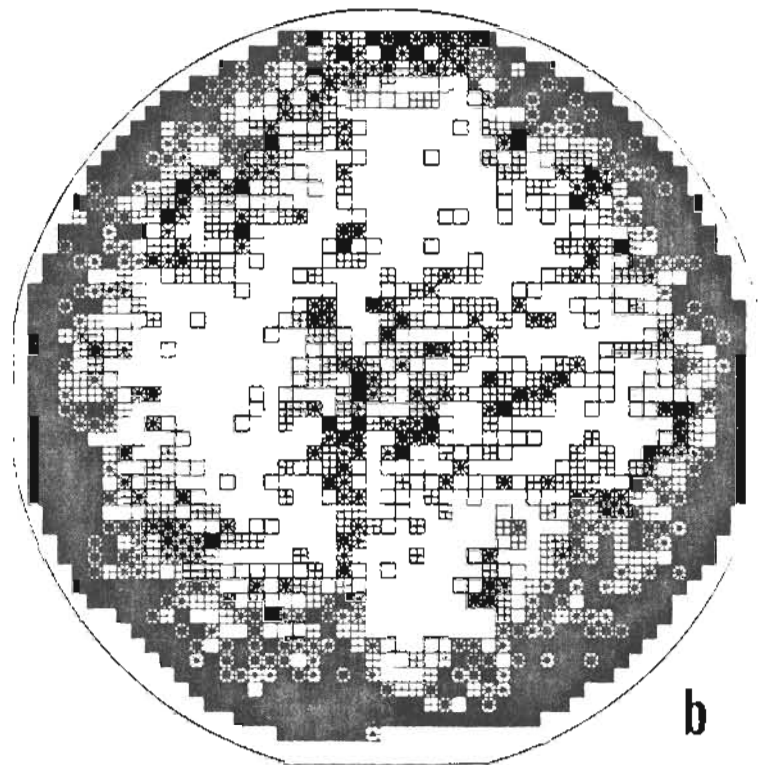
To the best of our knowledge, this is the only experimental system with the capability to provide quantitative informations about the EL2 content in thin GaAs wafers. The possibility of an independent calibration of our system has thus not yet materialized.

Machines that provide qualitative maps of EL2 in thin wafers, however, do exist, and we were happy to compare the resulting maps.

J. Windscheif et al. [5] have utilized a Si linear array of detectors and a broad band light source to get maps



a



b

6 _LEVEL SCALE. STEP = .075 cm-1
 □ ABS COEFF. 1.05 cm^{-1} EL2 $10.31 \text{ E}15 \text{ cm}^{-3}$
 ■ ABS. COEFF. >math>1.05 \text{ cm}^{-1}</math> EL2 >math>12.10 \text{ E}15 \text{ cm}^{-3}</math>

Figure 2-11: Transmittance map of a 0.5 mm thick GaAs wafer, as obtained by a system employing a linear array of Si detectors (a). EL2 map of the same wafer, as obtained by the system described in the text (b).

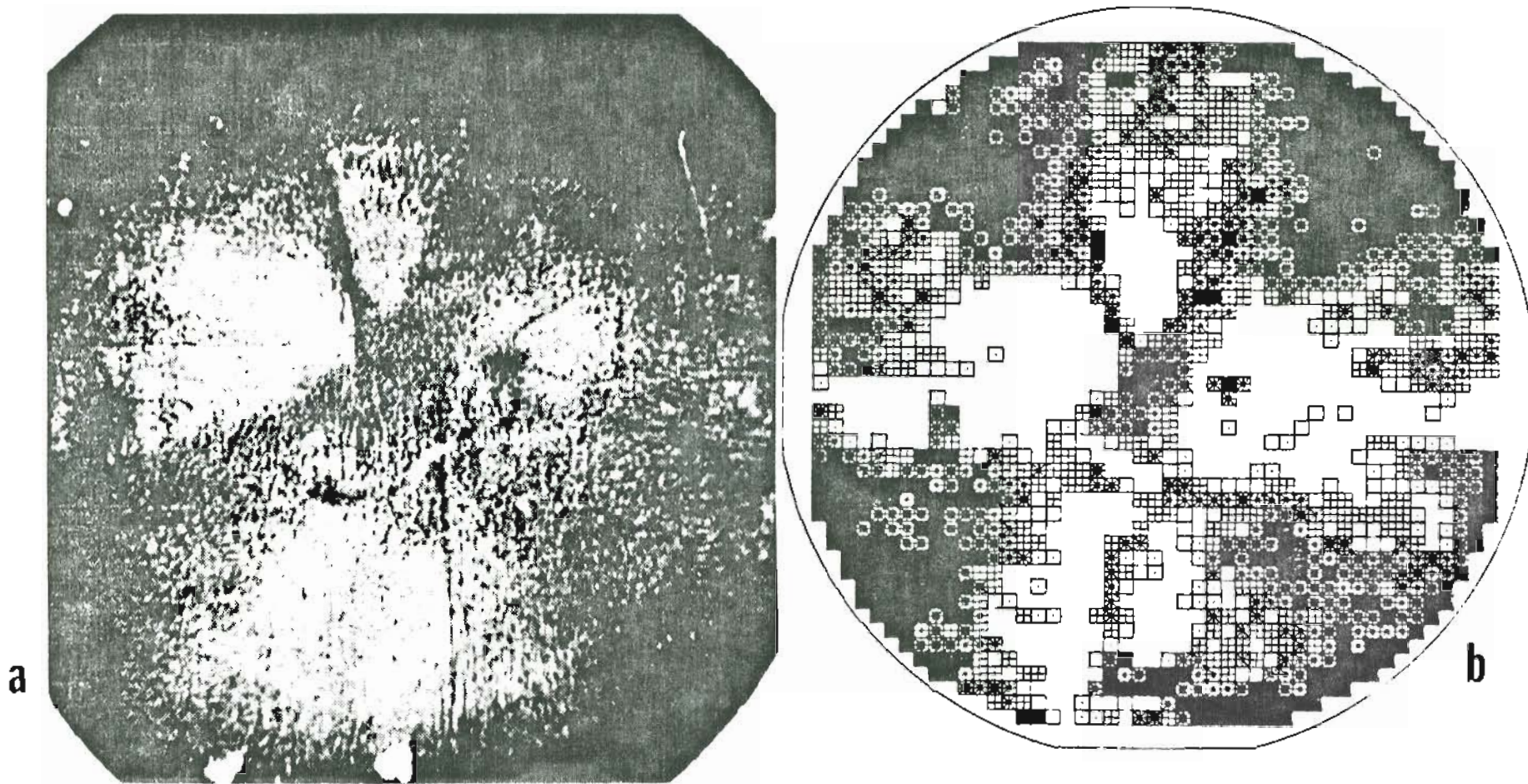


Figure 2-12: Transmittance and EL2 maps of the same thin wafer. (a) obtained by a Si based, commercial instrument; (b) obtained with the OGC set-up. We are indebted to Spectrum Technology for Part (a).

of the absorption coefficient . Given the spectral ranges of the silicon detector sensitivity and of the GaAs extrinsic and intrinsic absorptions, they are able to estimate the integrated absorbance of the sample in the whole 0.9-1.1 μm range. Figure 2-11 shows the same wafer, as mapped by the silicon based machine (part (a) of the figure) and by our system (part (b)). In this case we have mapped the sample at 0.92 μm , in order to get a numerical value close to the one reported by the other group. Although the spatial resolution of the West Germany group is higher than that of our system, they obviously cannot relate the broad range absorbance to a precise EL2 content.

Figure 2-12 shows another pair of maps, the one at left being obtained by a silicon Vidicon based machine sold by Hamamatsu Corp. The measurement is fast and the spatial resolution is high, but no numerical information is obtainable.

E. VAPOR-PHASE KOH DISLOCATION ETCH

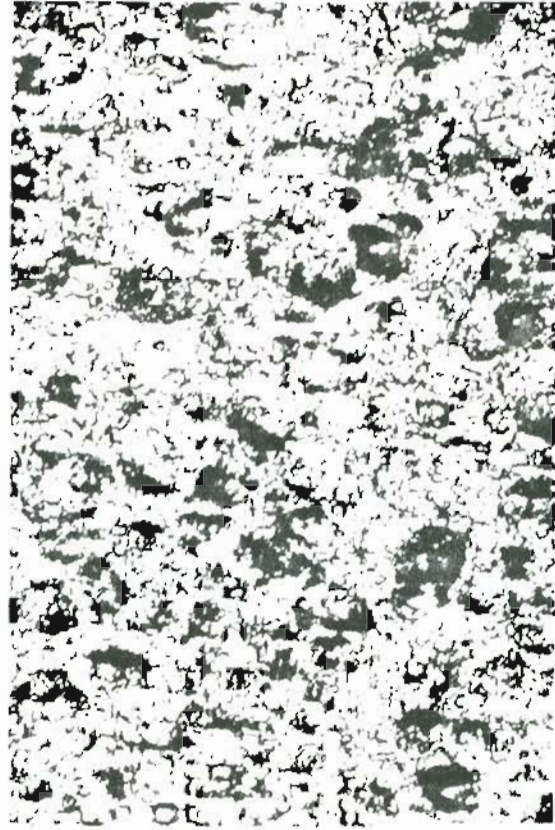
Dislocations are line defects almost always present in crystalline materials. In the simplest case, they can be regarded as the boundary between atomic planes displaced with respect to their ideal position.

Experimentally one often refers to the density of dislocations, that is the number of dislocation lines that intersect a unit area of the surface of the crystal. The density ranges from zero, in dislocation-free silicon crystals, to about 10^4 cm^{-2} in medium quality LEC GaAs crystals to 10^8 cm^{-2} in deformed metallic crystals.

One of the most widely used ways to reveal dislocations is chemically etching the sample: suitable etchants preferentially dissolve the crystalline matrix at points where the dislocation line intersects the surface, creating a characteristic etch pit. For GaAs, two etchants used are molten KOH [18] and the aqueous A/B etch [19] used at room temperature or slightly above (60°C). While the A/B etch is by far easier to use than KOH, the latter has the advantage of producing much more well defined pits, of the kind shown in the microphotograph in figure 2-13 (a).



a



b



c

Figure 2-13: Different pits produced by identical experimental conditions. The magnification of the micrographs is 516x (a); 172x (b) and (c).

On the other hand, molten KOH presents many disadvantages related to a well known lack of reproducibility and uncontrollable water content of the source KOH [26]. For instance, micrographs (b) and (c) in Fig. 2-13 show the pits produced by nominally identical etching procedures with KOH. In the worst case, the water content may be so high that breakage of the sample during the recrystallization of the melt is not an unusual event, because of the volatilization of water [26]. To overcome these drawbacks, a mixture of 50 mole per cent KOH and 50 mole per cent NaOH has been proposed [26], in the form of a bath to be used from 300 to 400 °C, with the clearest etch patterns being developed at 350 °C. This new etchant has been tried in our lab, but the results have been very poor.

In an attempt to eliminate the deficiencies of this etch and to avoid the customary procedure of dipping the sample in molten KOH or KOH/NaOH, the vapor ascending from a KOH melt has been tested as an etch agent.

It has been found that, from a temperature of about 380 °C, the vapor is energetic enough to etch an exposed surface uniformly in the same way the melt does, although at a rate about 5 times slower. This reduced speed can obviously be

useful when etching thin GaAs epitaxial films. Moreover it is possible to confine the spreading of the vapor to a specific area, while capping the top surface of the wafer.

For this vapor-phase etch, the KOH charge is contained in a graphite crucible which fits tightly into the bottom of a graphite cylinder. The wafer rests in a recessed groove around the periphery of this cylinder. The top surface of the wafer is coated with a film of silicone grease, which prevents a thick layer of (commercially available) silicone rubber from sticking to the sample. Once cured, the silicone rubber maintains the etch vapor inside the crucible, and prevents any damage to the upper surface of the wafer. After the etching, the silicone layer is brittle and can be easily removed. Then the wafer is rinsed with de-ionized water, trichloroethylene is used to dissolve the greasy coat and a final methanol rinse is applied.

The same charge of KOH can be used at least four times, without any detectable change in etch rate, for the process is far less sensitive to contamination of the melt. Since the sample is not abruptly immersed in the hot melt, but the ensemble crucible-wafer is brought to temperature and then slowly cooled down, the thermal stress on the

sample is greatly reduced.

Exposure to the vapor for 120 min at 400 °C develops the etch pit pattern on a (100) GaAs surface shown in Fig. 2-14. The typical hexagonal pit configuration developed by molten KOH can be recognized, as well as the grouping of dislocation pits in a cellular network.

F. ETCH PIT DENSITY EVALUATION

After the etching process, the customary procedure of etch pit counting to infer the dislocation density [27] is tedious and intrinsically not accurate.

In fact, a number of microphotographs need to be shot at different, strategical points on the sample. A balance is required between high magnification, which shows a reasonably low number of pits per picture but can lead to dramatic variations in the resulting etch pit density (EPD) over a range of a few hundred μm , and low magnification -that is statistically more satisfying, but with which the number of hardly individually resolved pits can be very high. Then the operation of counting the pits in a large number of pictures is obviously time consuming and prone to human error. As a result, a 50 % inaccuracy in the evaluation of EPD is still considered acceptable.

The technique here developed is based on the fact that pits formed on GaAs by molten KOH are concave in shape, so that they are less reflecting than the surrounding surface. Accordingly the intensity of the light reflected to the film in a camera equipped microscope is found to be a decreasing,

linear function of the number of pits in the field of view of the objective. In these conditions, the time required to get a correct exposure is proportional to the local etch pit density.

Operating in the automatic exposure mode two micrographs are needed to obtain the coefficients of the linear relation between EPD and exposure time, and it is then sufficient to simulate the shooting of pictures at points of interest on the sample to get a map of the EPD.

Reducing the light intensity, the exposure time can be made long enough to reduce any residual effect of the reaction time of the operator or, better yet, an electronic timing device could be fitted to the microscope with minor modifications to the instrument itself.

The precision of the measurement is limited by the linearity of the microscope metering system and by the accuracy with which the pits can be counted on the micrographs actually shot.

Figure 2-14 shows the results obtained with two different GaAs wafers observed through a Zeiss Ultraphot II microscope, at magnification of 512x and 128x. In both cases a good linearity is obtained between exposure time and etch

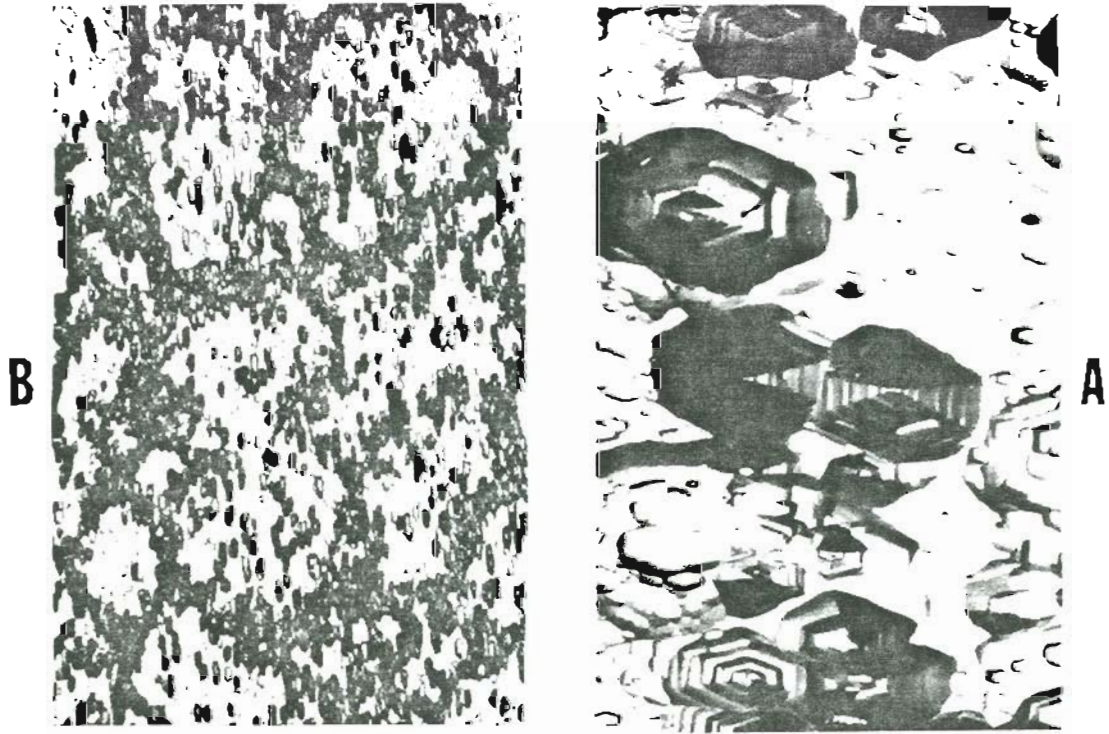
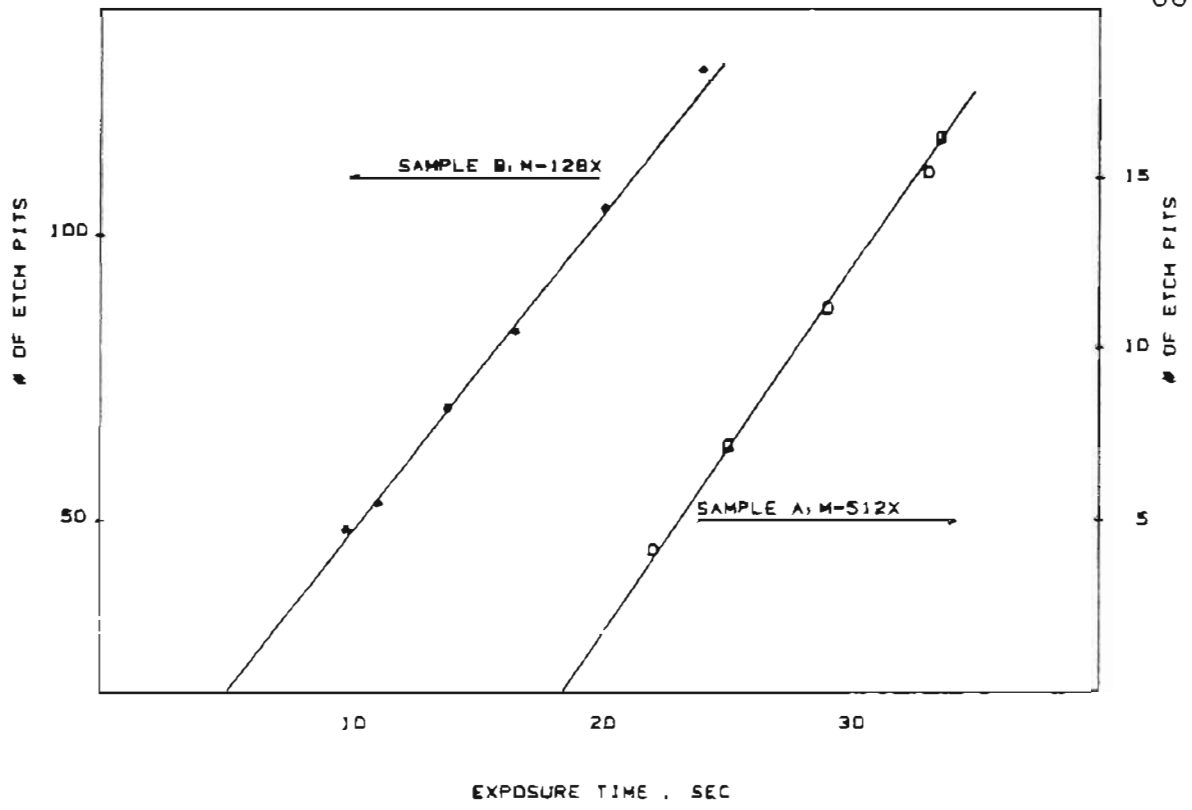


Figure 2-14: Number of etch pits in field of view of a microscope objective versus the correct exposure time (top) of micrographs of the etched surface (bottom).

pit density.

In most cases two micrographs can be satisfactorily used to deduce with good precision the parameters of the EPD versus time relation.

G. DISLOCATION MAPPING

The two previous sections were focussed on the use of KOH to reveal dislocations and how to deduce their density in a fairly reproducible manner.

Sometimes the spatial pattern of the dislocation distribution is at least as important as their density, but the techniques to get maps of the dislocation distribution are not very sophisticated.

After the etching process, one can either take a macrograph of the entire wafer, as shown in the upper part of figure 2-15, or even just photocopy the wafer with a good copy machine (bottom of figure 2-15). In both cases, the results do not provide more than the gross pattern of the dislocation distribution. The A/B etch is not suited for such macroscopic measurement, since the etch pits are much smaller than those produced by KOH.

Dissatisfied with these results, and being more interested in the exact spatial pattern of the dislocation distribution than in the actual dislocation density, I thought that our IR mapping machine, operated at the right wavelength, should have been able to discriminate between

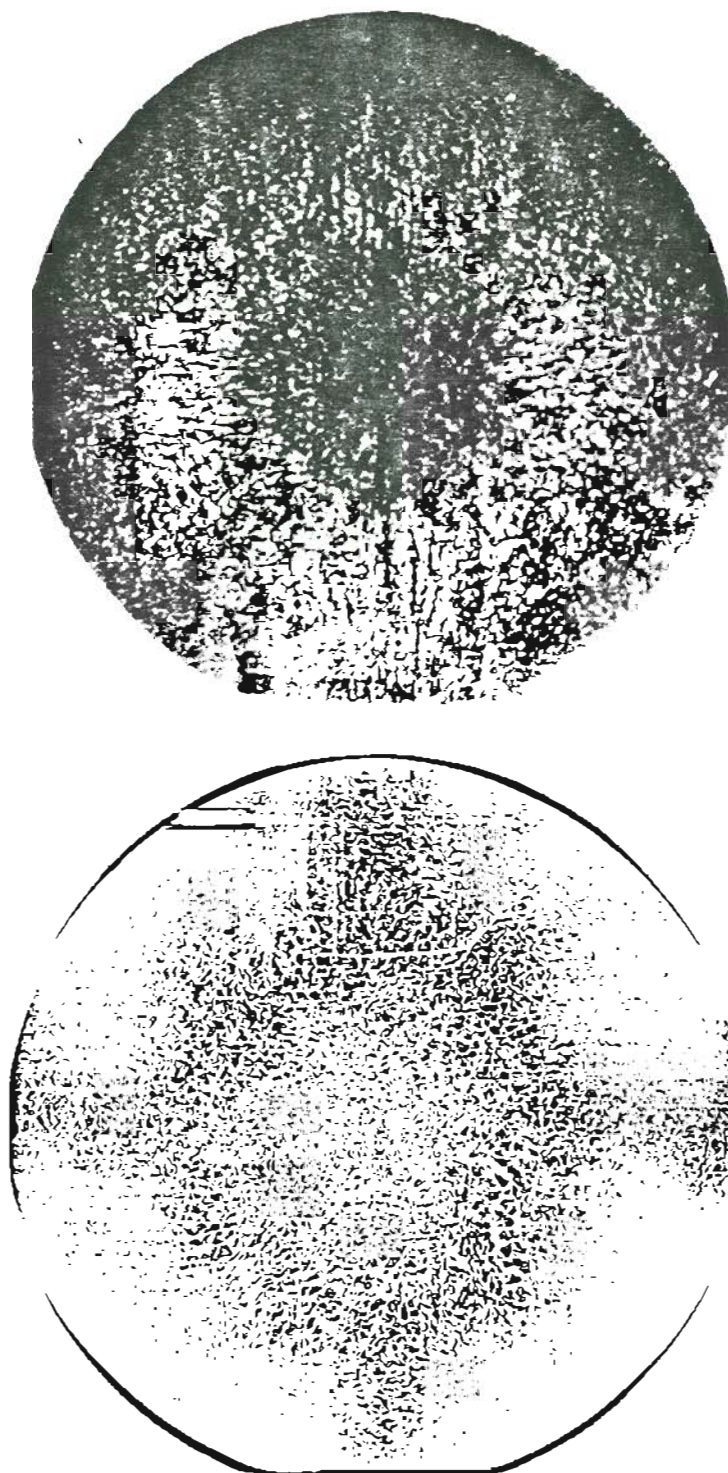


Figure 2-15: Different ways to produce macrographs of etched wafers: close-up photograph (top) and direct photocopy of the sample (bottom).

areas of low and high dislocation density on an A/B or KOH etched sample.

At sufficiently long wavelength, no other mechanism can provoke changes of the local transmittance, but the different surface roughness due to the etch pits, and the stress interference considerations discussed in Sect. 2.C.

The effect of pits on the surface can be considered as incoherent optical scattering, which modifies the transmittance of the sample. Operating at a wavelength of $1.45 \mu\text{m}$, where the sample is optically transparent, points of the wafer with a high dislocation density appear to be less transmitting than points with low or zero dislocation density.

The right part of figure 2-16 is the transmittance map of a 2" wafer, etched in KOH. The wavelength is $1.45 \mu\text{m}$, and the result can be compared with the left part of the same figure, produced by "photocopying" the wafer directly. Note that in the upper map low dislocation areas are represented as lighter (or white) shading, while in the photocopy they appear as dark zones. It is to be noted that the lowest shading (white) in the dislocation maps does not represent dislocation-free areas, but only zones of lowest dislocation

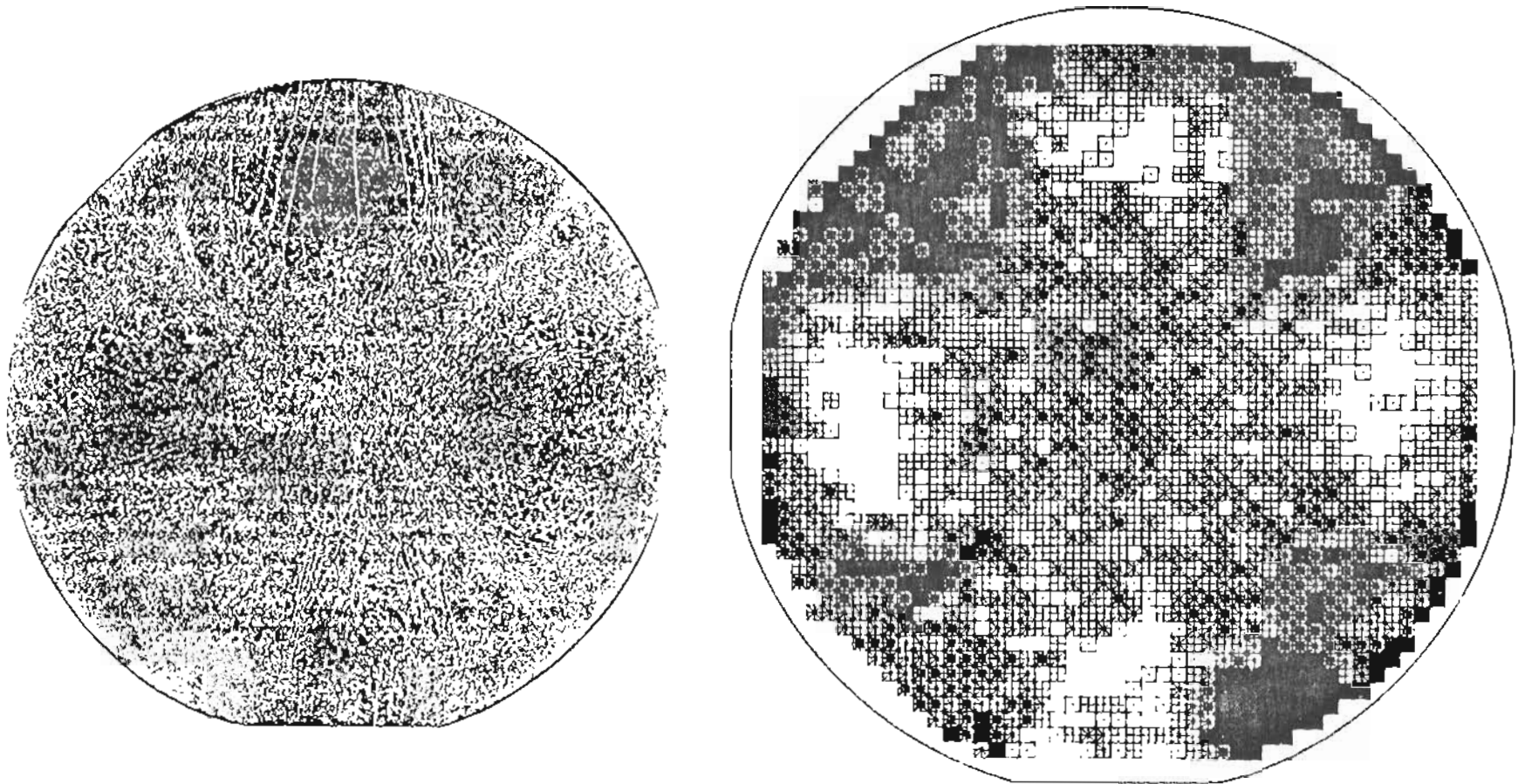


Figure 2-16: Comparison between a photocopy (left) and optical map (right) of the same KOH etched wafer. Low dislocation areas appear darker in the photocopy and lighter in the optical map.

density, which may be quite high in absolute value. In the few cases where white shading does indicate dislocation-free areas, attention will be drawn to this in the text.

Undoubtedly the optically deduced map carries more information than the simple process of photocopying the sample although it should be recognized that the latter is already an improvement with respect to whole-wafer photographs that appear in some recent literature [15,28,29].

It is of obvious interest to have some information on the ability of the system to discriminate between low and high dislocation areas. In this regard, the map has been reduced to its true dimensions (2" diameter) and superimposed upon the wafer, after some holes had been punched at interesting points (figure 2-17) in the map. Some micrographs have then been taken through the holes in the map.

It has been so determined that the lightest shading corresponds to about 1.0×10^4 dislocations per cm^2 , while the 5th level of shading corresponds to about $1.5 \times 10^4 \text{ cm}^{-2}$. With 6 levels of shading, then, we are able to resolve differences of EPD of about 10^3 cm^{-2} , although probably the

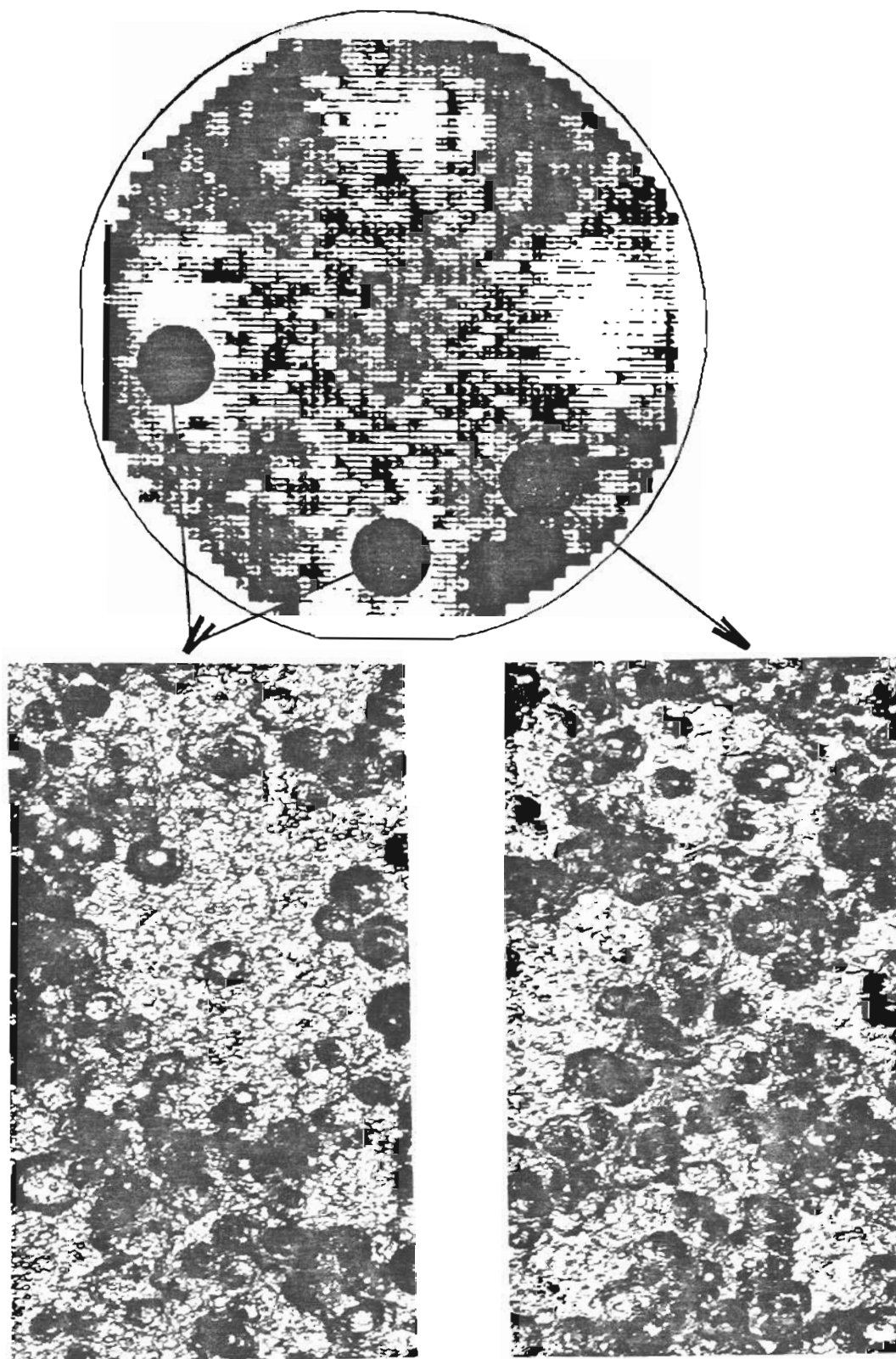


Figure 2-17: Evaluation of the resolving power of the dislocation mapping technique. The etch pit density was evaluated in points within the dark circles that appeared different in the dislocation map.

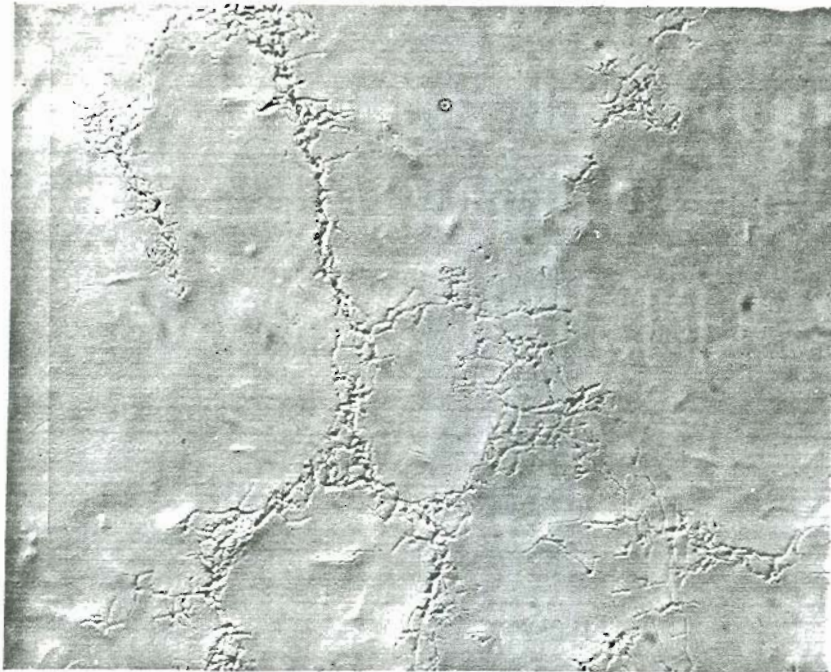
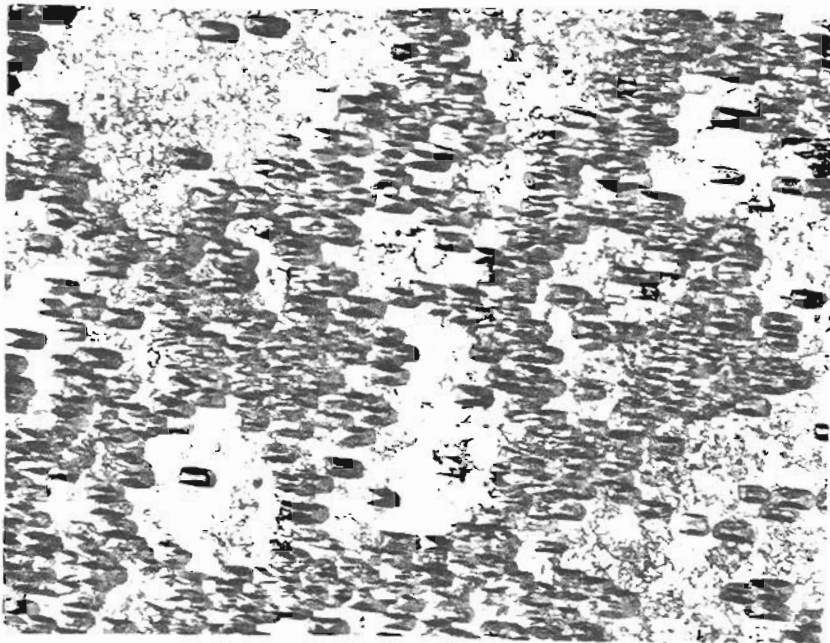
**a****b**

Figure 2-18: Cellular structure of dislocations in LEC GaAs. (a): as revealed by A/B etch, magnification 160x; (b) as revealed by KOH, magnification 182x.

system is capable of a higher resolution.

It may be of interest to note that, at the magnification of the two pictures in Fig. 2-17, one would need to be able to count the pits with a maximum tolerance of 3 pits to achieve the same resolution by eye.

As will be shown in the next chapter, both KOH and the A/B etch have been used with identical results to map the dislocation distribution. A brief discussion is in order here, to compare the results of etching a wafer with these two different etchants.

The two micrographs in Fig. 2-18 show A/B (a) and KOH (b) etch pits at different magnifications. In both micrographs the grouping of dislocations in cellular structures can be noted, as well as the different aspect of the etched features. The orientation and shape of the pits in the lower micrograph (b) are determined by the peculiar modality of action of KOH, which exposes the (111) arsenic planes (seen as the small triangular faces of the pits) more slowly than the (111) gallium planes (larger rhombohedral faces).

While material is removed by KOH around dislocations, the A/B etch works in the opposite way, attacking with

preference non-dislocated material. As a result the aspect of dislocation varies with their orientation with respect to the (100) surface of the sample. The aspect of differently oriented dislocations is seen in the micrographs of Fig. 2-19, all taken at the same magnification, $M = 512$. The feature labelled "a" is a long dislocation parallel to the surface, while the pit "b" represents a dislocation orthogonal to the surface. The conical pit "c" is the effect of the A/B etch on a dislocation inclined with respect to the (100) plane. The fact that the dislocation "a" is composed of small ovals is usually considered indicative of impurity segregation at the dislocation [19].

Despite the different mechanism, the large scale features of the dislocation distribution revealed by A/B are closely similar to those revealed by KOH, as already evidenced by Fig. 2-18.

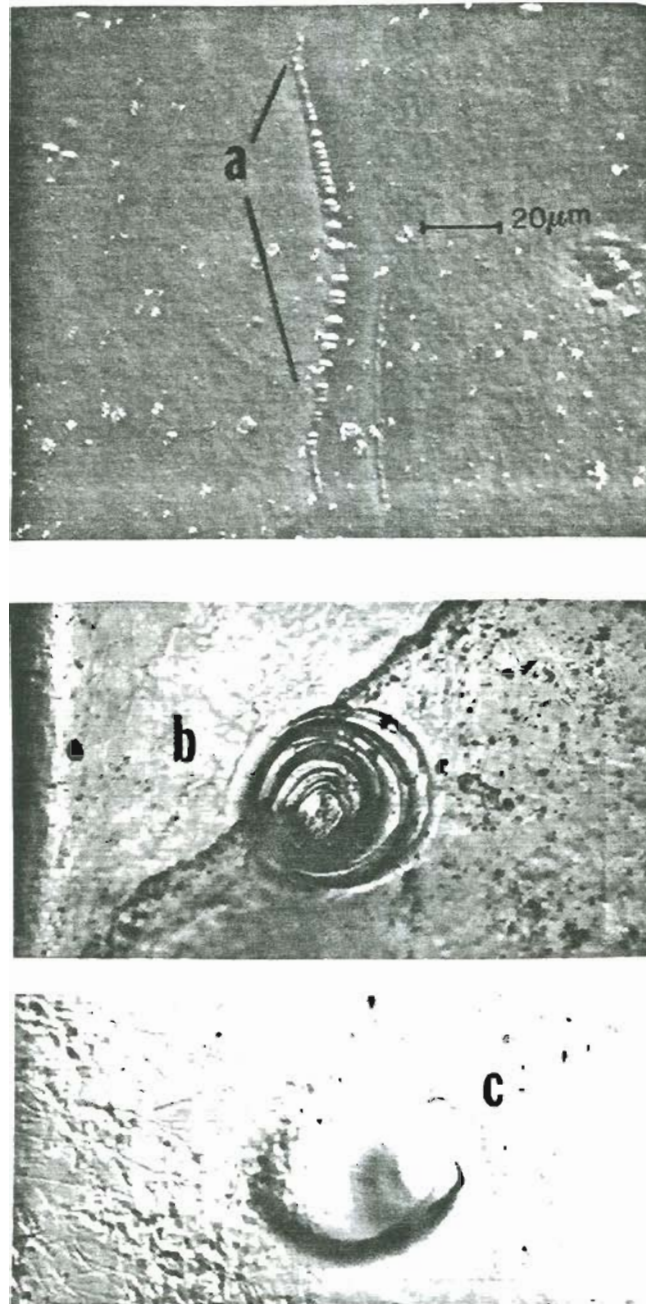


Figure 2-19: Different dislocations evidenced by the A/B etch: (a) a dislocation parallel to the (100) plane of the sample; (b) a dislocation perpendicular to that plane; (c) a dislocation inclined with respect to the (100) plane.

REFERENCES

1. J. S. Blakemore, J. Appl. Phys. 53, R123 (1982)
2. M. R. Brozel, I. Grant, R. M. Ware, and D. J. Stirland, Appl. Phys. Lett. 42, 610 (1983); M. R. Brozel, I. Grant, R. M. Ware, D. J. Stirland, and M. S. Skolnick, J. Appl. Phys. 56, 1109 (1984)
3. M. S. Skolnick, M. R. Brozel, L. J. Reed, I. Grant, D. J. Stirland, and R. M. Ware, J. Electron. Mater. 13, 107 (1984)
4. M. S. Skolnick, L. J. Reed, and A. D. Pitt, Appl. Phys. Lett. 44, 447 (1984)
5. J. Windscheif, M. Baeumler, and U. Kaufmann, Appl. Phys. Lett. 46, 661 (1985)
6. P. A. Leigh, I. P. Hall, C. R. Elliott, B. Wakefield, and M. H. Lyons, in Semi-Insulating III-V Materials: Kah-nee-ta 1984, edited by D. C. Look and J. S. Blakemore (Shiva Publishing, Nantwich, UK, 1984), p. 214
7. D. T. F. Marple, J. Appl. Phys. 35, 1241 (1964)
8. G. E. Stillman, C. M. Wolfe, and J. O. Dimmock, in Semiconductors and Semimetals, Vol. 12, edited by R. K.

- Willardson and A. C. Beer, (Academic Press, New York, 1977), p. 169
9. D. E. Holmes, R. T. Chen, K. R. Elliott, and C. G. Kirkpatrick, Appl. Phys. Lett. 43, 305 (1983); D. E. Holmes and R. T. Chen, J. Appl. Phys. 55, 3588 (1984)
 10. M. Duseaux and S. Martin, in Semi-Insulating III-V Materials: Kah-nee-ta 1984, edited by D. C. Look and J. S. Blakemore (Shiva Publishing, Nantwich, UK, 1984), p. 118
 11. A. Chantre, G. Vincent, and D. Bois, Phys. Rev. B 23, 5335 (1981)
 12. M. Kaminska, M. Skowronski, J. Lagowski, J. M. Parsey, and H. C. Gatos, Appl. Phys. Lett. 43, 302 (1983)
 13. G. M. Martin, in Semi-Insulating III-V Materials: Nottingham 1980, edited by G. J. Rees (Shiva Publishing, Nantwich, UK, 1980), p. 13
 14. G. M. Martin, Appl. Phys. Lett. 49, 747 (1981)
 15. A. S. Jordan, R. Caruso, and A. R. Von Neida, Bell Syst. Tech. J. 59, 593 (1980)
 16. N. Kobayashi and T. Iwaky, J. Cryst. Growth 73, 96 (1985)
 17. G. Szabo, J. Cryst. Growth 73, 131 (1985)

18. J. G. Grabmaier and C. B. Watson, *Phys. Sta. Solidi* 32, K13 (1969)
19. M. S. Abrahams and C. J. Buiochi, *J. Appl. Phys.* 36, 2285 (1965)
20. D. Brewster, *Phyl. Trans.* 60 (1815)
21. J. W. Dalley and W. F. Riley, Experimental Stress Analysis, (McGraw-Hill, New York, 1978)
22. S. R. Lederhandler, *J. Appl. Phys.* 30, 1631 (1959)
23. M. Born and E. Wolf, Principles of Optics, (Pergamon Press, Oxford, 1975)
24. C. W. Higginbotham, M. Cardona, and F. H. Pollak, *Phys. Rev.* 184, 821 (1969)
25. W. Kleber, An Introduction to Crystallography, (VEB Verlag Technik, Berlin, 1970)
26. H. Lessoff and R. Gorman, in "Semi-Insulating III-V Materials: Kah-nee-ta 1984", edited by D. C. Lokk and J. S. Blakemore (Shiva Publishing, Nantwich, UK, 1984), p.
27. Annual Book of Standard, Part 43 (Electronics), Standard Test Method F47-70 (ASTM, Philadelphia, 1981), p. 285
28. Y. Mita, S. Sugata, and N. Tsukada, *Appl. Phys. Lett.* 43, 841 (1983)

29. Y. Ishii, S. Miyazawa, and S. Ishida, IEEE Trans. El. Dev. ED-31, 800 (1974)

CHAPTER 3

DISLOCATION, STRESS AND EL2 DISTRIBUTIONS

A. Introduction

In this chapter experimental results obtained with the system described in Chapter 2 are shown and discussed.

Previous works that analyzed the EL2 distribution with respect to the dislocation pattern [1,2,3] considered the stress and related dislocation distributions somewhat more fundamental in nature than the EL2 pattern. Though I do not totally agree with this point of view, this chapter will discuss in section B data for stress and dislocation fields in GaAs wafers grown by the LEC technique, leaving the discussion of EL2 to section C.

B. Stress and dislocation distribution

It is necessary to spend some words on the theoretical studies of the stress distribution in GaAs ingots grown by the LEC technique, to provide a framework against which to evaluate our experimental results.

The main contribution to this subject has been provided by Jordan et al. [4] in 1980. Although other, more detailed analyses have been published [5,6], it seems to me that the original treatment of Ref. 4 gives a more physical insight.

In their work, Jordan et al. considered a perfectly cylindrical crystal pulled from a GaAs melt held at the melting point T_f . This growing boule is surrounded by an ambient fluid at temperature $T_a = \text{constant} < T_f$.

In a cylindrical coordinate system $(r, \vartheta, z; t)$ with the origin at the center of the crystal top, the partial differential equation for heat conduction takes the form

$$\frac{\partial T}{\partial t} = \kappa \left(\frac{\partial^2 T}{\partial r^2} + \frac{1}{r} \frac{\partial T}{\partial r} + \frac{\partial^2 T}{\partial z^2} \right) \quad (1)$$

where κ is the thermal diffusivity. The equation is independent of ϑ on account of the cylindrical symmetry of

the system.

The solution of this equation, with the proper boundary conditions, is expressed in terms of a series of Bessel functions of order zero. Such a solution includes time, pull rate, axial location, radius, convective and radiative heat transfer coefficients and the ambient temperature.

The temperature profile in the ingot induces a thermal stress field in the growing ingot as a result of spatially inhomogeneous thermal contraction. The stress components are obtained from classical thermoelastic theory assuming that the displacement is only radial, the center of the ingot suffers no displacement, and the lateral surface is free of traction.

Then the principal stress components are obtained on the basis of the equations

$$\begin{aligned}\sigma_r &= \frac{\alpha E}{1-\nu} \left(\frac{1}{r_0^2} \int_0^{r_0} Tr \, dr - \frac{1}{r^2} \int_0^r Tr \, dr \right) \\ \sigma_\theta &= \frac{\alpha E}{1-\nu} \left(\frac{1}{r_0^2} \int_0^{r_0} Tr \, dr + \frac{1}{r^2} \int_0^r Tr \, dr - T \right) \\ \sigma_z &= \frac{\alpha E}{1-\nu} \left(\frac{2}{r_0^2} \int_0^{r_0} Tr \, dr - T \right)\end{aligned}\quad (2)$$

where E , ν , and α are Young's modulus, Poisson's ratio and the linear thermal expansion coefficient, respectively.

The resulting stress components are plotted in Fig. 3-1, reproduced from the work of Ref. 4. Multiplication of the levels in the ordinate scale in the figure by $(\alpha E / (1 - \nu)) [(T_f - T_a) / 200]$ yields the stresses in absolute units.

The major mechanism by means of which dislocations are introduced during the Czochralski growth of GaAs is crystallographic glide caused by excessive thermal stress. Glide occurs when the shear stress acting in the (111) planes in the [110] directions exceeds the value of the so-called critical resolved stress.

If the stress magnitude is always lower than the critical intensity, dislocations will not be introduced, and at room temperature the stress will disappear completely. On the contrary, the fraction of stress exceeding the threshold set by the critical stress will be relieved by the production of dislocations, while the remainder will disappear when the ingot is uniformly at room temperature. At this point, though, the stress that had produced dislocations at high temperature will reappear, since the ingot is not at equilibrium with a flat temperature profile,

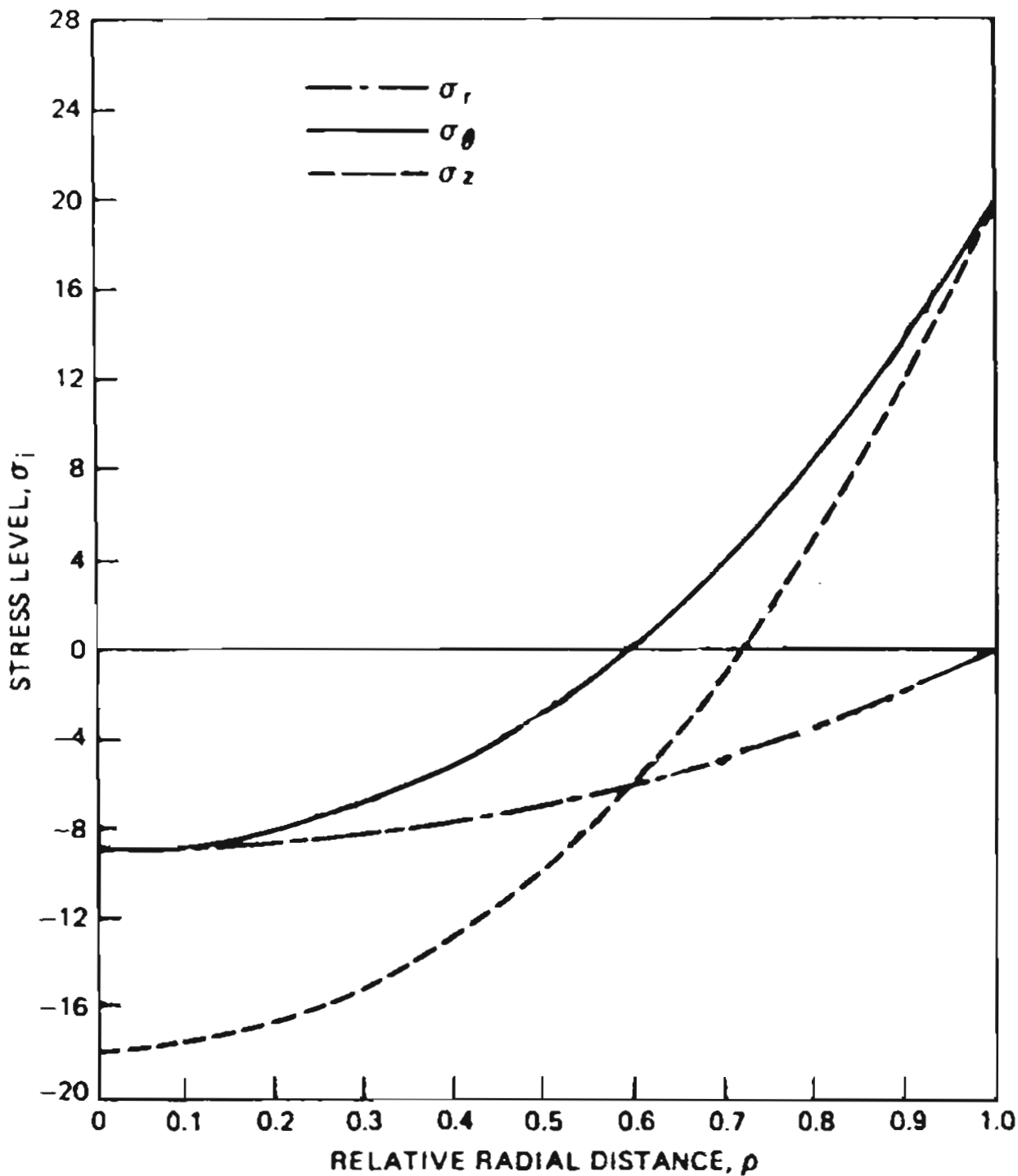


Figure 3-1: Radial, tangential and axial stress components as a function of the distance from the center in a boule of LEC grown GaAs. The ingot is in compression in the central core, and in tension in the periphery. Reproduced from Ref. 4.

due to the previous relaxation in the high temperature range.

This residual stress field can be optically detected as shown in Chapter 2, and it reproduces the configuration of the stress field that exceeded the critical stress at high temperature. The theoretical distribution, and an example of experimental pattern are shown in Fig. 3-2.

Keeping in mind that in these interferograms the shading of each pixel increases with the local transmittance, points of destructive interference correspond to white areas in the left map of Fig. 3-2. Since the only variables in Eq. (2-12) are the wavelength at which the interferogram is obtained and the thickness t of the wafer, this equation can be rewritten as

$$\tau = 1.7 \times 10^{10} (\lambda/t) (2n + 1) \text{ dyne cm}^{-2} \quad (3)$$

with λ and t in the same units (μm , for instance). Then the integer n is counted from the inner fringe in one of the four lobes in the [011] directions, since they are expected to sustain a local minimum stress intensity. In the case of Fig. 3-2 then, $n = 0$ is assigned to the fringe labelled "a".

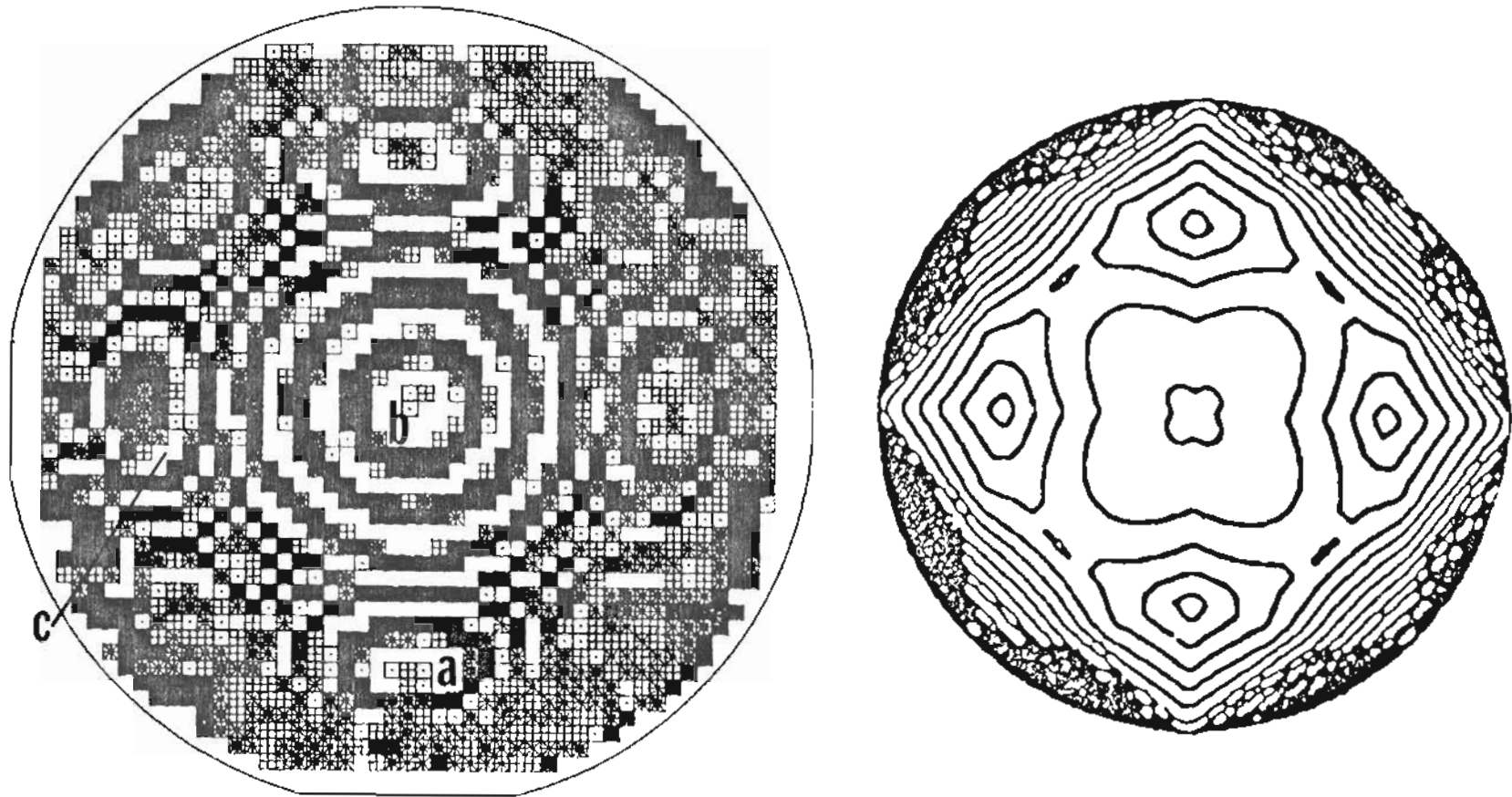


Figure 3-2: Experimental (left) and theoretical (right) stress contours. The latter reproduced from Ref. 5 .

Counting the fringes inward to the center, $n = 5$ is so assigned to the central fringe "b". Interestingly, not all the minima are equivalent, and for instance the lowest order fringe "c" towards the minor flat corresponds to $n=1$, indicating that at this minimum the stress intensity is distinctly higher than at the one near the major flat (a). Since the wafer was 0.65 mm thick and was analyzed with radiation at $1.37 \mu\text{m}$, the lowest stress intensity results to be 3.5×10^7 dyne cm^{-2} at the fringe "a"; at the crystallographically equivalent position of fringe "c" the stress level is 3 times higher, and it is 4×10^8 dyne cm^{-2} at the central fringe "b".

Although the value of the theoretically deduced stress is somewhat uncertain, due to the lack of precisely known input parameters, one can expect a peak stress intensity at the center of the ingot roughly in the range of 10^8 dyne/ cm^2 , with a ratio between this peak and the local minima in the [011] directions of some 5:1 to 10:1.

The details of the axial dependence of the stress distribution are less clear than its planar distributions: in fact all theoretical models [4,5,6] assume a quasi-steady state situation, so that different axial positions are made

almost equivalent with an appropriate temporal shift: the situation at the point $z = z_0$ at a time $t = t_0$ will be reproduced at $z = z_1$ at a time $t_0 + (z_1 - z_0)/p$, where p is the pull rate of the crystal. As a result, apart from a slight increase of the stress from top to bottom of the ingot, no radical modification is expected.

In connection with the axial dependence of the stress field, we are going to examine at first two sets of wafers cut at different positions from two ingots grown by Cominco. The first one is a 2", undoped crystal that was not annealed, while the second is a 3" ingot, wholly annealed. Pertinent quantitative parameters of both ingots are shown in Table II.

TABLE III

Ingot/wafer	ingot radius, (mm)	stress $\times 10^8$ dyne cm^{-2} (minimum/peak)	r_{min}/r
638/5	27	0.53 / 5.8	0.78
638/72	30.5	0.53 / 7.9	0.69
638/190	31.5	0.53-1.6* / 5.6	0.71
638/215	30	0.53-1.6* / 4.6	0.73
925/10	41	0.43-2.1* / 5.5	0.80
925/38	41.5	0.43 / 3.8	0.77
925/71	43	0.43 / <1.3	0.63
925/105	47	0.43 / <1.3	0.56

* double entries indicate that the crystallographically equivalent minima do not sustain the same stress

Putting aside for the moment considerations about the planar distribution, the two crystals show a definite trend from top to bottom. The stress in crystal No. 925 is strongly decreasing towards the tail end, and in fact the peak magnitude is likely to be less than the value of 1.3×10^8 dyne cm^{-2} quoted in the table, since no central fringe could be clearly resolved. Although the situation in crystal 638 is less clear-cut, the stress magnitude seems again to be decreasing at the tail end of the ingot, in contrast to what is expected by the various theoretical

models.

Definite discrepancies from the analytical models are noted in the position of the minima: in general they are located between 70 and 80% of the radius of the as-grown ingot, while the theory does not allow for minima further out than $0.7 r$; then their position gets closer to the center towards the bottom of the ingots, the opposite being expected. The latter phenomenon is more apparent in tail wafers from crystal 925, and it is accompanied by a lower peak intensity of the stress. We may note that in most of the cases shown here the stress magnitude is slightly higher than expected, and it is reasonable to wonder whether there is a relationship between the low stress in wafers 71 and 105 and the "correct" position of the minima.

Stress maps of these two crystals are shown in Figs. 3-3 and 4, for ingot 638 and 925 respectively.

It is finally interesting to note that the stress distribution in wafer 10 of crystal 925 is off center, but it appears to be perfectly centered in the following sample, No. 38.

Before going on, we have now to reassure ourselves that a good correlation between stress and dislocation maps

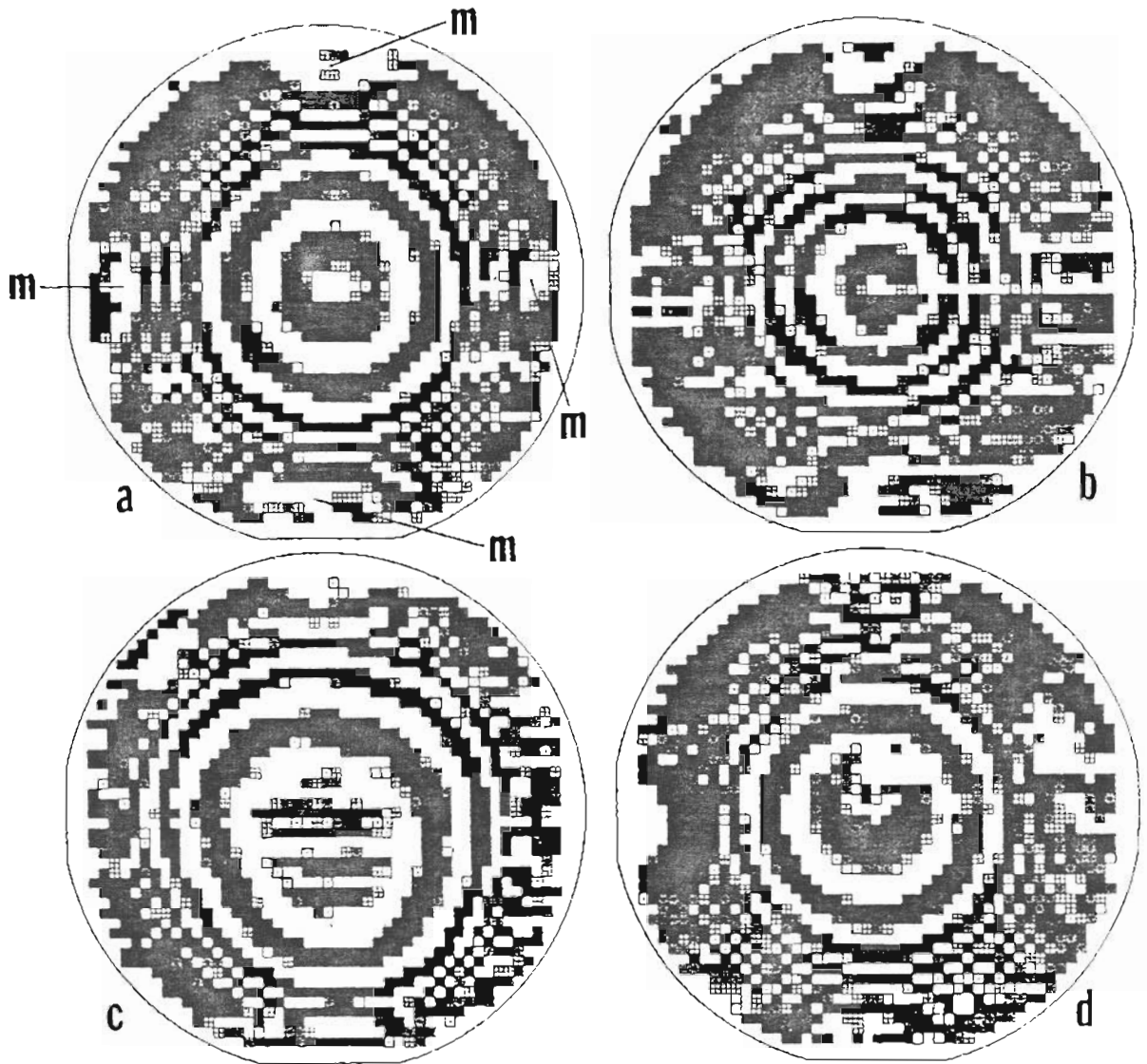


Figure 3-3: Stress contours in some wafers cut at different positions along the length of an LEC ingot. (a): wafer No. 5; (b): wafer No. 72; (c): wafer No. 190; (d): wafer No. 215. The local minimum stress (e.g. (m) in part (a)) is near the edge of the wafer.

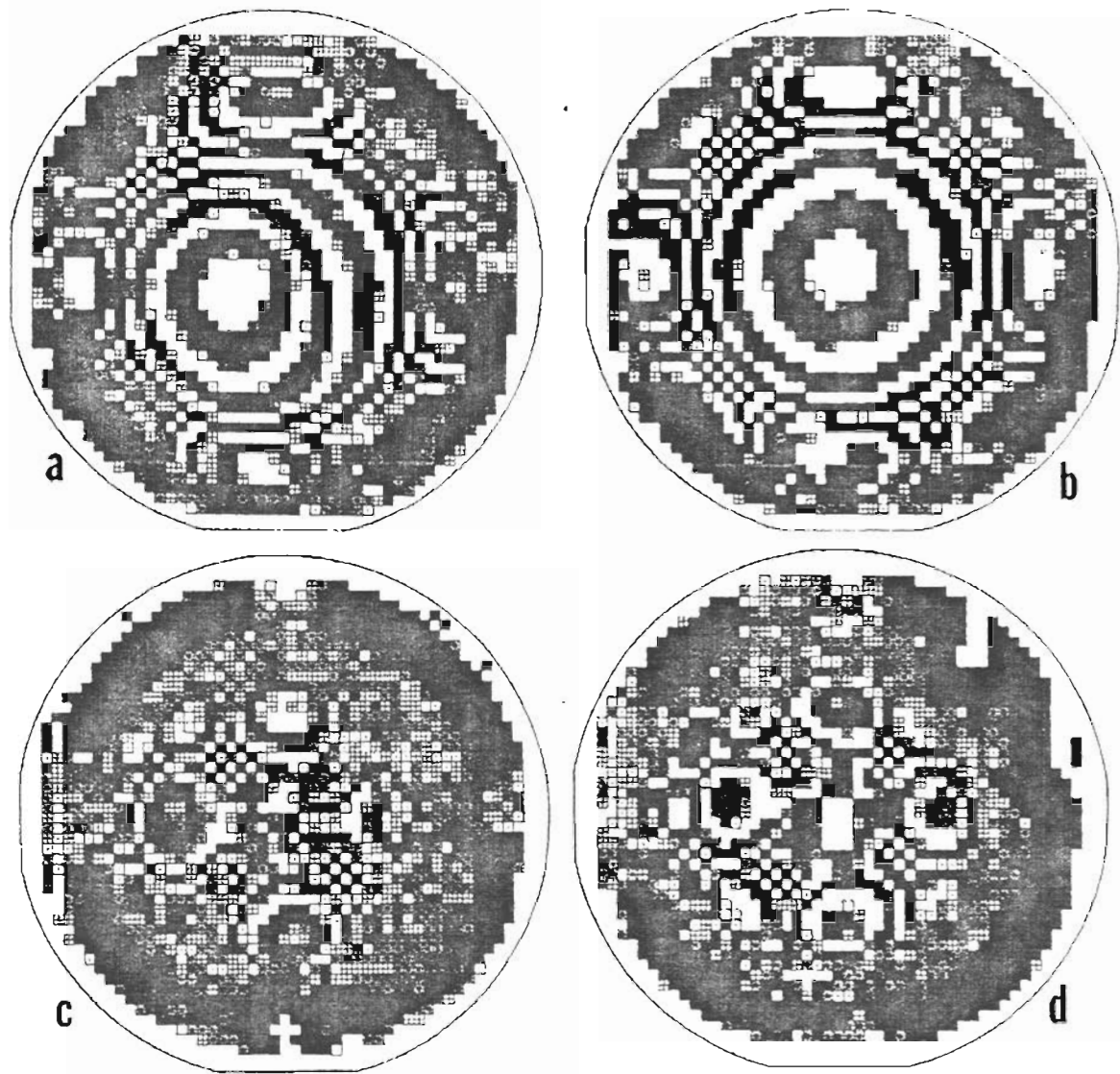


Figure 3-4: Stress contours in wafers from crystal 925. (a): wafer No. 10; (b): wafer No. 38; (c): wafer No. 71; (d): wafer No. 105.

exists. That connection is seen in the maps of Fig. 3-5, where the right one shows the dislocation distribution obtained etching the sample with the A/B etch. The map at left is the stress image of the same wafer. The coincidence between the two maps is more than good. In fact, while an exact correspondance between stress and dislocation maps is not to be expected, since dislocations have secondary sources (dislocations propagating from the seed crystal), and can moreover move through the crystal, it is reassuring to note that the minima in the $[011]$ direction in part (a) of Fig. 3-5 are characterized by a higher stress than the ones along $[0\bar{1}1]$ (the number of fringes is one unit higher along $[011]$), and this feature is recognized in the broader areas of low dislocations along $[0\bar{1}1]$ in the map of part (b).

The variability of the position of the minima of the stress field discussed above is seen in some other dislocation maps, as the ones in Fig. 3-6: part (a) shows the lowest dislocation density at some 52% of the radius of the wafer, as opposed to the minimum etch pit density at about 73% of the radius in the sample of part (b). Finally part (c) shows the sort of misalignment of the central peak

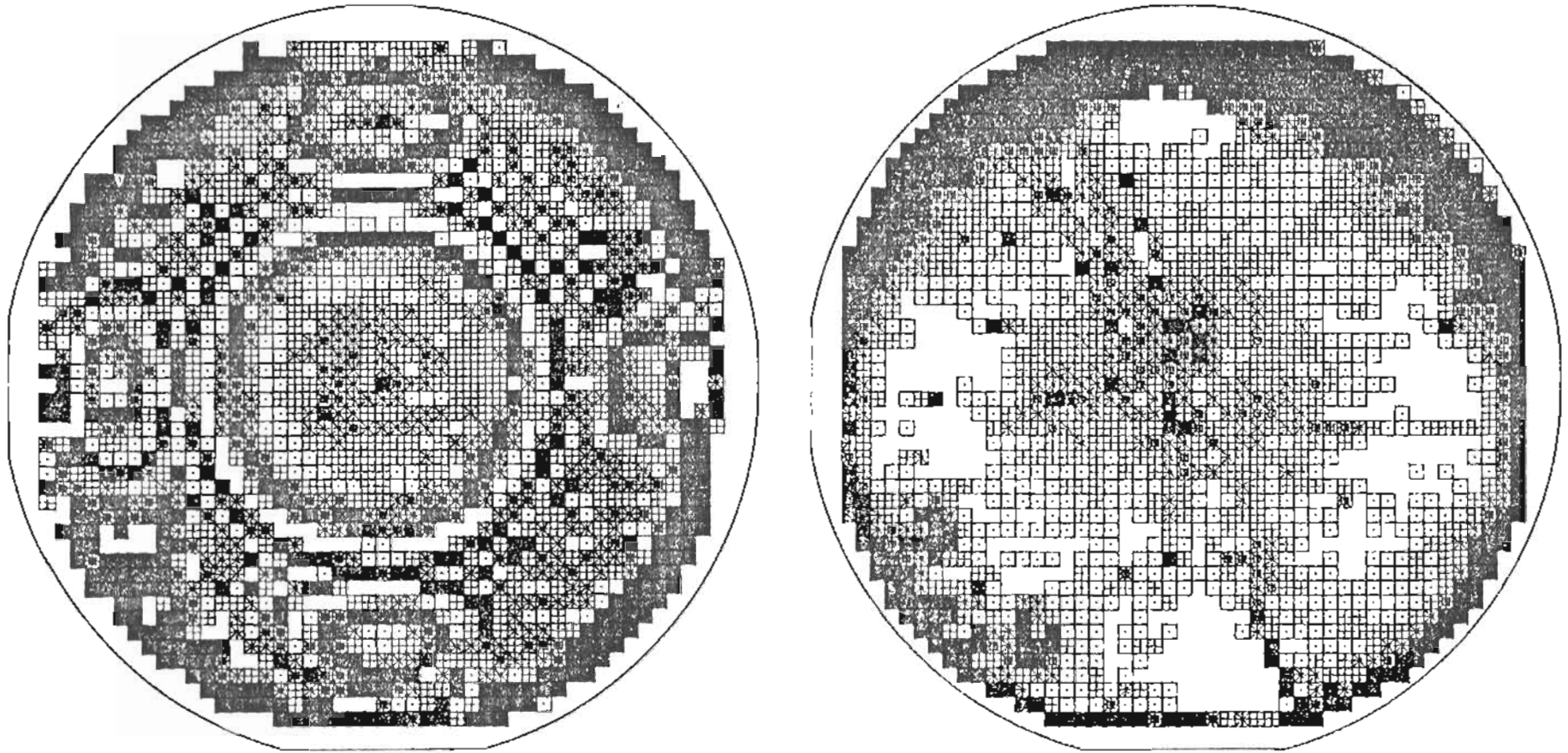


Figure 3-5: Correlation between stress contours and dislocation map in the same wafer.

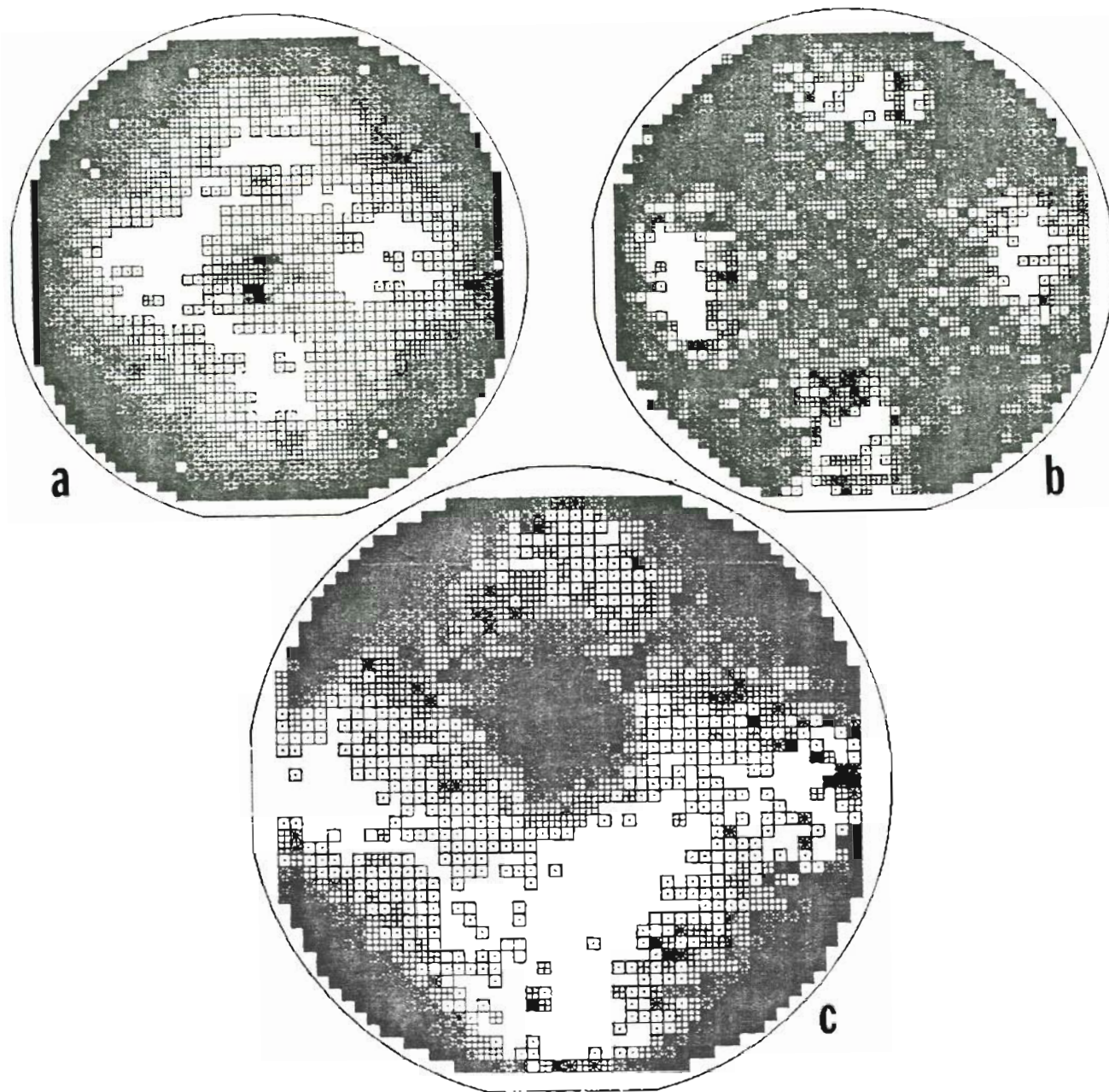


Figure 3-6: Dislocation maps of wafers from the same supplier. (a): 3" wafer, with minimum dislocation density at 52% of the radius, (A/B etch); (b): 2" wafer with minimum dislocation density at 73% of the sample radius, (KOH etch); (c): 3" wafer, with off-center maximum dislocation density, (A/B etch).

with respect to the center already seen in the stress map of wafer 925/10.

Despite the variability of the details of stress and/or dislocation patterns in all the previous samples, the basic fourfold symmetry is that theoretically expected. The intrinsic characteristics of the material seem to be able to compensate the gap between the ideal conditions postulated by theoretical treatments and the more complicated actual growth process.

A completely different situation is encountered in the analysis of LEC wafers from some other suppliers. First, consider Spectrum Technology. Figure 3-7 shows a typical stress map for a S. T. 2" wafer. Besides the general lack of details, contours of equal stress can be recognized as two or maybe three sets of circular fringes positioned near the center of the wafer and along the [001] direction.

A set of three maps for wafers from one S. T. ingot are shown in Fig. 3-8. In all these maps fringes are localized about two distinct areas of the wafer; such locations appear to be less dislocated than the surroundings, as shown in the dislocation map of Fig. 3-9.

The interpretation of these interferograms is

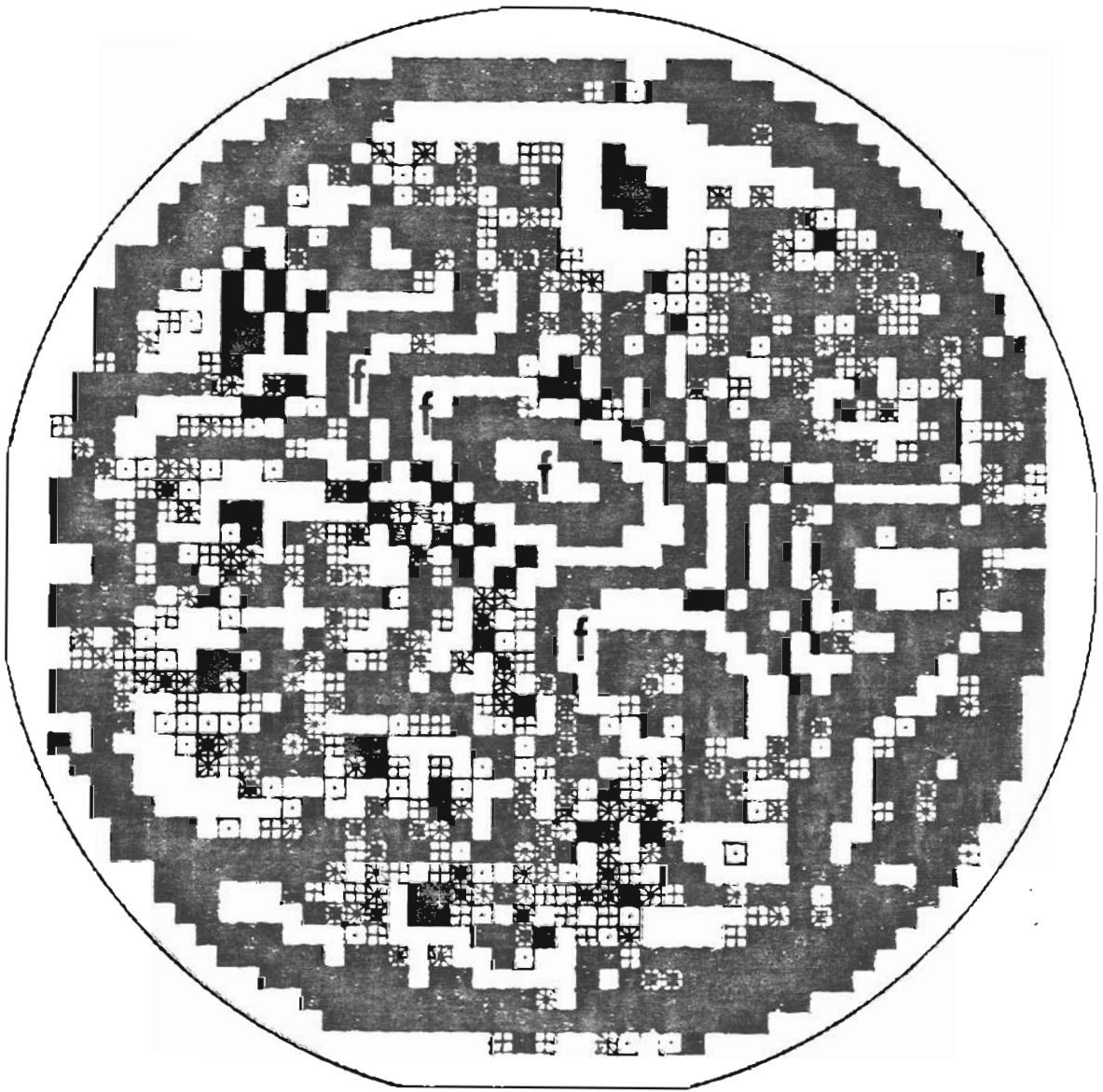


Figure 3-7: Stress contour map of a 2" wafer. Few fringes (f) can be resolved, oriented along a [100] direction. No four-fold symmetry is present.

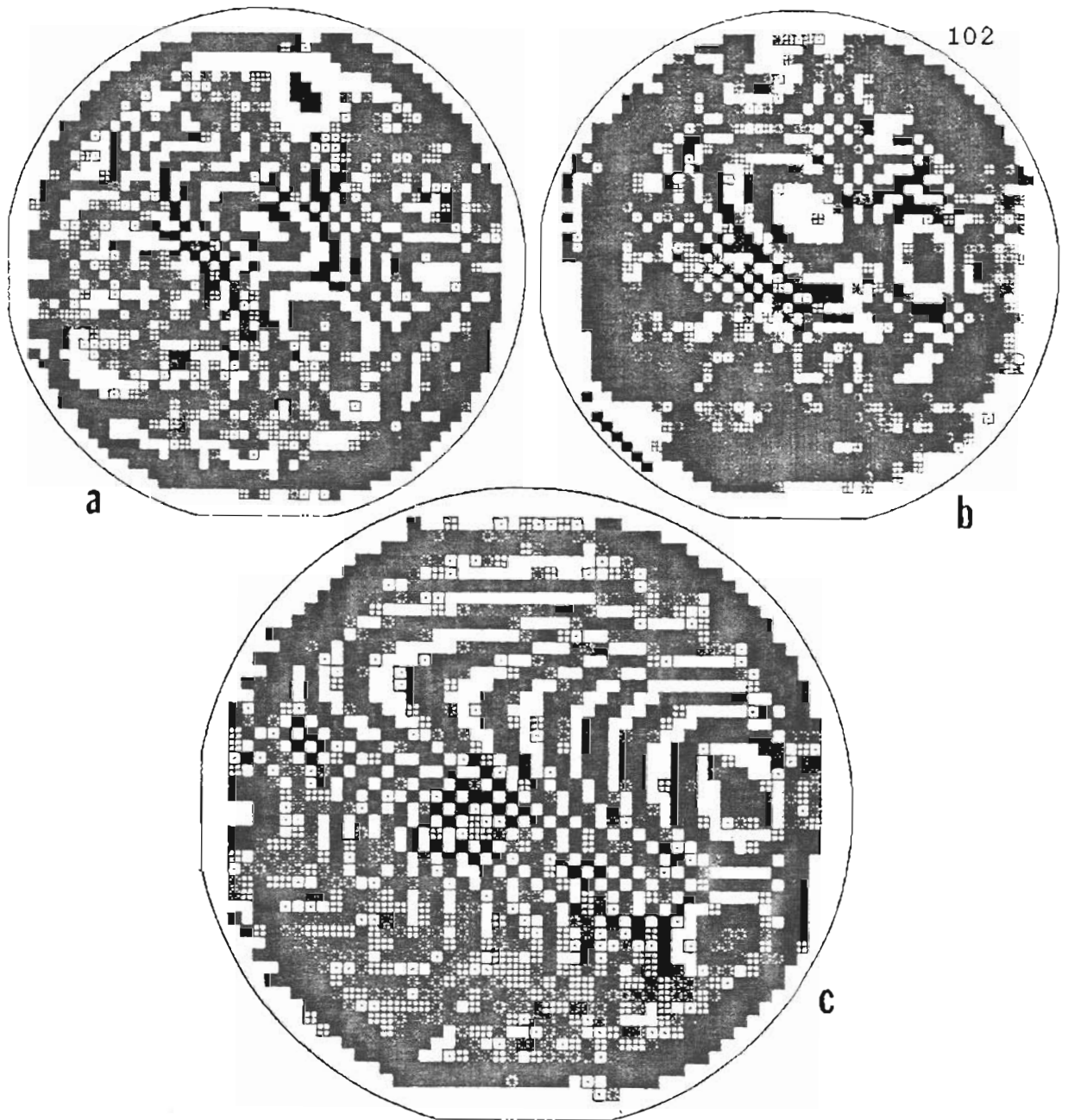


Figure 3-8: Stress contour maps of some wafers from the same 2" ingot. (a): wafer No. 120; (b): wafer No. 123; (c): wafer No. 100.

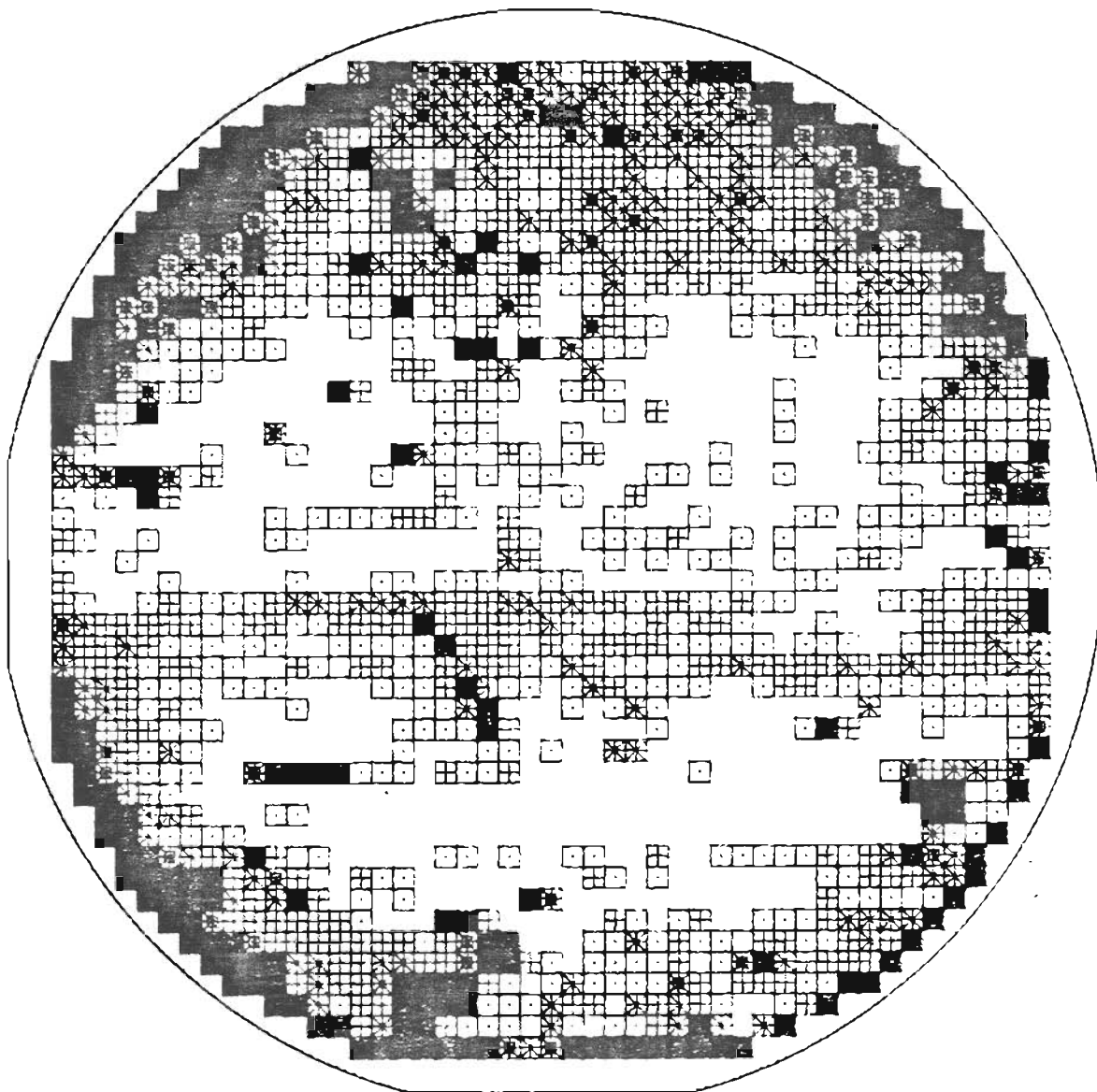


Figure 3-9: Dislocation map of wafer No. 100, whose stress map is shown in Fig. 3-8(c).

difficult, but it is evident that in these specimens the stress field is strongly modified from a "regular" Czochralski-induced pattern.

Passing to other manufacturers, new shapes are seen in contours of equal stress, as in Fig. 3-10 for wafers from a third source (Sumitomo). Figure 3-10 (a) shows the interferogram of an indium-doped wafer. Indium (In), an element isoelectronic to gallium, is used to dope an LEC ingot to a concentration of about 10^{20} cm^{-3} in order to harden the crystalline lattice. The hardening effect has been explained with a local distortion of the lattice [7] which also prevents the spreading of dislocations. The final effect is an increase of the threshold above which dislocations can be generated, and in fact the dislocation map in Fig. 3-10 (b) does show large dislocation free areas across the surface. Despite this addition of indium, the sample of Fig. 3-11 shows a distorted stress symmetry with a central peak.

All the samples from the manufacturer (Sumitomo) of the wafer mapped in Fig 3-10 show indefinite stress patterns, independently from the addition of indium. This is the case shown in Fig. 3-12, made up by the stress (a) and

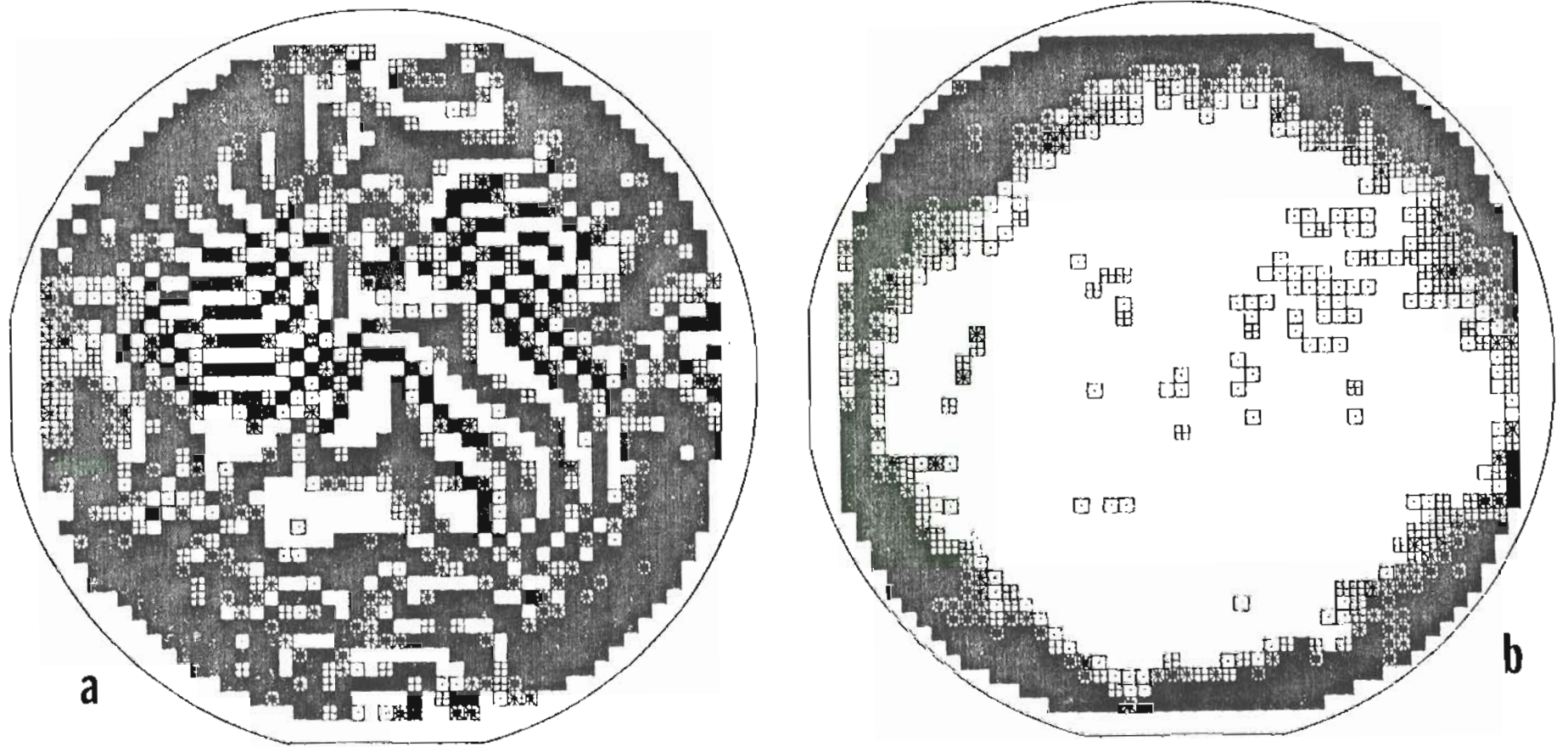


Figure 3-10: Stress (left) and dislocation (right) maps of an In-doped, 3" wafer. White areas in the dislocation map correspond to essentially dislocation free zones.

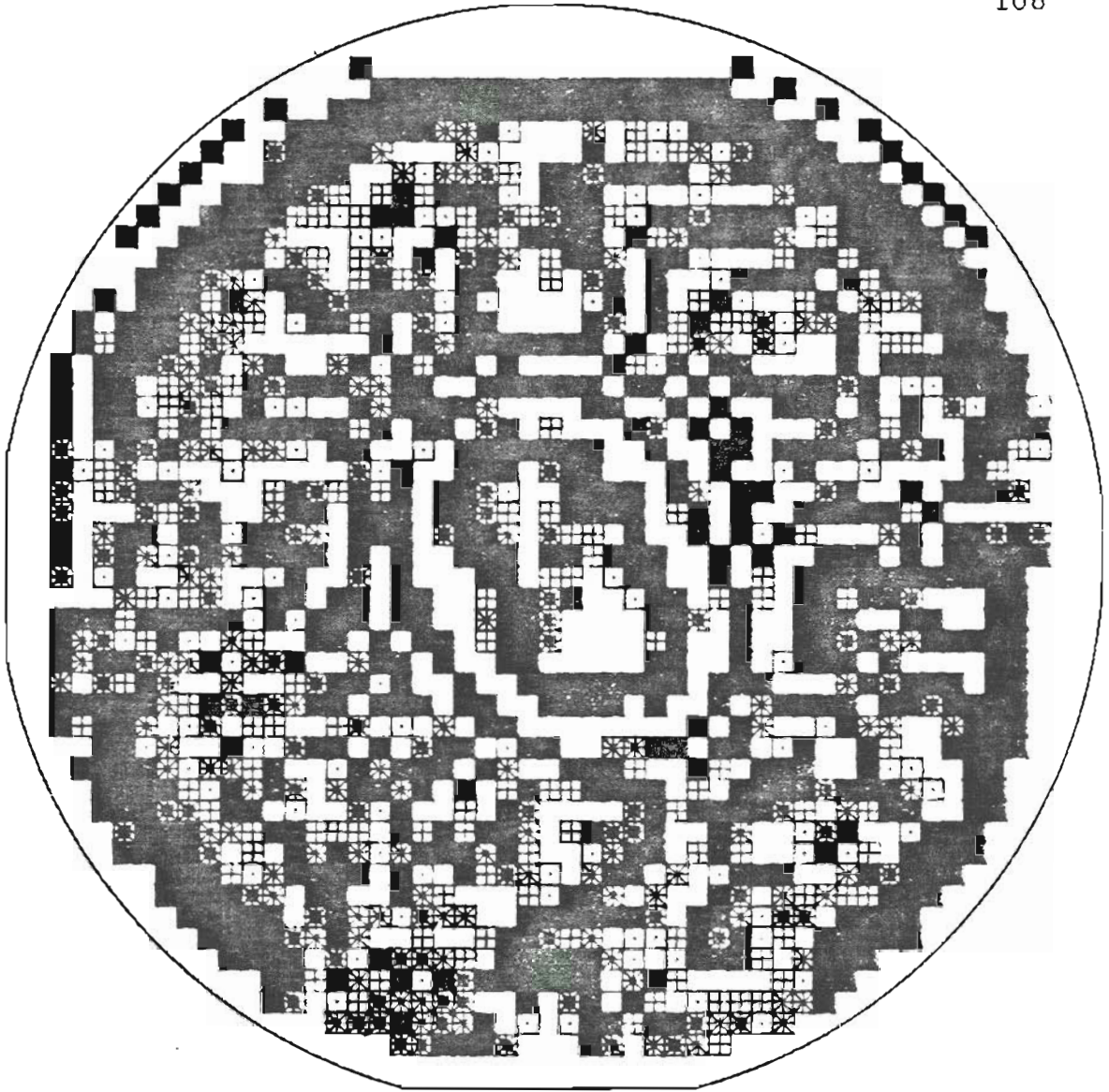


Figure 3-11: Stress map of another In-doped sample. Few fringes can be resolved at the center of the wafer.

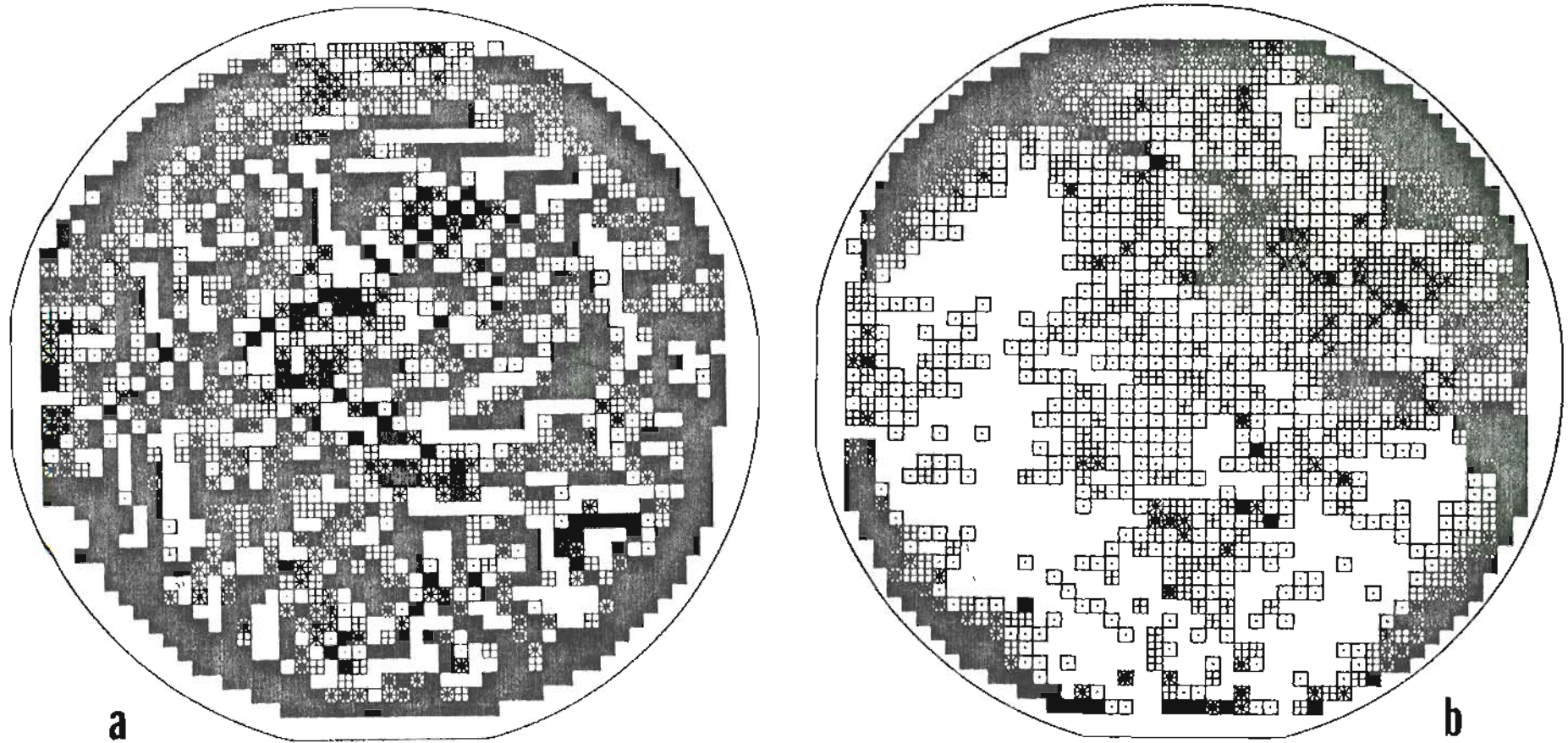


Figure 3-12: Stress (a) and dislocation (b) maps of an undoped GaAs wafer, from the same supplier of the sample of Fig. 3-10.

dislocation map (b) of an undoped sample; it can be seen that even in the absence of In-doping, the dislocations are distributed with absolute disregard of the crystallographic directions.

Some conclusions can be drawn from these results, the main one being that nominally identical growth processes produce quite different stress distributions in GaAs crystals. In connection with this, one must recognize that theoretical treatments [4-6] of the Czochralski technique are not always applicable. Nevertheless, in some cases the experimental stress patterns are similar to the theoretical ones, even if the stationary character of the theoretical solution is not adequate to provide a full account of the axial distribution of the stress field.

The possibility of mapping the frozen-in stress distribution independently from the dislocation pattern appears to be quite an important result, providing an experimental basis any future theoretical analysis will have to deal with. Such nondestructive stress mapping is timely, in view of the fact that the dislocation distribution does not appear to reproduce with fidelity the original stress distribution, because of other unknown mechanisms [5].

C. EL2 distribution

Radial profiles of the EL2 distribution were first studied by Holmes et al. [1]. They reported that EL2 profiles across the front of SI crystals grown from As-rich or near-stoichiometric melts were invariably W shaped. Profiles from the tail end of ingots were often U shaped, or inverted U shaped, as well as W shaped. In the same crystals, the dislocation distribution remained W shaped from seed to tail. They concluded that these EL2 profiles could be caused by residual stress, and/or by variations in melt composition at the solid-liquid interface during growth.

In a following report [2] the same authors provided 2-dimensional plots of the EL2 distribution, of the kind shown in Fig. 3-13, and confirmed the occurrence of four-fold symmetry in wafers cut from the front end of LEC ingots. Despite the lack of such symmetry in samples from tail portions in which the dislocation distribution was consistently crystallographically dependent, they explained these results with the hypothesis of stress enhanced EL2 formation.

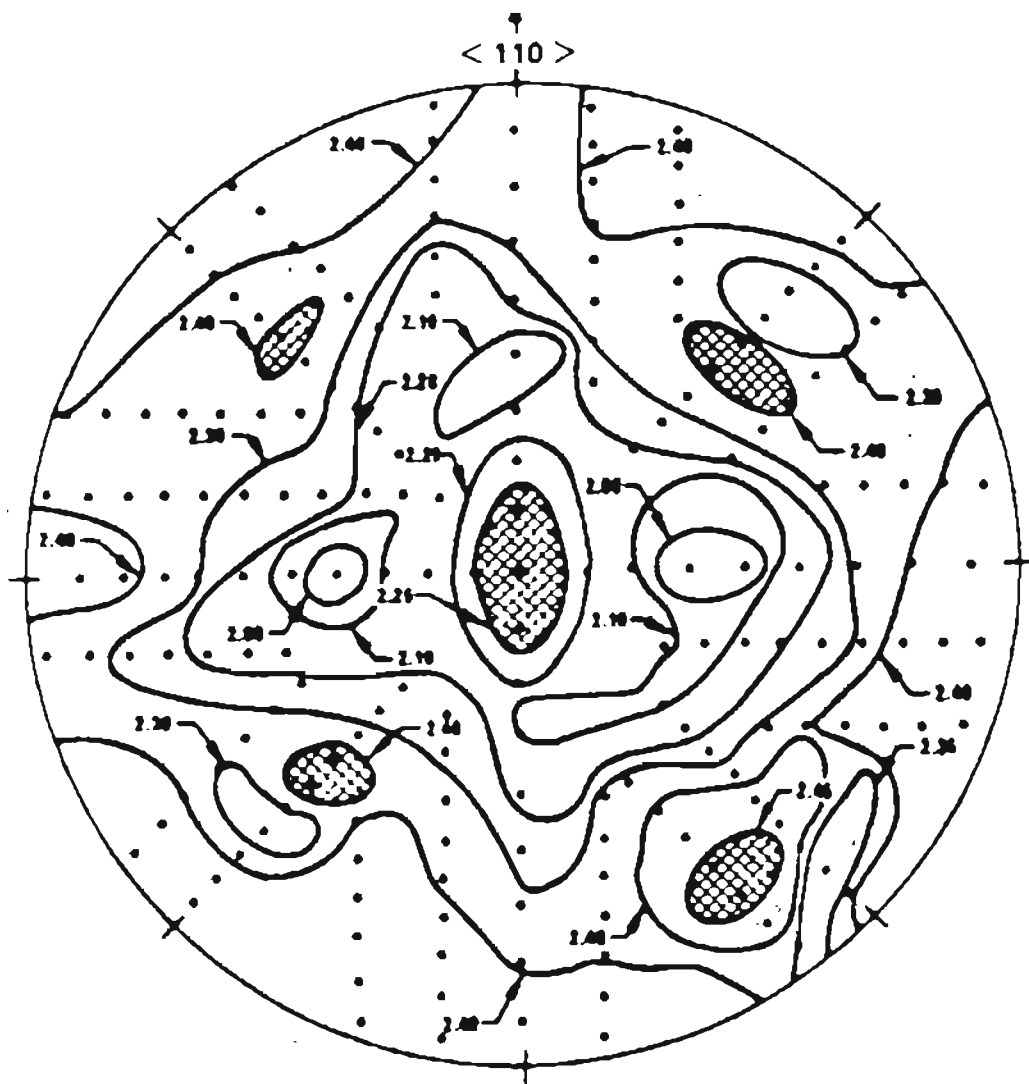


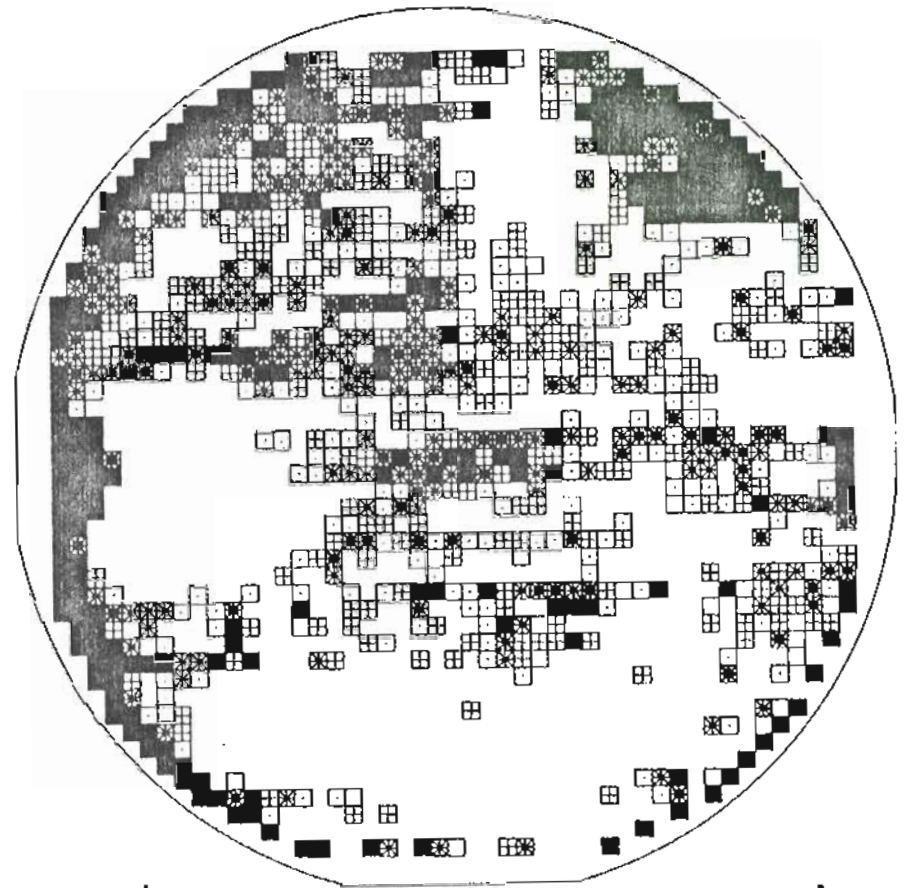
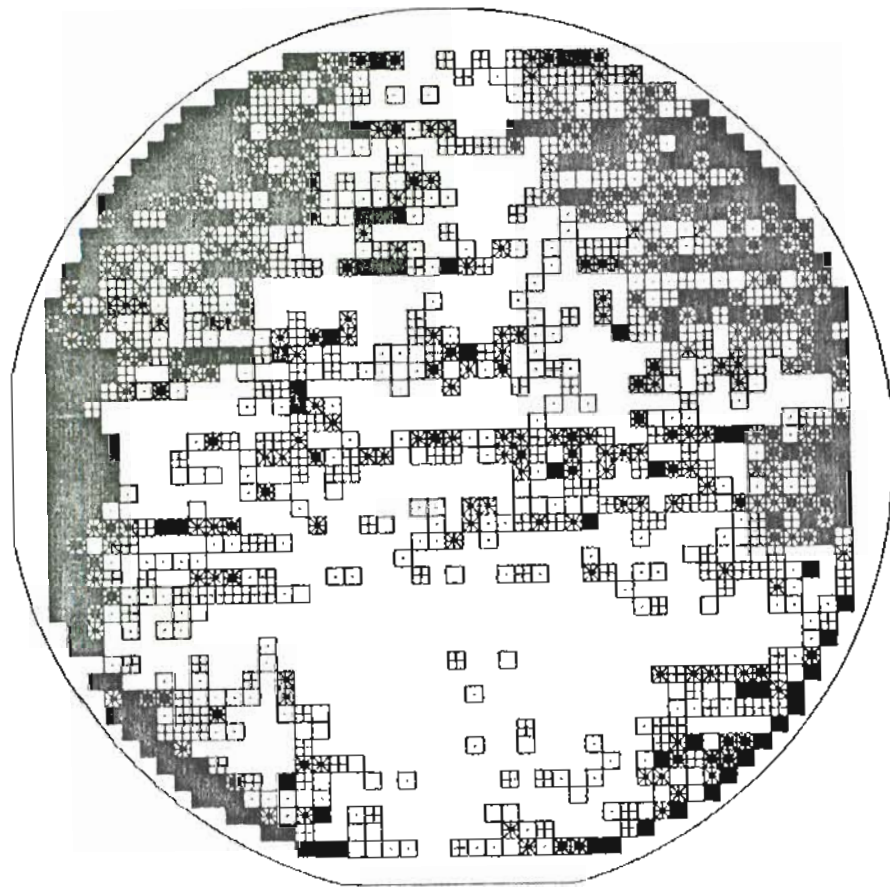
Figure 3-13: EL2 distribution in a 3 mm thick wafer, as detected and displayed by Holmes *et al.* [1].

The situation at present is still far from being clear, because of the almost simultaneous publication of some "definitive" proofs of a 1 to 1 correlation between dislocations and EL2 centers [3] and well documented but less flamboyant evidence of no correlation between EL2 formation and dislocation climb [8].

The main questions to be asked as far as the EL2 distribution is concerned are: (1) what controls the average EL2 concentration, and how does this parameter change along the growth axis of an ingot ?; (2) what controls, or influences the EL2 distribution in the (100) plane, orthogonal to the [100] growth axis ?

The present study could not determine the factors that influence N_{EL2} averaged over the entire ingot, due to the proprietary sparsity of information about the growth conditions of our samples. On the other hand, the dependency of EL2 on the melt composition seems to be reasonably well established, and is represented in Fig. 3-14, reproduced from Ref. 9.

The seed-to-tail trend of the EL2 concentration does not seem to follow a sharp pattern. For instance the two samples of Fig. 3-15 are characterized by an average EL2



a

b

6 LEVEL SCALE. STEP =.02 cm⁻¹

□ ABS. COEFF. <1.61 EL2 <13.41 E15 cm⁻³
 ■ ABS. COEFF. >1.69 EL2 >14.08 E15 cm⁻³

6 LEVEL SCALE. STEP =.02 cm⁻¹

□ ABS. COEFF. <1.80 EL2 <13.83 E15 cm⁻³
 ■ ABS. COEFF. >1.74 EL2 >14.48 E15 cm⁻³

Figure 3-15: EL2 maps, from seed (a) and tail (b) wafers in the same ingot.

concentration constant within 3%. Part (a) of the figure shows the EL2 distribution in wafer No. 28, averaging $1.38 \times 10^{18} \text{ cm}^{-2}$, while in wafer No. 98, in part (b) of the same figure $N_{EL2} = 1.41 \times 10^{18}$. Neither wafer, by the way, shows a recognizable EL2 pattern.

Although we could report measurements of many pairs of seed/tail wafers, we prefer to discuss the problems related with such coupled measurements, on the basis of our analysis of crystal No. 638, for which 8 wafers cut at different positions along the length of the ingot were measured.

This long crystal was grown to a radius of about 30 mm and then cut into some 220 wafers 50 mm in diameter. The actual crystal profile, as provided by the grower of the ingot [10], is shown in Fig. 3-16, since it will be useful later on. The same figure shows the average EL2 concentration in the wafers we analyzed, and the point is that if one were to characterize this ingot on a seed-to-tail trend basis, wafers Nos. 5 or 38 from the seed and Nos. 190 or 215 from the tail would be a priori logical choices.

Depending on the pair of samples actually chosen, though, quite different results would be obtained: an

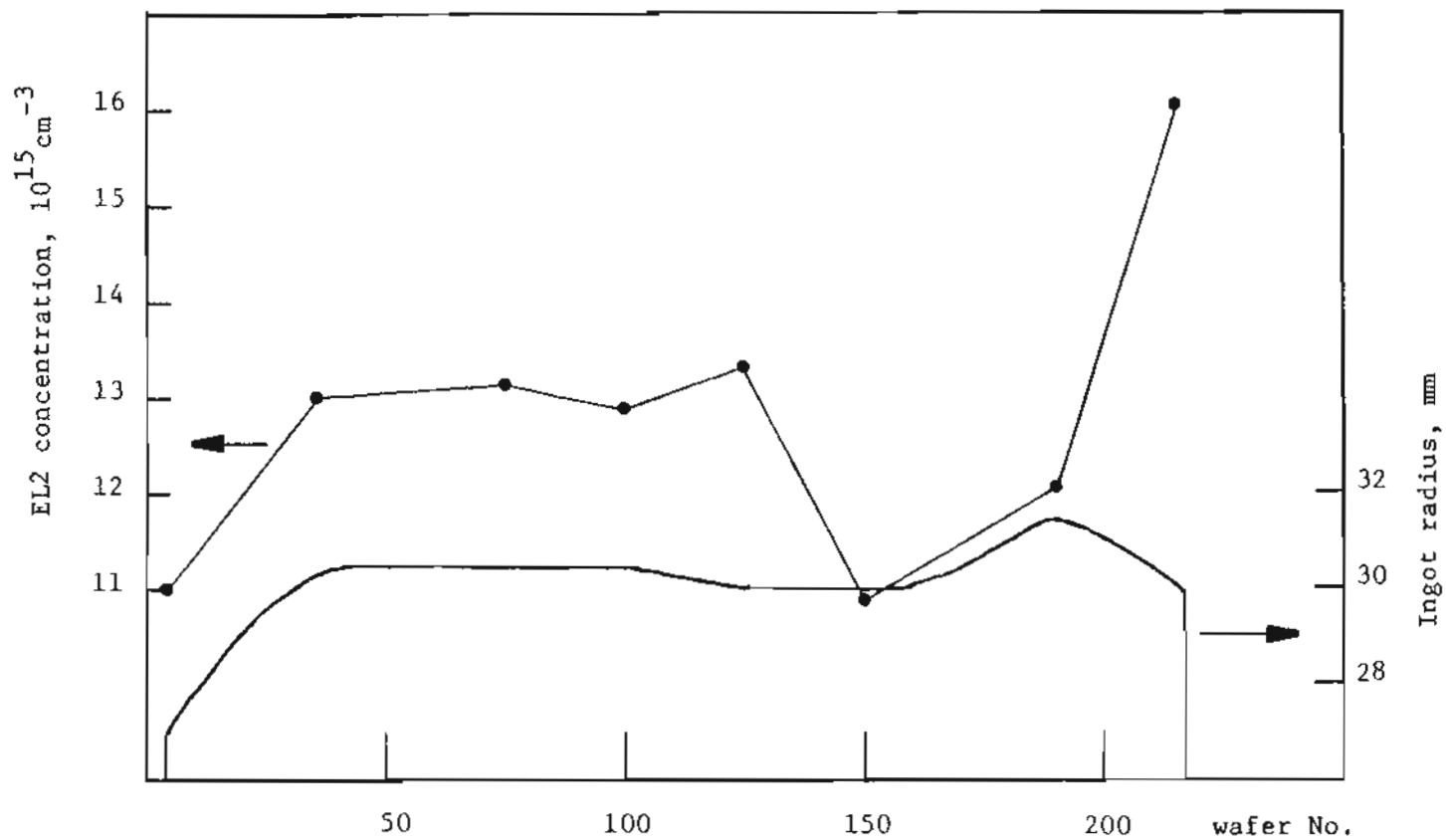


Figure 3-16: Ingot profile (lower curve) and EL2 concentration (upper curve) in crystal 638, from which 8 wafers were analyzed for EL2 and stress patterns.

essentially uniform axial distribution would be inferred on the basis of the pair 5-190, a lower EL2 concentration towards the tail with the pair 38-190, or a moderately larger EL2 at the tail (pair 5-190), as well as a huge increase from seed to tail could be deduced measuring the pair 5-215. The fact is that this ingot (like probably many others) is not suited to be characterized in terms of seed-to-tail trend, having a near-constant EL2 concentration through a large central portion, and large variations towards the tail end.

The spatial distribution of EL2 in representative wafers from crystal 638 can be seen in Fig. 3-17. Parts (a) and (b) show a four-fold symmetrical distribution, which becomes less clear in part (c), the map of wafer No. 190. At the level of wafer No. 215 (part (d)) the EL2 distribution has radial symmetry, of the kind usually described as inverted U [1]. The wafers whose maps are not shown were not distinguishable from wafer No. 72, part (b) of the figure.

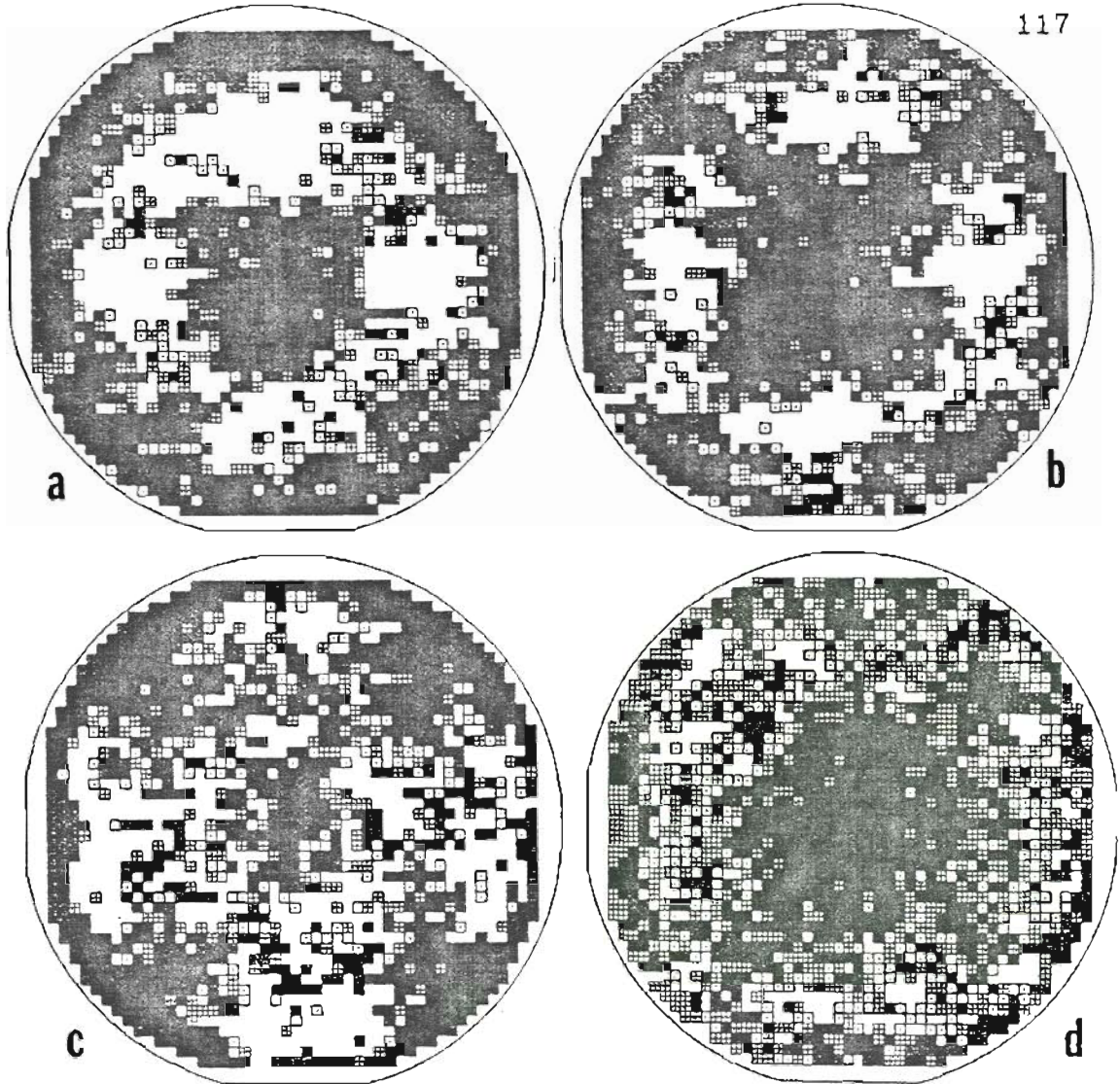
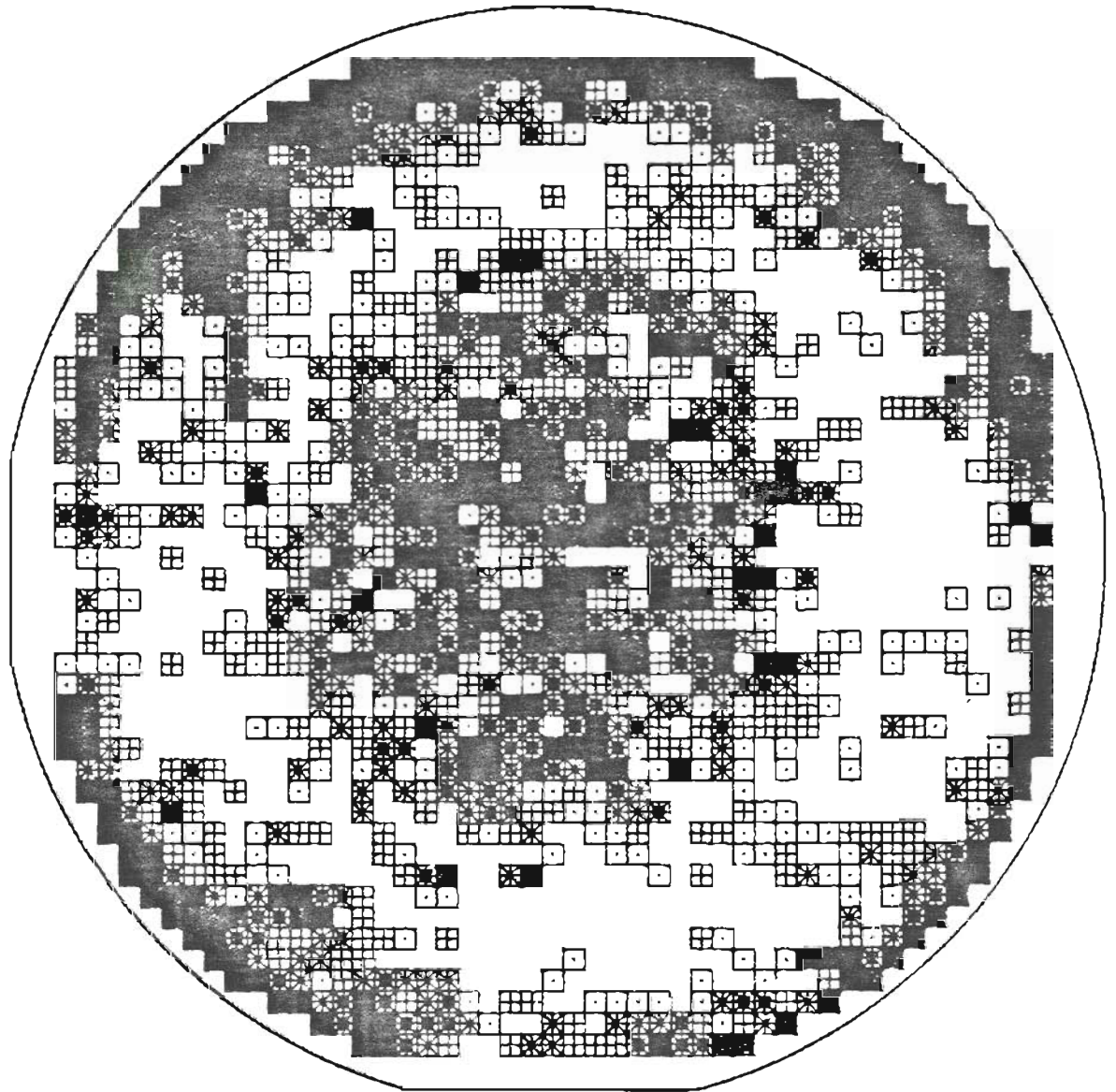


Figure 3-17: EL2 maps of wafers from crystal 639. (a): wafer No. 5; (b): wafer No. 72; (c): wafer No. 190; (d): wafer No. 215.

Shapes like the one of part (b) of Fig. 3-17 motivated the hypothesis that EL2 and dislocations (or stress) are somehow coupled. Even for this "canonical" wafer, anyway, a problem arises with this hypothesis. The minimum EL2 concentration is found at $r = 15$ mm, which is 60% of the radius of the sample. Stress maps of this and other wafers from this ingot show the same kind of symmetry, but the local stress minima are at about 90% of the radius (see Fig. 3-3 for stress maps of these wafers). The profile of the as-grown ingot (Fig. 3-17) allows us to determine that the stress minima are localized at some 70% of the original radius, in overall agreement with calculated positions of minimum stress [4-6]. In terms of as-grown radius, which is after all the important parameter, EL2 minima are at 50% of this distance, much closer then to the center than the theoretically expected and experimentally determined value of low stress intensity.

Despite the symmetry of the stress contours in the last wafer from this ingot, (Fig. 3-3(d)), the EL2 pattern in this wafer is radial, decreasing towards the periphery and with no azimuthal dependence. Such EL2 distributions are not uncommon, another example being seen in Fig. 3-18. Generally

WAFER PUN2302Y125/11
 DIAMETER : 78 mm
 THICKNESS : .7 mm
 WAVELENGTH : 1000 nm
 MEAN ABS.COEFF. : 1.031 cm⁻¹
 MEAN EL2 : 8.58 E15 CM⁻³
 AVERAGE TRANSMISSION : .483



8 LEVEL SCALE, STEP = .03 cm⁻¹

□ ABS.COEFF. < .972 cm⁻¹ EL2 < 8.09E15 cm⁻³
 ■ ABS.COEFF. > 1.092 cm⁻¹ EL2 > 8.09E15 cm⁻³

Figure 3-18: Radial EL2 distribution in a 3" wafer.

these shapes are found in wafers cut from the ingot tail end.

As opposed to the four-fold distribution, these radial patterns can be explained by the thermal history of the crystal tail end after growth. An example of a typical cooling cycle can be seen in Fig. 3-19, reproduced from the work of Holmes et al. [11].

In general the last portion to solidify will experience a faster cooling than parts of the ingot that emerge from the encapsulant earlier, since the latter will begin cooling naturally while the rest of the growth takes place. Only after the entire crystal has emerged is a "programmed" cooling sequence begun. As a result, the tail EL2 concentration, which is expected on thermodynamical grounds to increase with temperature, does not have time to continuously adjust to the rapidly falling temperature, and its room temperature distribution reflects the radial profile of the temperature, in a sort of frozen-in state. This hypothesis is substantiated by the fact that the tail EL2 concentration decreases upon annealing [11], as opposed to the increase of the seed EL2 concentration in the same circumstances.

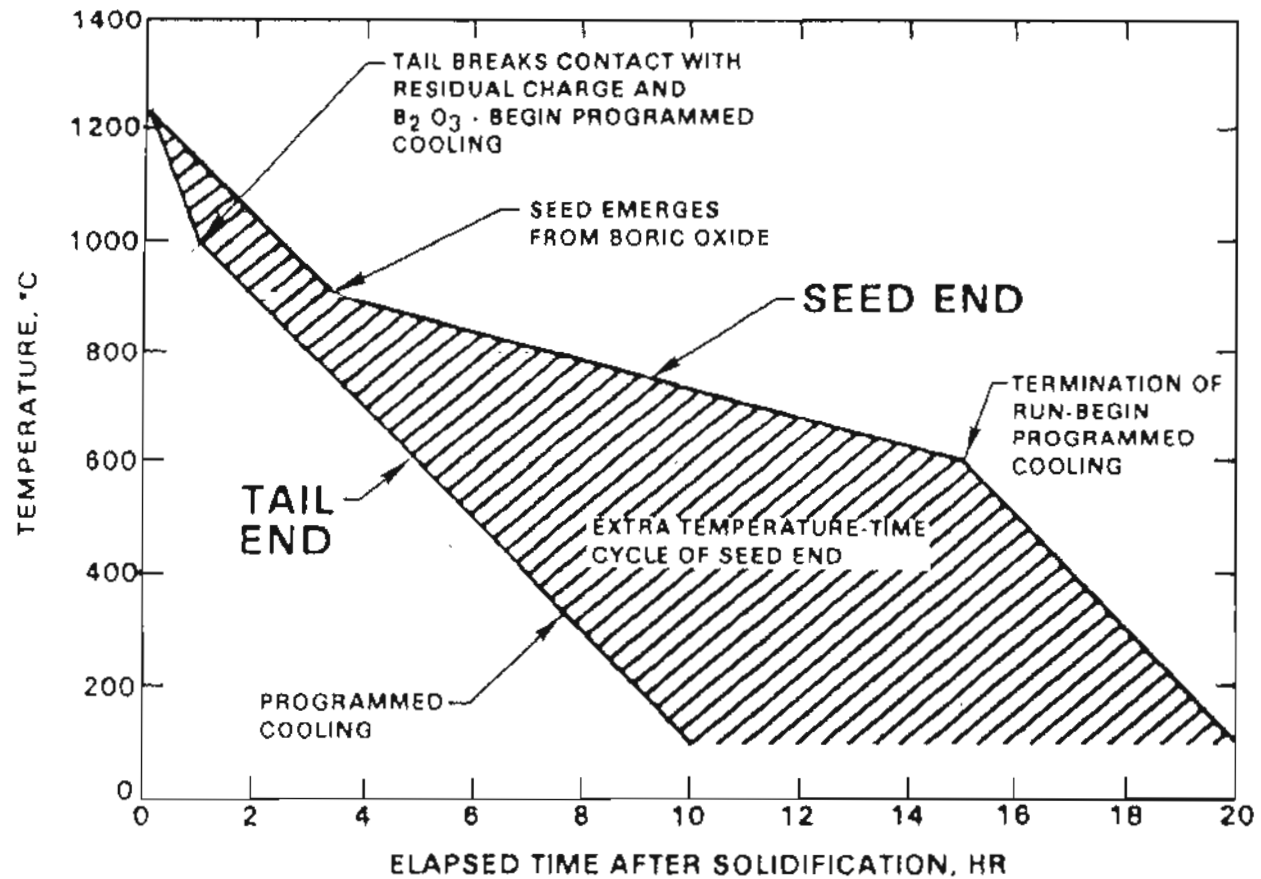


Figure 3-19: Cooling cycle of a LEC ingot, after Ref. 11 . The tail end cools to room temperature in ca. ten hours, about half of the time required for the seed end to reach the same temperature.

Before concerning ourselves with the large-scale EL2 distribution in (100) cut wafers, some details of that distribution can be understood. With reference to the two maps in Fig. 3-20, the features we are interested in are the lines of high EL2, labelled "L" in the maps and parallel to the [110] directions.

These EL2 accumulations are associated with similar "lineages" of dislocations, of the type shown in the micrograph of Fig. 3-21. Such slip lines, always parallel to [011] or [01 $\bar{1}$], are much more numerous than corresponding EL2 lines in the maps, this being due to the limited spatial resolution of our mapping system. Nevertheless, EL2 is clearly concentrated around these dislocations, so that a gettering about extended defects is extremely likely to be the process responsible for these EL2 nonuniformities. A further example of EL2 gettering about linear arrays of dislocations is evidenced in Fig. 3-22. It is noteworthy that these three wafers were produced by different suppliers, so that this gettering mechanism appears to be universally present.

We are ready to attach physical meaning to claims of a 1 to 1 correlation between dislocations and EL2 centers

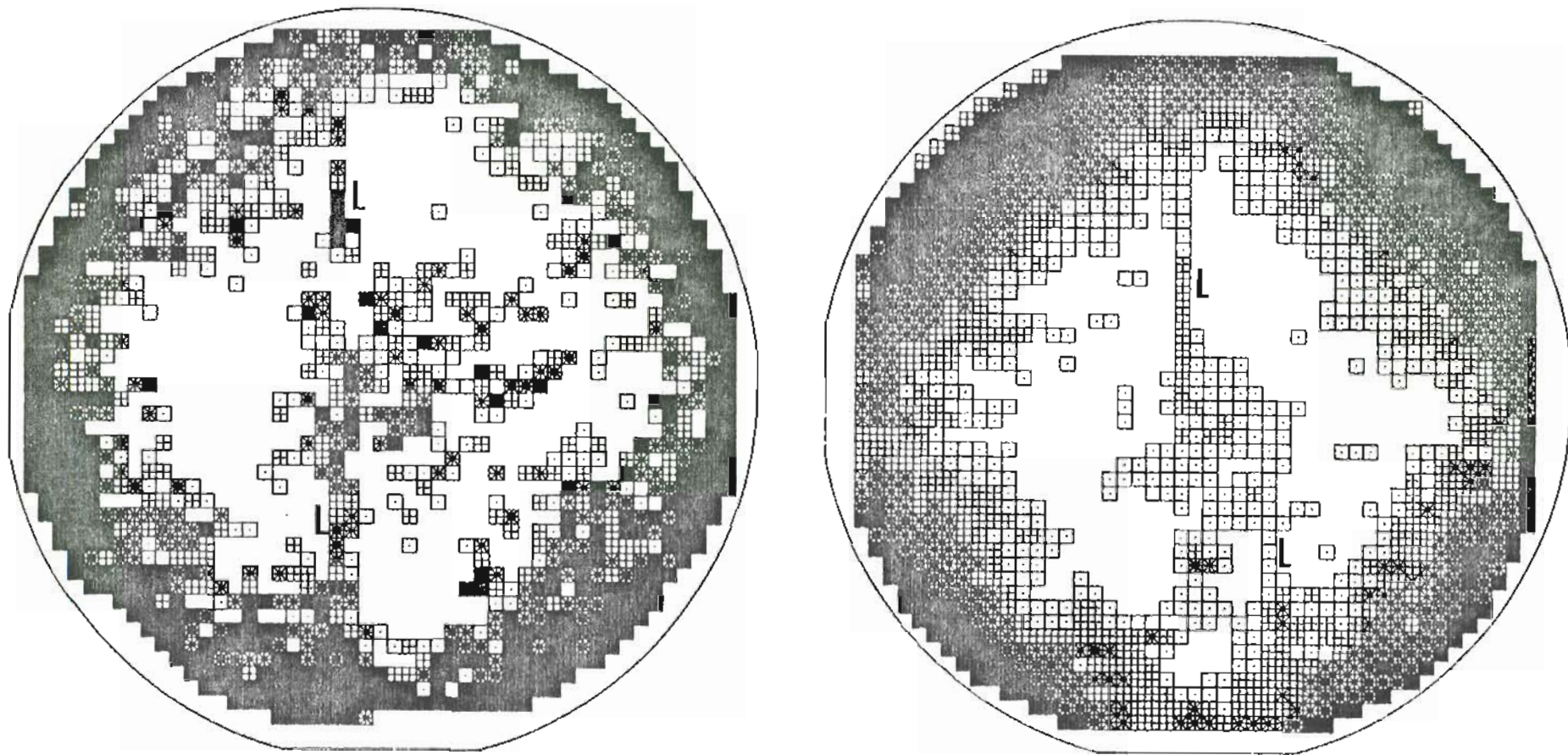


Figure 3-20: EL2 accumulation (features labelled "L" in the maps) near dislocation lineages.

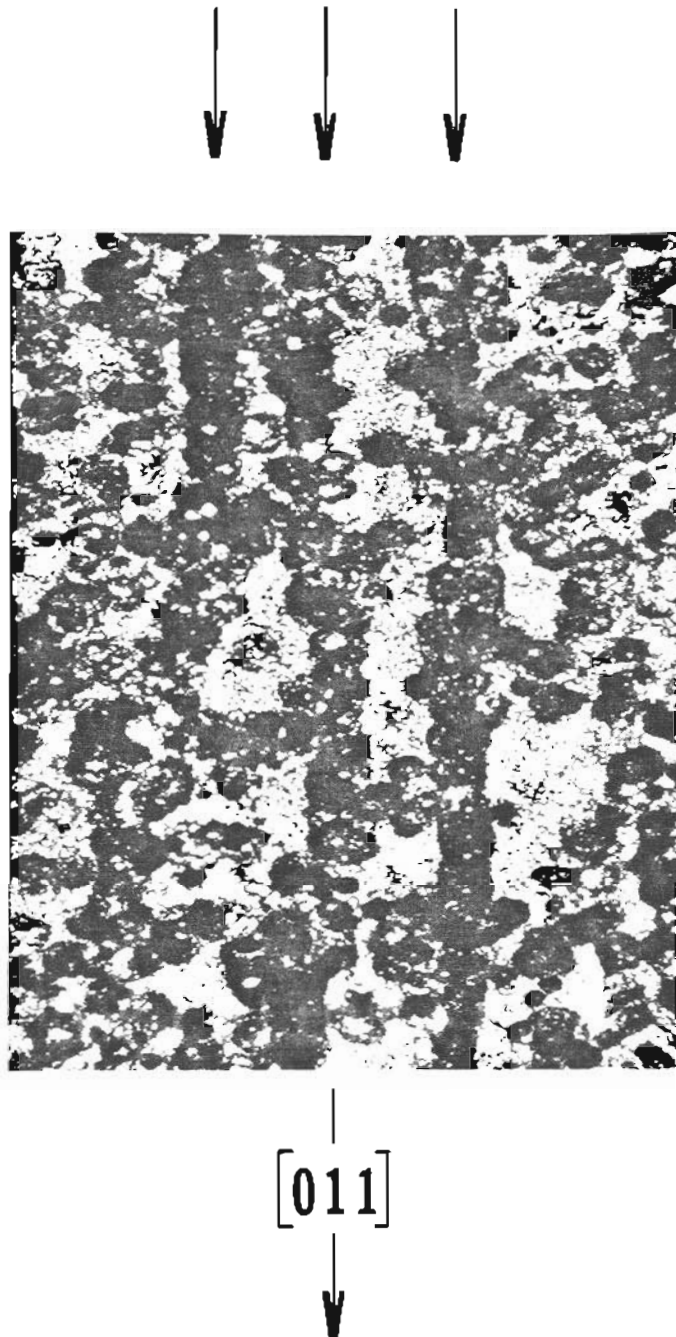


Figure 3-21: Micrograph ($M = 400\times$) of dislocations grouped in lineages in a KOH etched wafer.

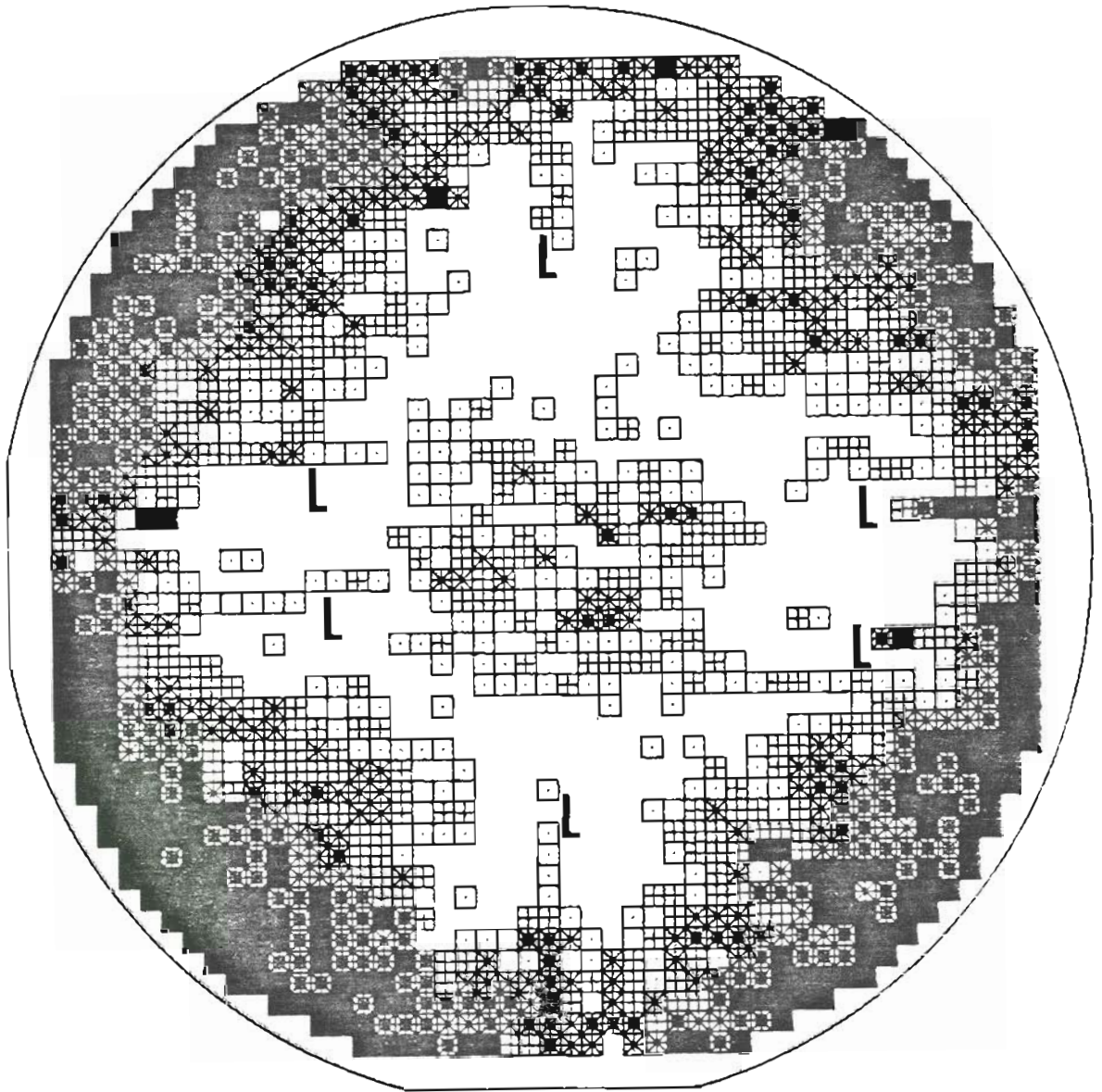


Figure 3-22: EL2 map, evidencing gettering about lineage dislocations (L).

[3,12] when experimental evidence is taken from this kind of locations in a LEC wafer; in most cases, nevertheless, we feel such correlations have no real physical meaning, for the simple reason that in a cubic centimeter of GaAs, containing some 10^{16} EL2 centers and traversed by 10,000 dislocations, the spatial coincidence of etch pits and EL2 related high IR absorption is statistically very high. We should indeed be very surprised by the lack of such coincidences! Furthermore, the etch pits shown in the works of Ref. [3,12] seem to indicate dislocations always perpendicular to the (001) plane, while in all our samples the great majority of dislocations lay parallel to this plane.

As far as the overall shape of the EL2 distribution is concerned, it is true that about 50% of the samples have a symmetrically distributed EL2 concentration. It is also true that some 50% of the dislocation maps show the four-fold symmetry. Unfortunately, the two sets of samples do not necessarily coincide. While samples in which the EL2 distribution is less symmetrical than the dislocation pattern do not disprove that the EL2 pattern is controlled by dislocations (for it is very likely that other unknown

factors may disrupt the dislocation-related EL2 symmetry) we have seen a number of wafers where EL2 is symmetrically distributed in absence of, or despite, different dislocation and stress patterns.

To begin, figure 3-23 (a) shows the stress contour map of a 3" wafer from the tail end of an ingot. The symmetry evidenced is the regular four-fold one, with minima in the [011] directions. Part (b) of the same figure represents the EL2 map of the same wafer. Clearly, there is a symmetrical distribution of EL2, but minima of N_{EL2} are positioned along the [001] directions, 45° from the stress minima. I measured another sample, from the seed end of the same ingot (whose dislocation map can be seen as Fig. 3-6 (c)), which evidenced the same EL2 distribution as in the sample plotted here.

The same lack of correlation is evidenced in the matched maps of Fig. 3-24, while an almost reversed spatial correlation can be observed in the maps of Fig. 3-25. Areas of low dislocation density marked "ld" in the map at left are zones of high N_{EL2} in the EL2 map at right, the opposite being true for areas of high dislocation density (hd).

Concerning the relationship between EL2 and

dislocations, dislocation free (In-doped) samples offer interesting opportunities to test the validity of the linkage of EL2 formation to extended defects. Very little information is available on the EL2 distribution in In-doped samples, the most interesting work being by Duseaux et al. [13]. They measured the optical absorption of 4 mm thick samples and deduced that the average EL2 concentration is much lower than in undoped samples, and that no sign of a four-fold symmetry could be detected. They concluded that the EL2 concentration in In-doped material arises as a background concentration due to thermodynamic equilibrium.

Figures 3-26, 27, 28 show the results of our investigations on In-doped wafers, and two observations are immediate: the average EL2 concentration is 2-3 times lower than in undoped material, but the qualitative features are not different from undoped samples. If we are to consider the measured concentration as the EL2 thermodynamic background concentration, we must conclude that the effect of dislocations in undoped material increases the thermodynamic concentration by two or three times. Such a hypothesis does not appear reasonable by itself, since we should think that any mechanism able to modify the

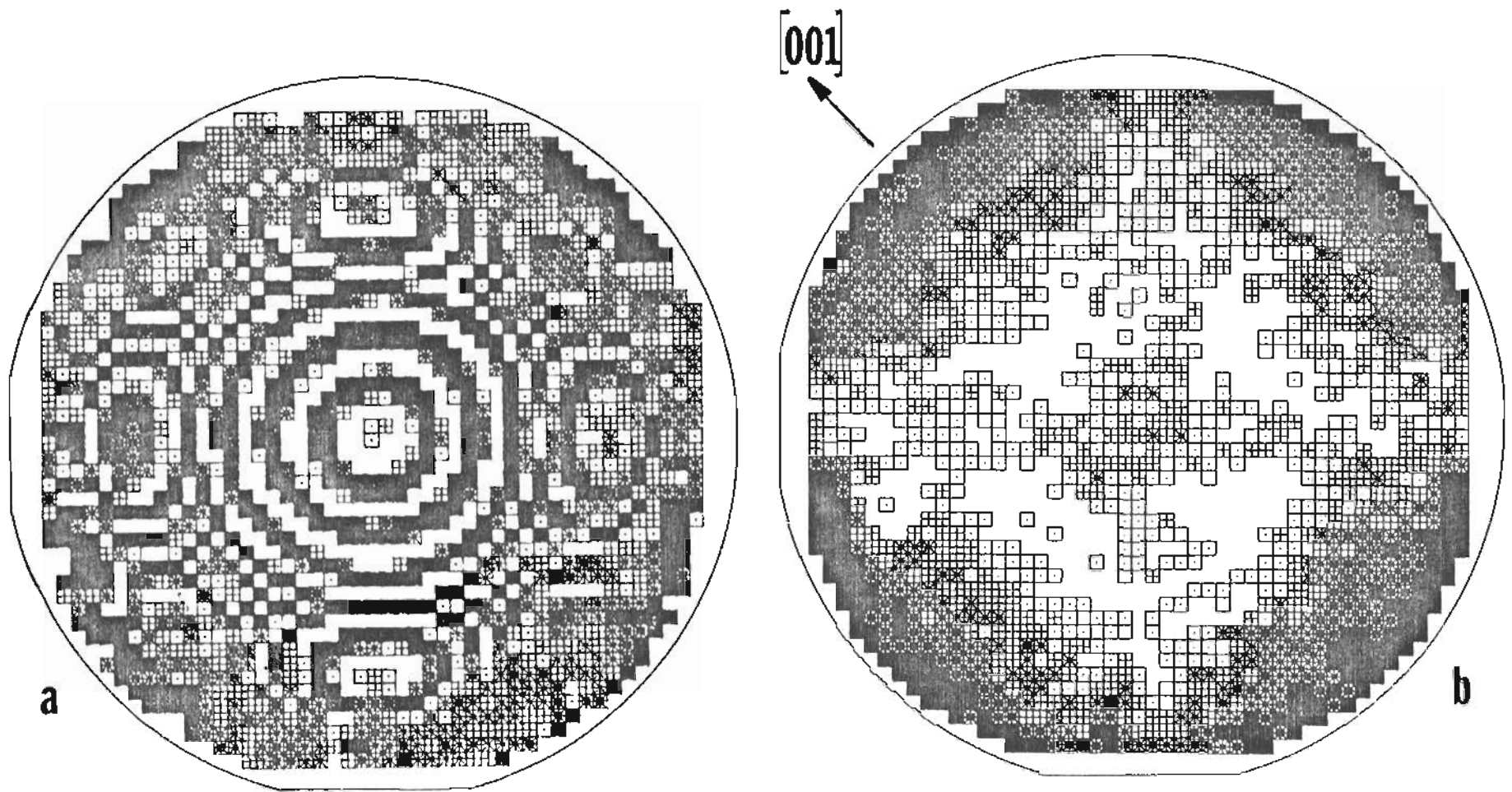


Figure 3-23: Stress (a) and EL2 (b) maps of the same wafer. Local EL2 minima are positioned along the $[001]$ class of directions.

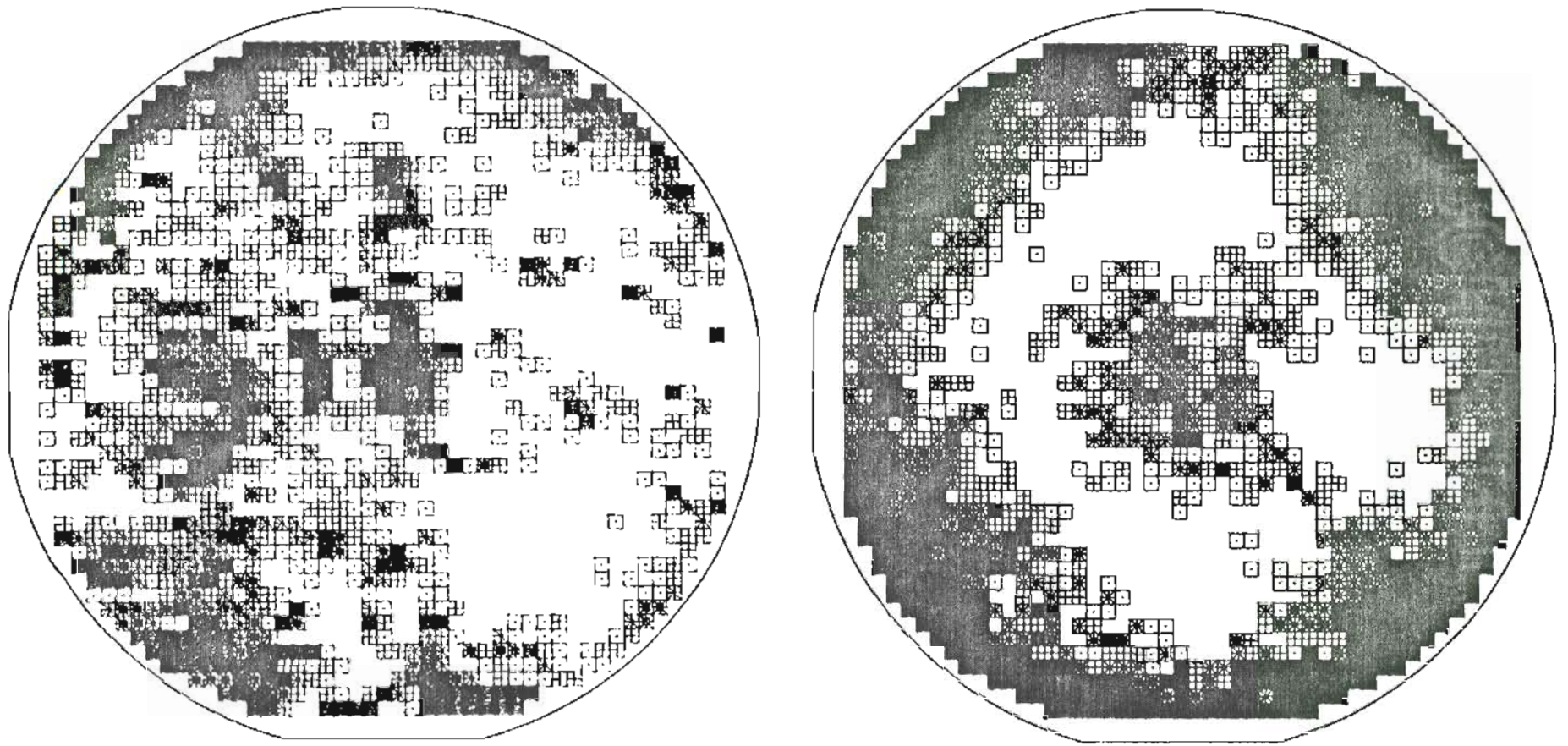


Figure 3-24: Dislocation (left) and EL2 (right) maps of the same sample. The EL2 concentration is symmetrically distributed, despite the lack of similar symmetry in the dislocation pattern.

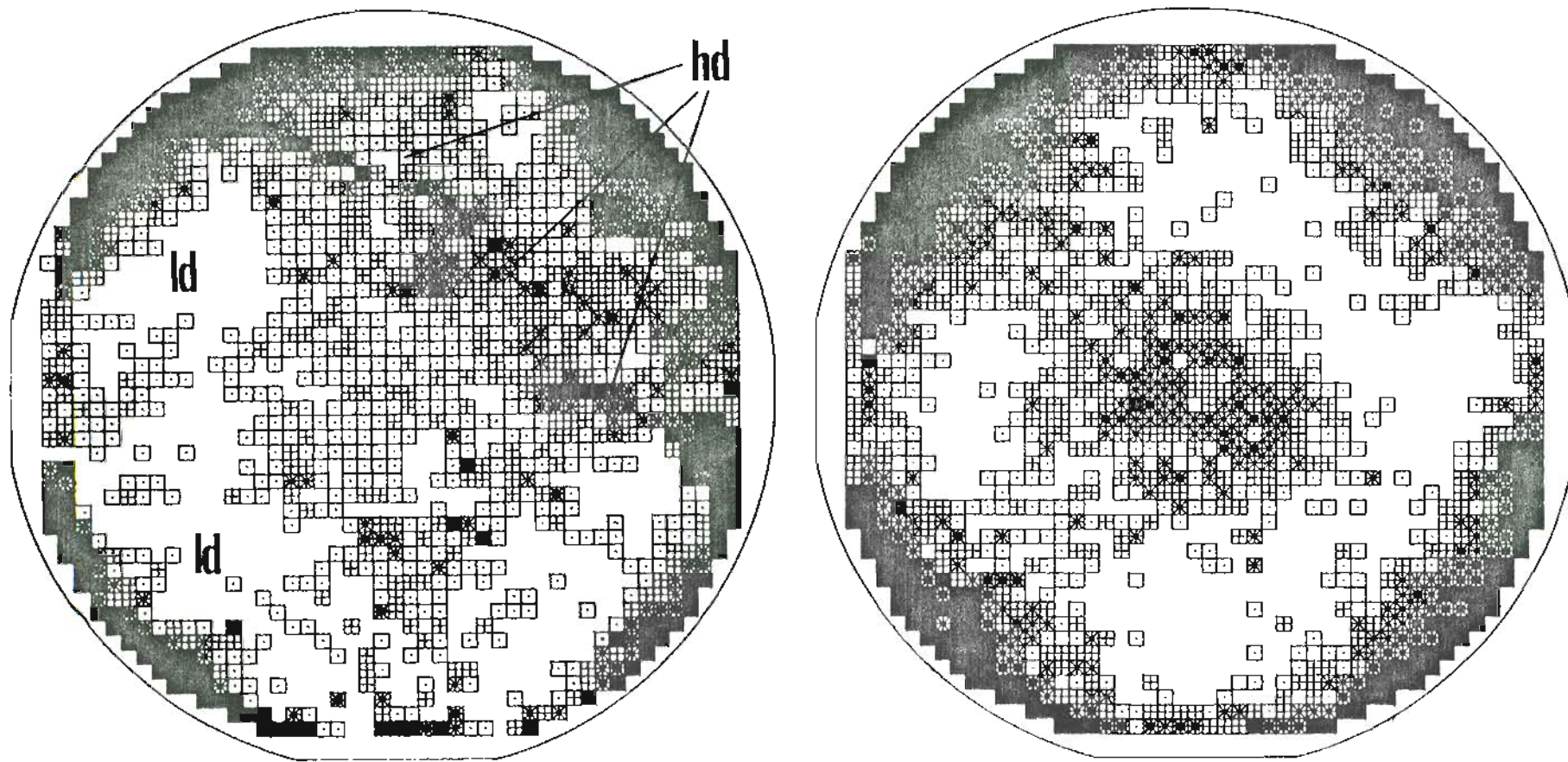


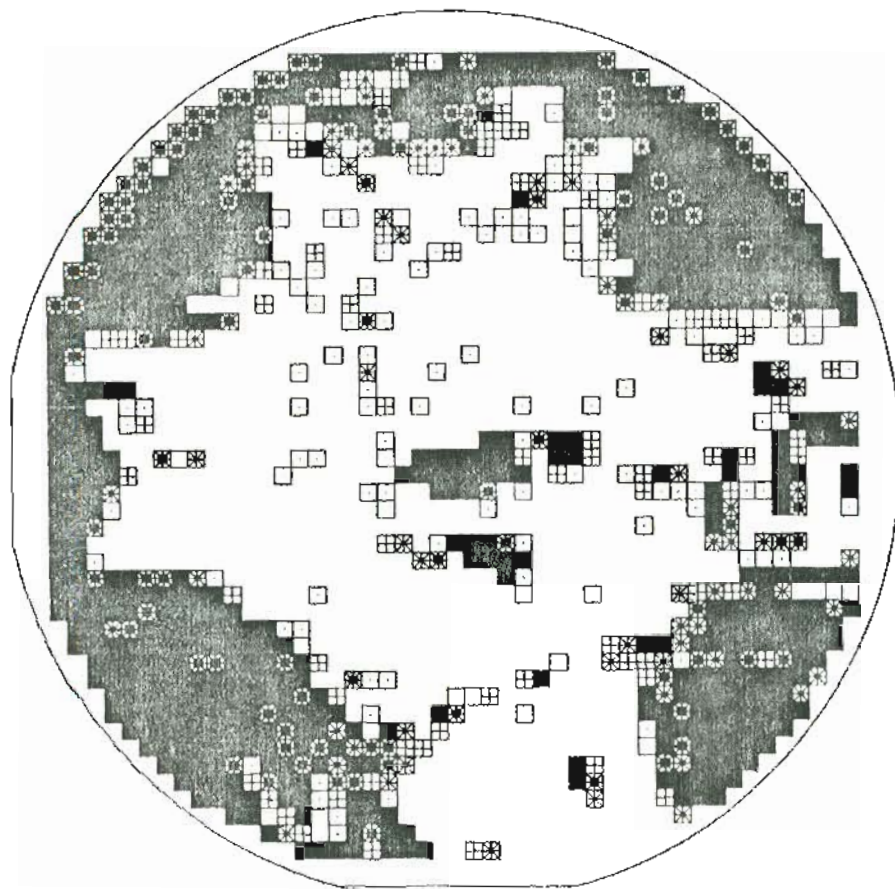
Figure 3-25: Dislocation (left) and EL2 (right) distributions. Low dislocation areas (ld) correspond to high EL2 regions, and vice versa.

thermodynamic equilibrium concentration can provide a small correction to the the main concentration, and is further weakened by the noncorrelation between EL2 and dislocations evidenced in previous samples.

The interpretation we offer for these In-doped wafers is as follows: insofar as EL2 is somewhat connected to the As_{Ga} antisite defect, indium (being isoelectronic to gallium) is effectively competing with arsenic in occupying gallium vacancies, precursors to the antisite defect. As a result a smaller number of antisite defects is able to form, and the average EL2 concentration is lowered.

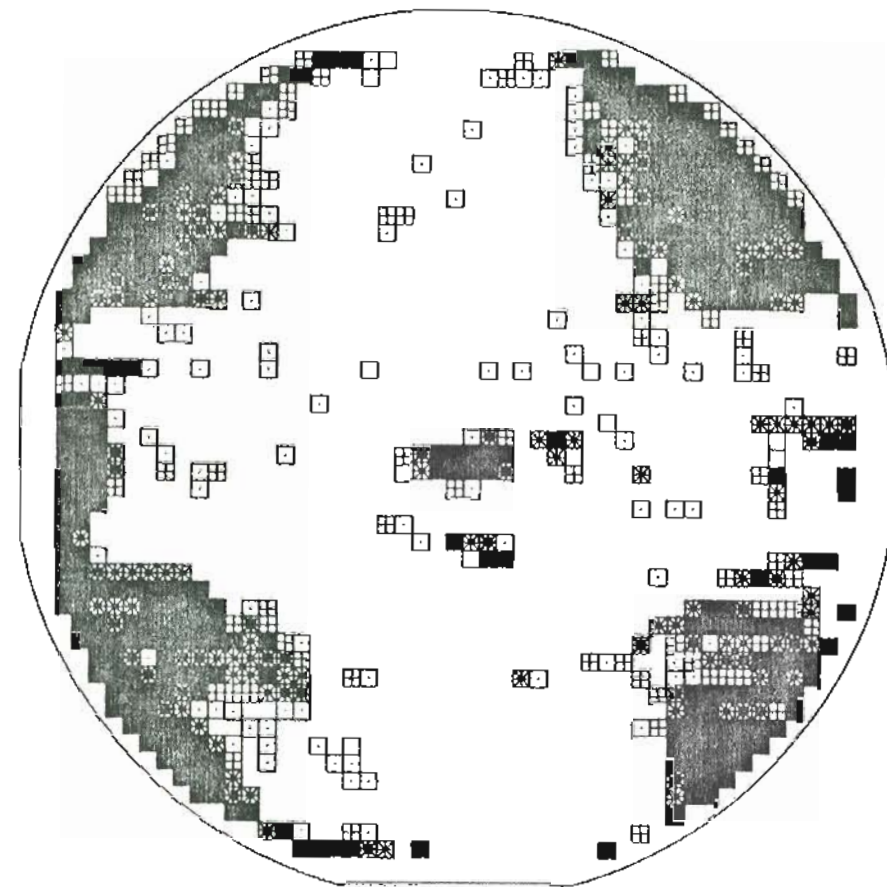
In conclusion, a unified picture of the behavior of EL2 in LEC GaAs does not clearly emerge from our data. Three regimes can be nevertheless identified: EL2 distributions without recognizable pattern, EL2 distributions with four-fold symmetry, that do not appear to be especially connected to stress and dislocation patterns, and radial EL2 distributions. While the last one can be explained by the effect of the temperature profile in the growing ingot, the four-fold EL2 distribution appears to be likely controlled by parameters other than dislocations and/or stress.

Possible candidates for a controlling role are



8 LEVEL SCALE, STEP = .025 cm⁻¹

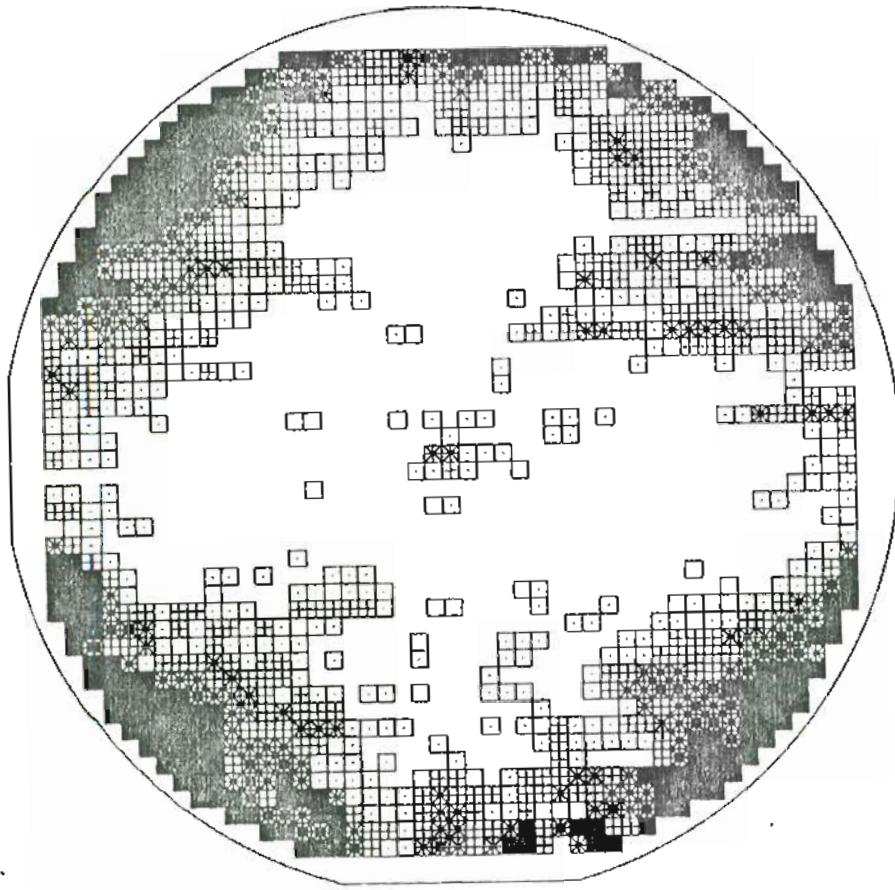
- ABS. COEFF. < .4 cm⁻¹ EL2 < 2.85E15 cm⁻³
- ABS. COEFF. > .5 cm⁻¹ EL2 > 3.57E15 cm⁻³



8 LEVEL SCALE, STEP = .04 cm⁻¹

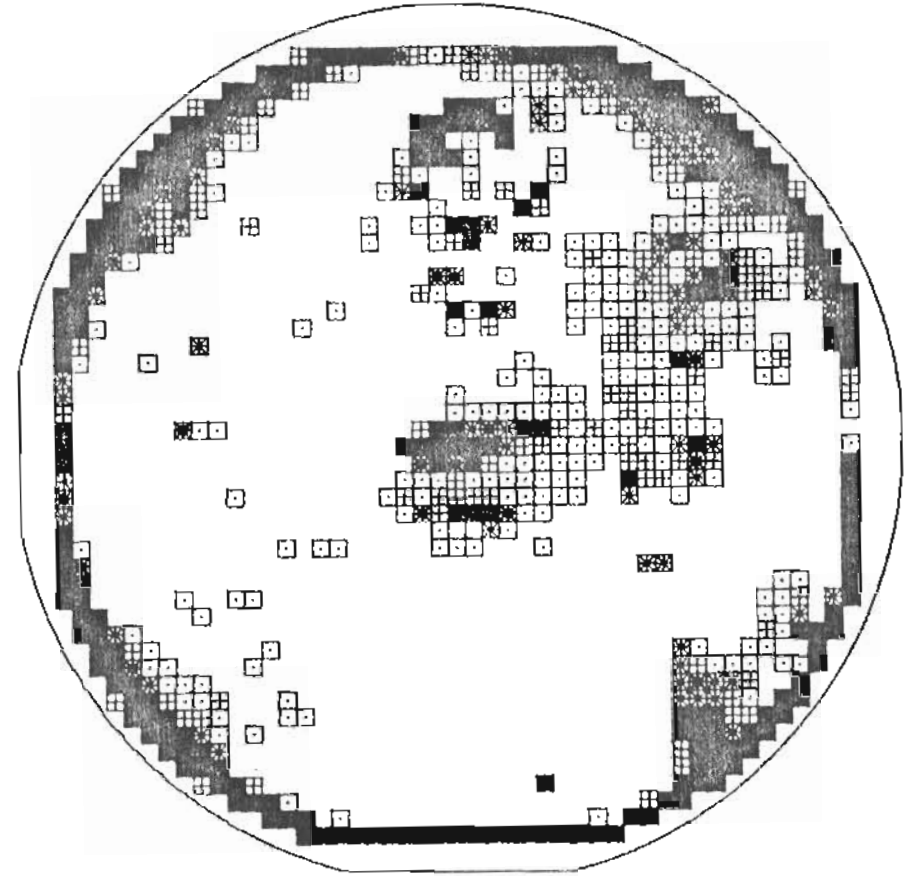
- ABS. COEFF. < .56 cm⁻¹ EL2 < 4E15 cm⁻³
- ABS. COEFF. > .72 cm⁻¹ EL2 > 5.14E15 cm⁻³

Figure 3-26: Two 2" In-doped wafers from the same supplier, Showa Denko. Although N_{E12} is low, in both samples the four-fold symmetry can be recognized.



6 LEVEL SCALE, STEP =8E-03 cm-1

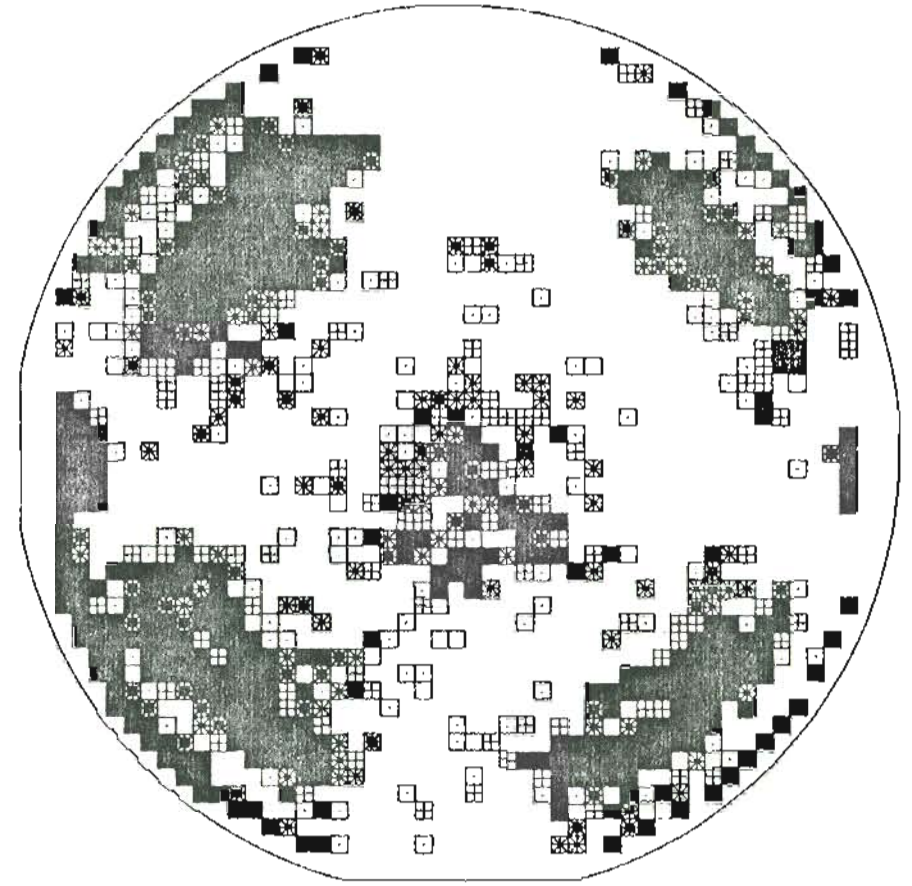
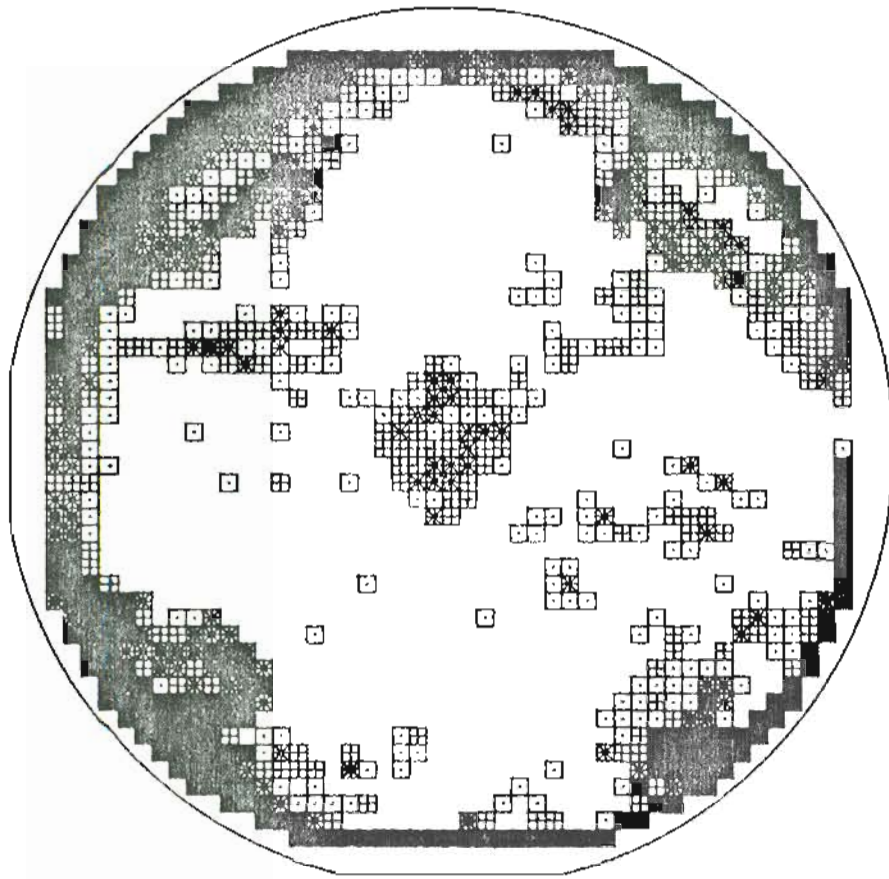
- ABS. COEFF. < .624 cm-1 EL2 <4.45E15 cm-3
- ABS. COEFF. > .656 cm-1 EL2 >4.60E15 cm-3



6 LEVEL SCALE, STEP =.05 cm-1

- ABS. COEFF. < .34 cm-1 EL2 <2.42E15 cm-3
- ABS. COEFF. > .54 cm-1 EL2 >3.85E15 cm-3

Figure 3-27: A 3" In-doped wafer, from Sumitomo (left) and an equally doped 2" wafer, from Showa Denko (right).



0 LEVEL SCALE. STEP =.04 cm⁻¹

□ ABS. COEFF. <.44 cm⁻¹ EL2 <3.14E15 cm⁻³
 ■ ABS. COEFF. >.8 cm⁻¹ EL2 >4.29E15 cm⁻³

0 LEVEL SCALE. STEP =.03 cm⁻¹

□ ABS. COEFF. <.72 cm⁻¹ EL2 <5.14E15 cm⁻³
 ■ ABS. COEFF. >.84 cm⁻¹ EL2 >8E15 cm⁻³

Figure 3-28: Two 2" In-doped wafer, from Showa Denko (left) and Furukawa (right). The four-fold symmetry is most evident in the sample at right, but note the ring of low EL2 at the edge of the wafer, where dislocations are usually numerous.

hydrodynamic flow patterns in the melt and particular segregation mechanisms at the growth interface, both possibly coupled with crystallographically dependent EL2 formation. Theoretical and experimental investigations of the melt movements in the Czochralski growth [13,14] have revealed a number of possible fluid configurations in the crucible, influenced by the crystal diameter and rotation rate, as well as by the crucible rotation. Nonmixing cells with different convective fluid movements exist in the crucible, and they are likely to affect the growth of the crystal, as well as the solid-liquid interface.

The distribution of dopants in GaAs has been shown to be nonuniform and incompatible with standard segregation theory [1,15]. The EL2 distribution could be affected by such anisotropic incorporation of impurities. Finally one of the suggested identification of EL2 [16], a double antisite defect, is preferably aligned along the [110] directions, an indication that the specific coupling of defects with the crystalline GaAs matrix could be responsible for its peculiar distribution in the (100) plane.

.

REFERENCES

1. D. E. Holmes, R. T. Chen, and J. Yang, Appl. Phys. Lett. 42, 419 (1983)
2. D. E. Holmes, R. T. Chen, K. R. Elliott, and C. G. Kirkpatrick, Appl. Phys. Lett. 43, 395 (1983)
3. D. J. Stirland and M. R. Brozel, in Microscopic Identification of Electronic Defects in Semiconductors, edited by N. M. Johnson, S. G. Bishop and G. D. Watkins, MRS Conf. Proc. Vol.46, 213 (1985)
4. A. S. Jordan, R. Caruso, and A. R. Von Neida, Bell Sys. Tech. J. 59, 593 (1980)
5. N. Kobayashi and T. Iwaki, J. Cryst. Growth 73,96 (1985)
6. G. Szabo, J. Cryst. Growth 73, 131 (1986)
7. H. Ehrenreich and J. P. Hirt, App. Phys. Lett. 46, 668 (1985)
8. S. Martin and M. Duseaux, in Defect Recognition and Image Processing in III-V Compounds, edited by J. P. Fillard (Elsevier, Amsterdam 1985), p. 287
9. K. R. Elliott, R. T. Chen, S. G. Greenbaum, and R. J. Wagner, in Semi-Insulating III-V Materials: Kah-nee-ta

- 1984, edited by D. C. Look and J. S. Blakemore (Shiva, Nantwich, UK, 1984), p. 239
10. T. Schroeder, private comm.
 11. D. E. Holmes, H. Kuwamoto, C. G. Kirkpatrick, and R. T. Chen, in Semi-Insulating III-V Materials: Kah-nee-ta 1984 edited by D. C. Look and J. S. Blakemore (Shiva, Nantwich, UK, 1984), p.204
 12. D. J. Stirland, M. R. Brozel, and I. Grant, Appl. Phys. Lett. 46, 1066 (1985)
 13. A. D. W. Jones, Progr. Crystal Growth and Charact. 9, 139 (1984)
 14. J. R. Carruthers and K. Nassau, J. Appl. Phys. 11, 5205 (1968)
 15. L. Jastrzebstri, J. Lagowski, W. Walukiewicz, and H. C. Gatos, J. Appl. Phys. 51, 2301 (1980)
 16. T. Figielski, E. Kaczmarek, and T. Wosinski, Appl. Phys. A 38, 253 (1985)

CHAPTER 4

EL2, DISLOCATIONS AND DEVICES

A. Introduction

Gallium arsenide FETs for integrated circuits are often fabricated by direct ion implantation into a SI substrate. This substrate typically comes from a crystal grown by the LEC method, and SI status derives from compensation of shallow acceptors by the midgap donor EL2.

The potentially important attributes for a SI wafer to be used for ICs may include the electrical resistivity and the activation energy, the EL2 concentration in its neutral (N^0) and ionized (N^+) states, as well as the density of dislocations N_d produced by thermal stress during post-growth cooling. How uniform the FET parameters will be across a wafer can be expected to show some correlation with the uniformity of the various substrate properties.

The interaction between dislocations and device behavior has been subject of many studies, with groups in

Japan describing an apparent shift of V_{th} with proximity to a dislocation. Miyazawa et al. [1] found V_{th} to be shifted by up to 300 mV for a FET in a SI LEC substrate when the nearest dislocation was only a few micrometers away. Less sensitivity of V_{th} to dislocation proximity was later reported for annealed wafers [2], and for indium-doped, low-dislocation SI GaAs [3]. In an independent study, however, Winston et al. [4] concluded that V_{th} was not directly influenced by dislocation proximity in their In-doped GaAs. Of course, the EL2 distribution was not known for the wafers used in the contrasting reports of Refs. 1 and 4, so that a discrimination between the effects of EL2 centers, of dislocations, or anything else on device properties was not possible from those works.

Capacitance spectroscopy measurements below the Schottky gate contact of a GaAs implanted/annealed FET often detect little EL2 near the top of the channel, due to outdiffusion [5], hydrogen passivation [6], etc., during the post implant anneal. However, EL2 is present further down in the channel, as evidenced by photo-FET [7] or side-gating [8] experiments which are sensitive to the channel-substrate interface. It is therefore pertinent to look for correlation

between the substrate neutral EL2 concentration N^0 and device parameters which depend in part on the channel-substrate interfacial space-charge density.

B. Experimental procedures and results

After the regular EL2 mapping, the wafers here considered were processed by Si^+ ion implantation, furnace capped anneal, etc. to form a device test pattern, including a square array on 1 mm centers of FETs with a 100 μm gate width and 3 μm source to drain spacing [9].

Following measurements of the threshold voltage and drain saturation current carried out at Tektronix, the wafers were etched in molten KOH, to reveal dislocation etch pits.

The pattern of Na so found for wafer No. 1 was a familiar one, with some lineage apparent along the [110] directions, larger values ($N_a = 7 \times 10^4 \text{ cm}^{-2}$) towards the edge along the four [100] directions, and the smallest values ($N_a = 2 \times 10^4 \text{ cm}^{-2}$) along [011] directions at about mid-distance from the center. The map of the saturation current I_{ds} of

FETs built in the same wafer can be seen in the lower left part of Fig. 4-1, while the upper part shows the dislocation configuration and the EL2 map is seen in the lower right part. The saturation current is measured in all the samples at $V_{gs} = 0$ and $V_{ds} = 1.5$ V, and in this particular wafer it was quite low, averaging only $3.0 \mu\text{A}$. Although the EL2 pattern is somewhat fuzzy, the same four-fold symmetry can be recognized in the maps composing Fig. 4-1.

The results for this wafer do not allow a conclusion as to whether FET channel conductance is affected by the proximity of a dislocation or by the local EL2 concentration. It is also clear that, depending on whether one only knows the dislocation pattern or the EL2 one, a good case can be made for either parameter as responsible for the non-uniformity of the FET properties.

In this respect the results for wafer No. 2 are more interesting. The infrared transmittance mapping had shown this wafer to have a radial N^0 pattern, with no azimuthal variations. As discussed in Chapter 3, this kind of EL2 distribution is fairly common in samples from the tail portion of an ingot.

On the contrary, the large dislocation density ($N_d = 10^5$

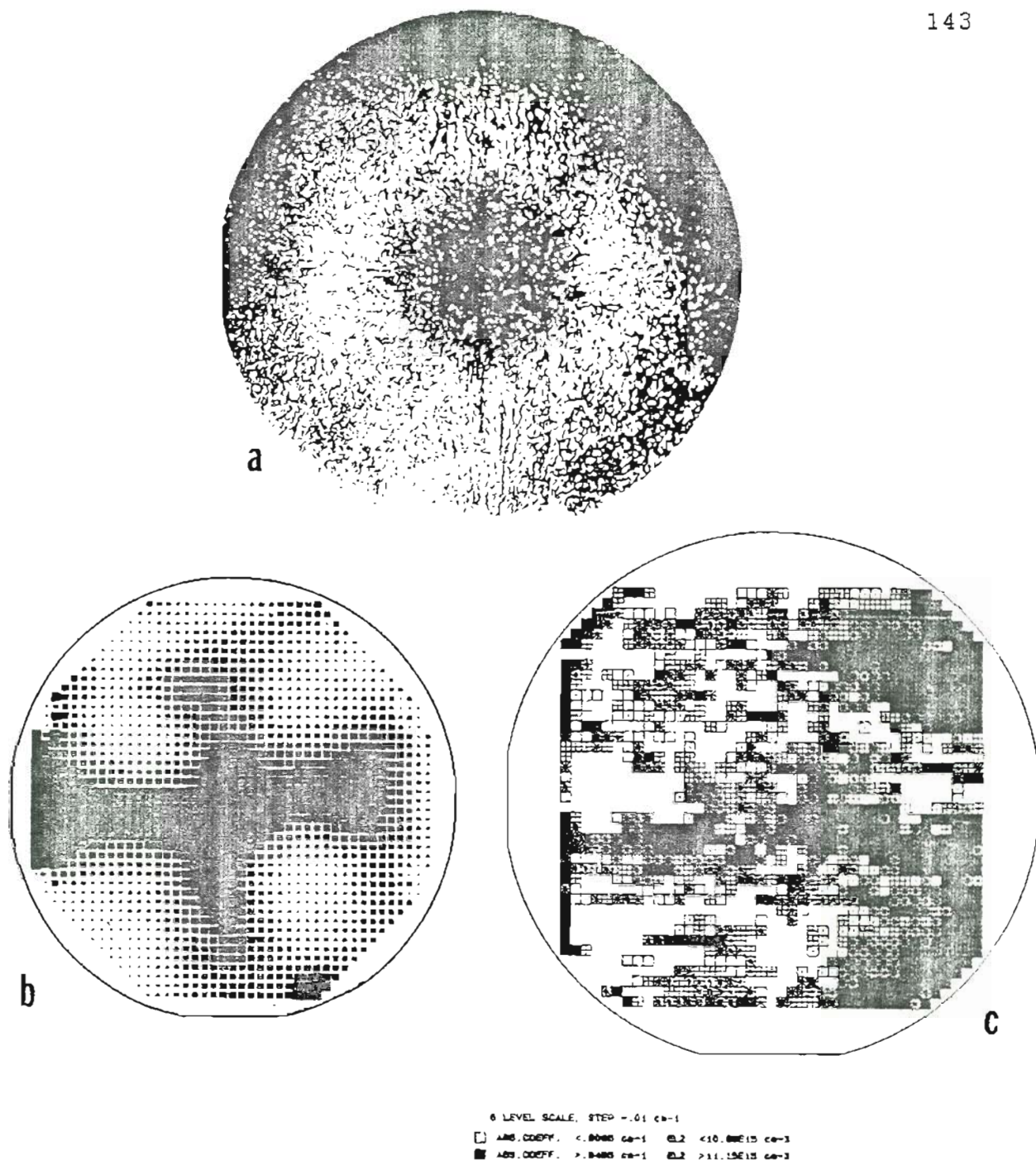


Figure 4-1: Set of measurements performed on wafer No. 1. (a): macrograph of the dislocation distribution; (b): map of the saturation current, with darker pixels corresponding to higher I_{ass} ; (c): EL2 map.

cm^{-2}) was essentially uniform, as evidenced by figure 4-2.

Mapping of the electrical characteristics of the devices built in this wafer clearly showed radially symmetric patterns of the device V_{th} and I_{ass} , shown in Fig. 4-3. I_{ass} increases with increasing EL2 concentration, and the threshold voltage becomes more negative (thus larger in absolute value) for locally higher EL2 concentration.

More quantitatively, the electrical data can be compared with EL2 by calculating the correlation between the two variables. Linear regression plots are shown in figures 4-4 for V_{th} and I_{ass} vs. EL2, respectively, for wafer No. 2. The correlation factor r deduced is slightly larger than 0.6. While this is not an extremely high value, the large number (ca. 1600) of experimental points implies a $> 99\%$ confidence level for the correlation. It is to be kept in mind, moreover, that points of the wafer that are considered to be the same in the process of calculating the correlation are such only approximately, because of the relative misalignment between "optical" and "electrical" grids.

An In-doped wafer has been subjected to the same set of measurements. In this wafer, though, In-doping did not appear to have been effective in "hardening" the lattice

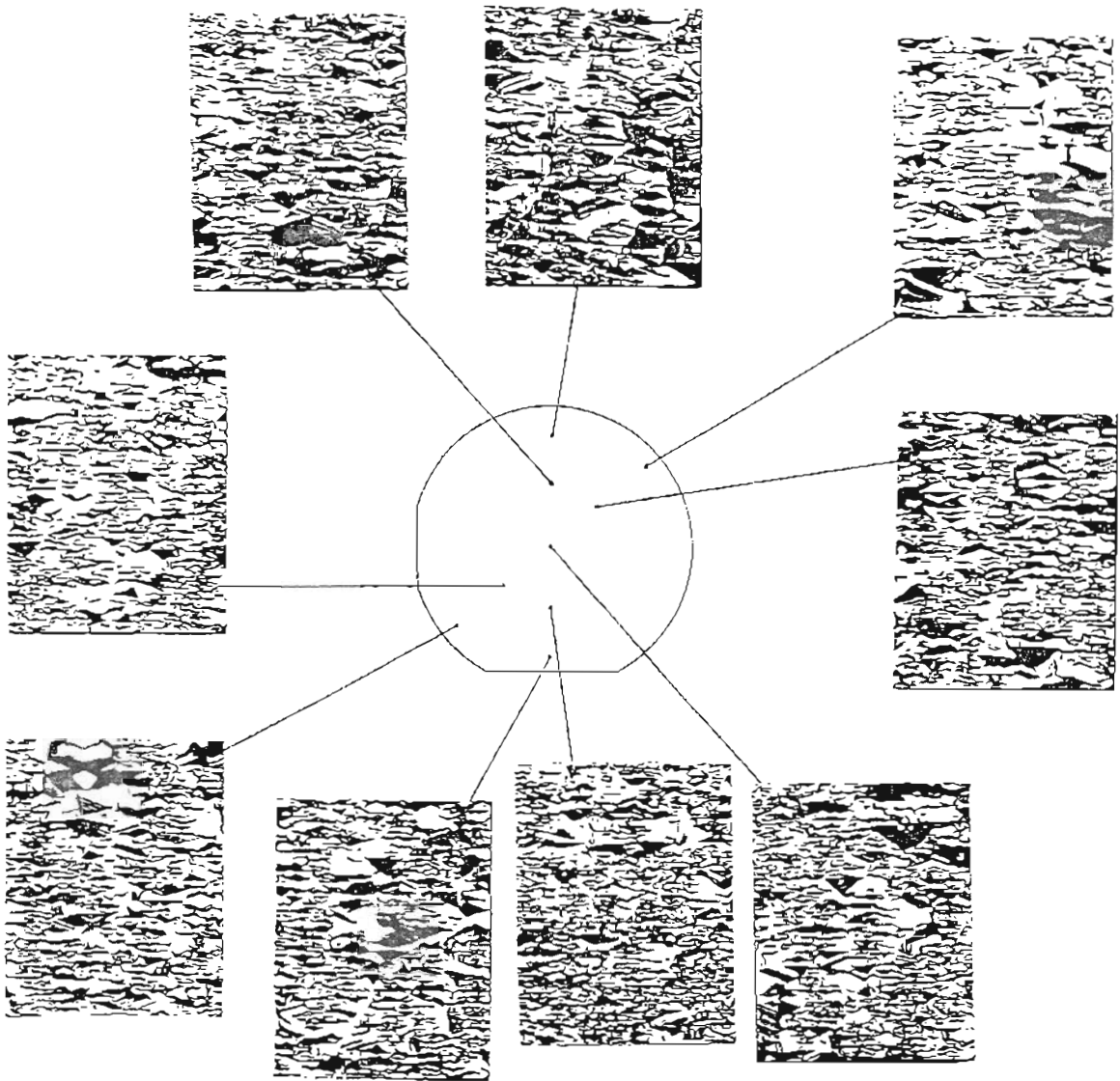


Figure 4-2: Micrographs shot at different points on wafer No. 2 indicate an essentially uniform dislocation pattern.

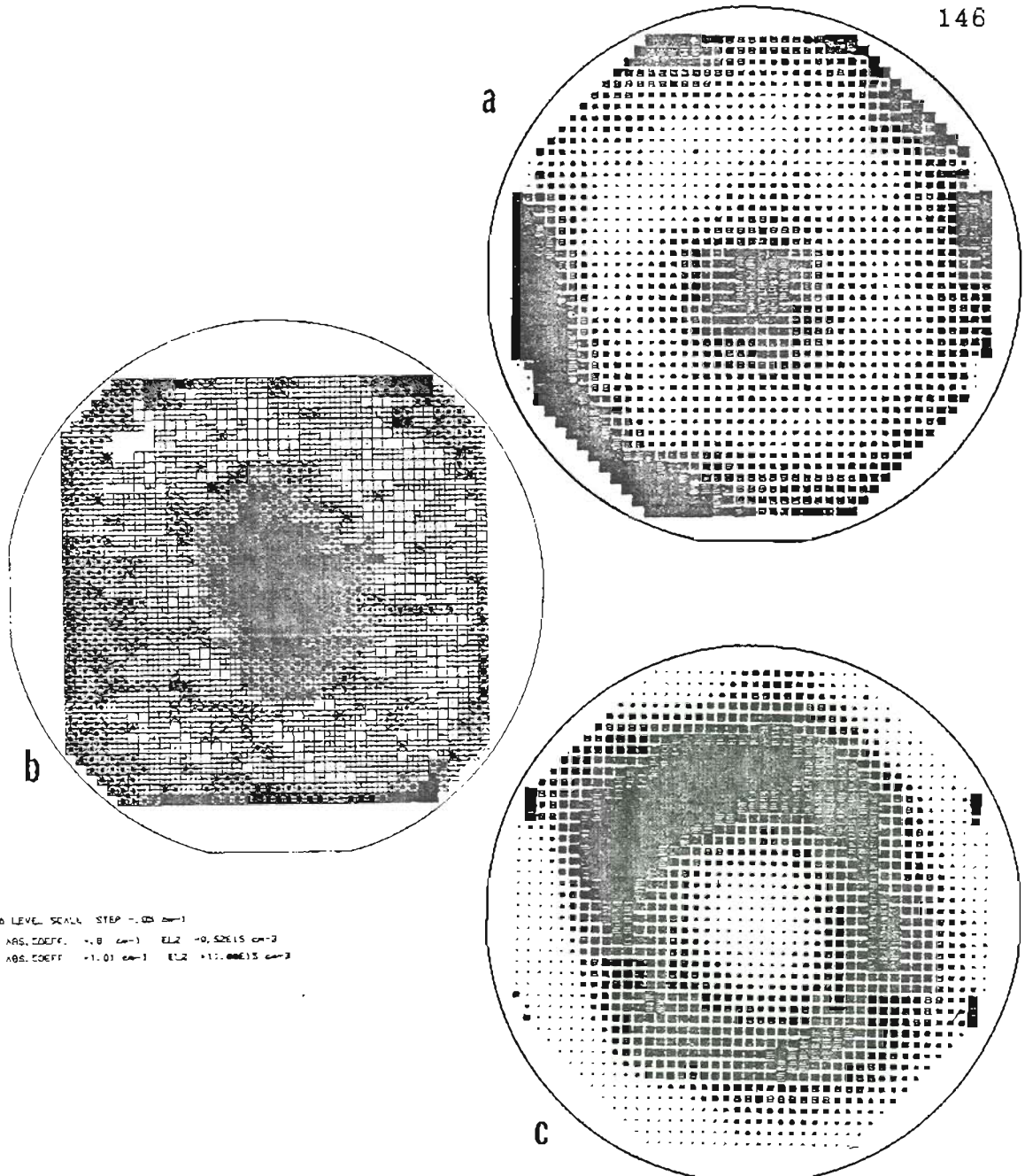


Figure 4-3: Measured performed on wafer No. 2. (a): saturation current map, I_{s} increasing with pixel shading; (b): EL2 map; (c): threshold voltage map, V_{th} larger for darker pixel shading.

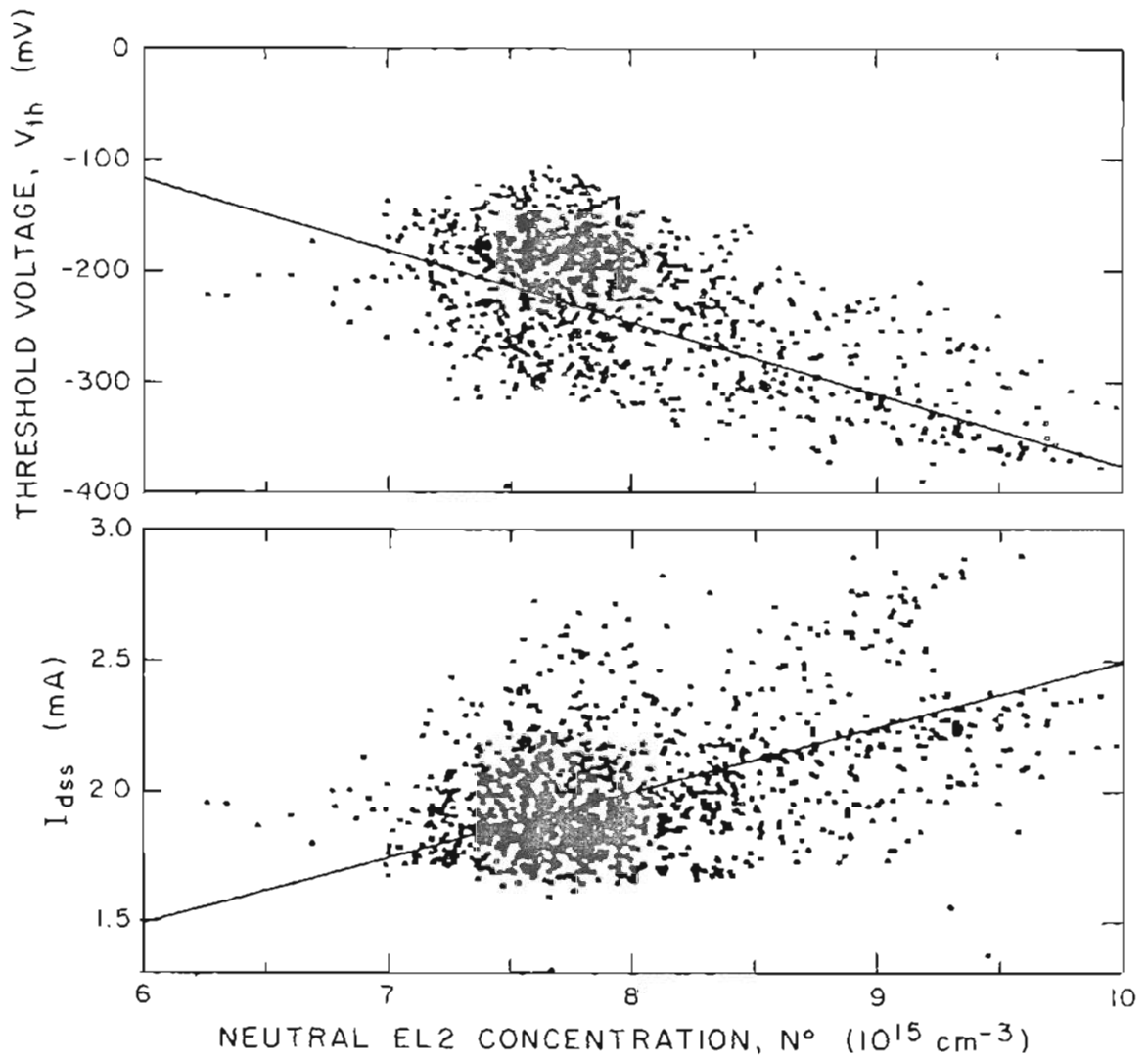
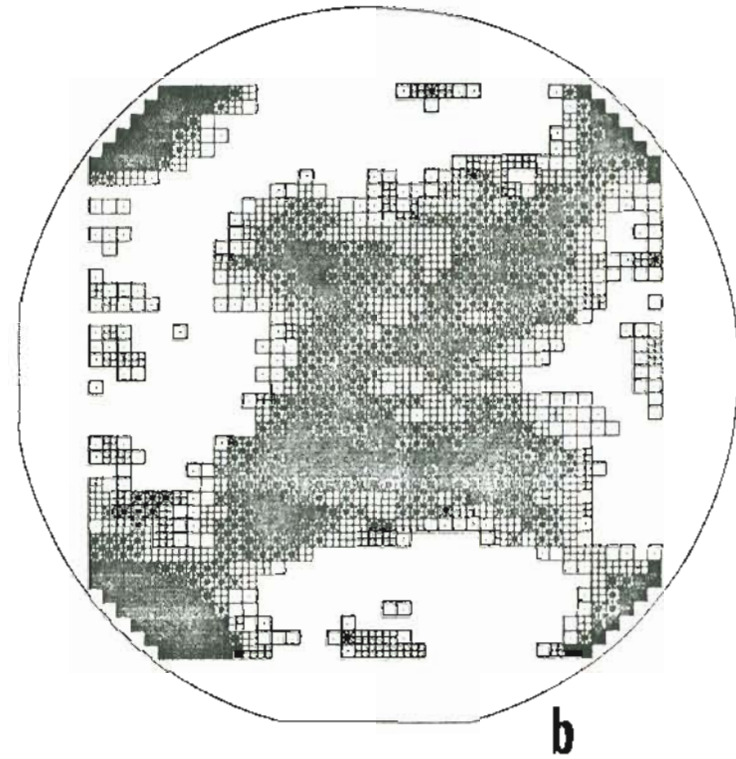
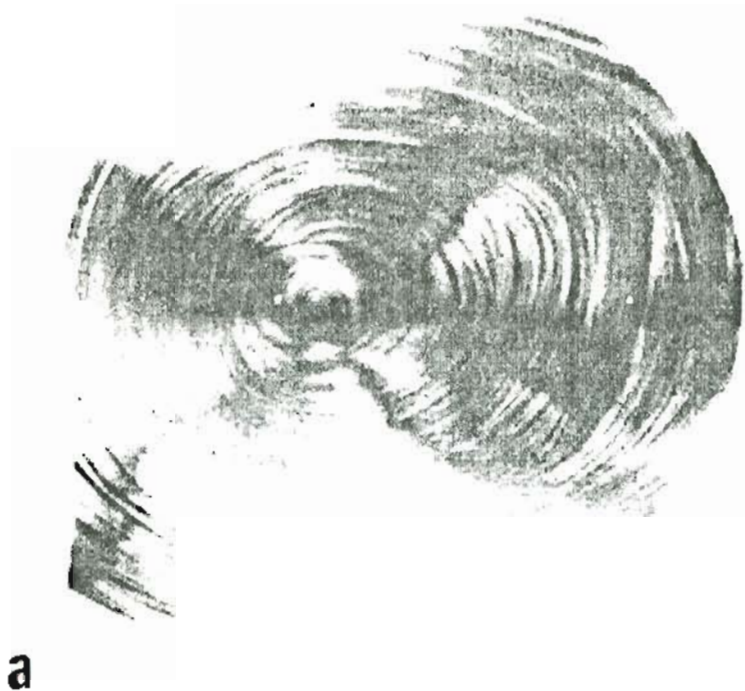


Figure 4-4: Correlation plot for wafer No. 2.

adequately against the generation of dislocations, since X-ray topography (Fig. 4-5, left) reveals a 4-fold pattern of dislocation density, including a central maximum. It is thus interesting to note that N^0 does not have a central maximum, as per figure 4-5, right. Yet the EL2 concentration is sharply peaked along the [110] directions, with a moderately low mean concentration of about 6×10^{15} centers per cubic centimeter. The variance of the EL2 concentration is high, at 30% of the mean value, providing a large range over which the effect of local variations can be correlated to the behavior of devices.

FETs were in fact implanted in a wafer immediately next to this one, with results, for V_{th} and I_{dss} , that can be seen in Fig. 4-6. The spatial features of the three distributions (EL2, V_{th} and I_{dss}) are closely matched, even in the asymmetries of the four [110]-oriented lobes of high N^0 and V_{th} . It is worth noting that the center of this wafer pair shows a lower N^0 and V_{th} , even though X-ray evidence indicates this area to have above average dislocation density. The correlation plot between V_{th} , N^0 can be seen in Fig. 4-7.



6 LEVEL SCALE, STEP = .07 ce^{-1}
□ ABS. COEFF. <.4 ce^{-1} EL2 <4.7E15 ce^{-3}
■ ABS. COEFF. >.68 ce^{-1} EL2 >7.99E15 ce^{-3}

Figure 4-5: X-ray tomograph (a) and EL2 map (b) of wafer No. 3. Dark bands in part (a) indicate strain.

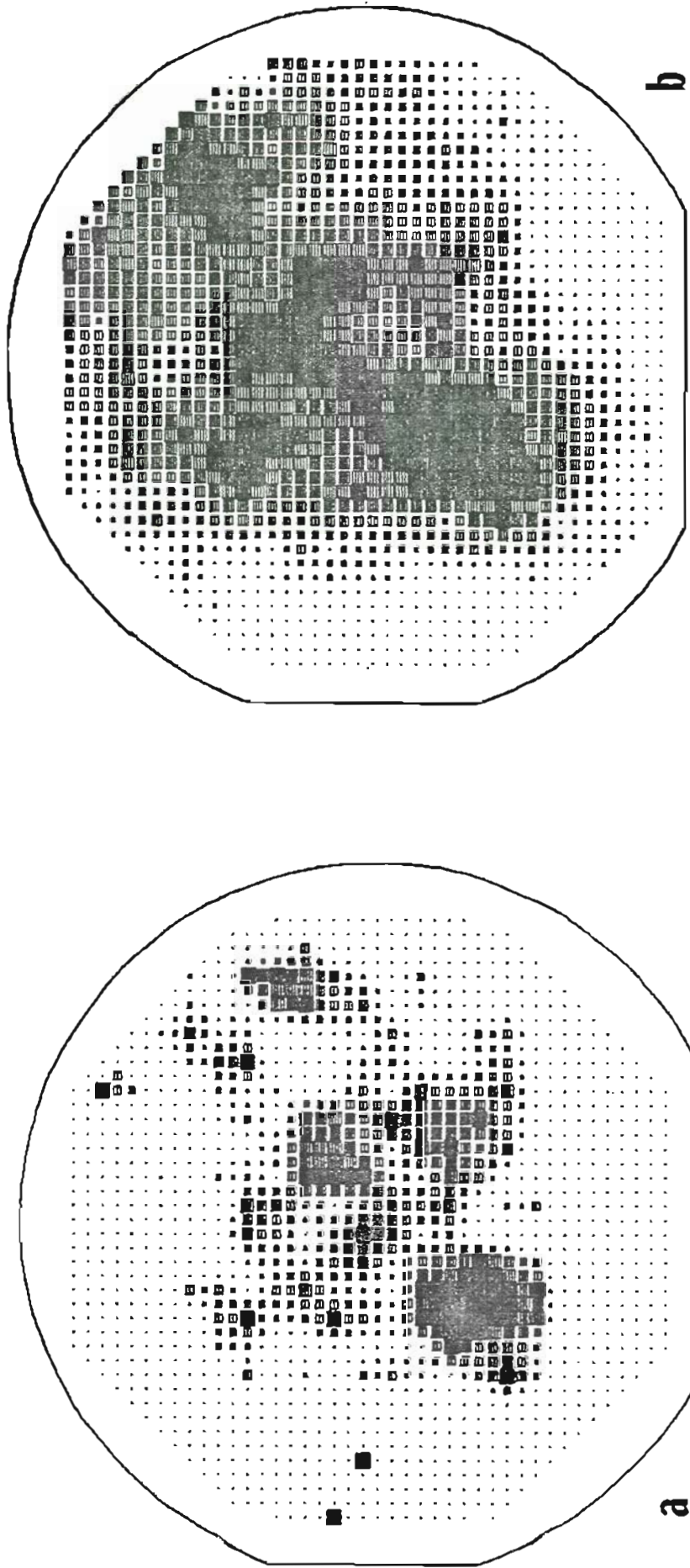


Figure 4-6: Threshold voltage (a) and saturation current (b) maps for wafer No. 3

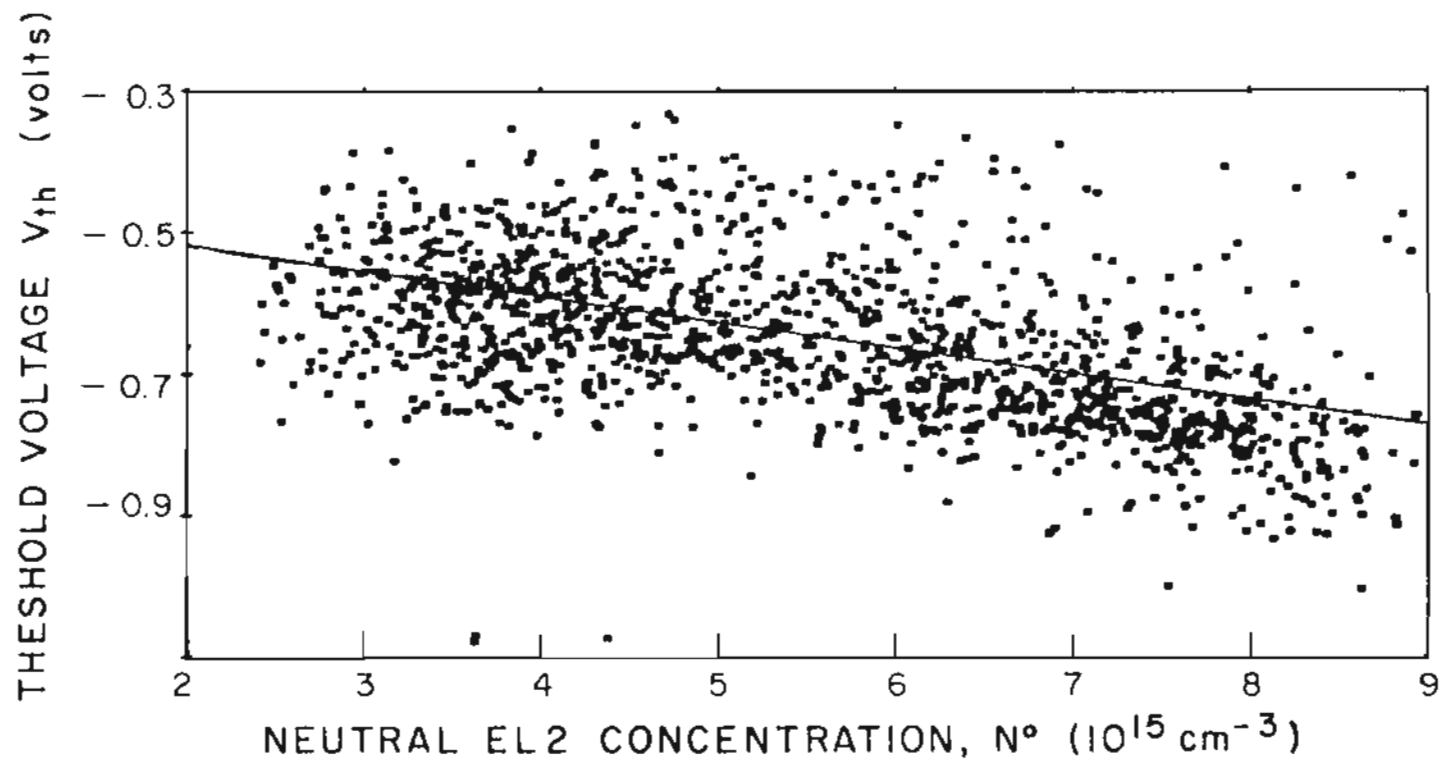


Figure 4-7: Correlation plot for results obtained in wafer No. 3.

C. Discussion

The works of references [1,3], supported by more recent results [10,11] which clearly show that the FET parameters change with proximity to dislocations, are too well documented to be dismissed.

Nevertheless, observations of this kind are phenomenological in nature, and a cause-effect relationship may be implied, but should not be taken for granted. On the same grounds, moreover, the insensitivity of stress parameters to proximity to dislocations has been reaffirmed [12].

If there is a correlation between V_{th} and local dislocation density, however, this connection does not necessarily work through a physical dependence of V_{th} on the distance to the nearest dislocation. Suppose that for some reason which will be elucidated later on, algebraically low values of V_{th} occur predominantly in high-dislocation regions, and high values in low-dislocation regions. In the high-dislocation region, the nearest pit will be closer to a device than in low-dislocation regions. As a result, low values of V_{th} will be statistically associated with short

distances to the nearest pit.

As for the physical mechanism responsible for changes in V_{th} , it is to be considered that conventional modeling of FET performances [10,13] provides an expression for the threshold voltage that is controlled, among other factors, by the net carrier concentration $(N_D - N_A)$ in the active layer:

$$V_{th} = \Phi_B - (E_c - E_f) - \frac{q}{2\epsilon} (N_D - N_A)t^2 \quad (1)$$

for a Schottky barrier height Φ_B , a difference between the the Fermi level E_f and the conduction band edge E_c in an active layer of thickness t .

Some considerations can be made considering only the effect of a variable N_D concentration across a substrate wafer:

- a) if V_{th} is on the average close to zero, it will become slightly negative (positive) for locally high (low) N_D ;
- b) for a mean V_{th} different from zero, a local concentration N_D above the average value will drive V_{th} algebraically smaller: that is, a negative V_{th} will get more negative, and an average positive threshold voltage will become smaller.

Clearly, we are implying here that a variable EL2 concentration is partially responsible for changes of the total Nd concentration. The problem is that in an n-type active layer EL2 should be in its neutral state, therefore not able to directly affect the electrical properties of the active layer. On the other hand, it is expected on the basis of thermodynamical considerations [14,15], that the presence of a locally high EL2 concentration reduces the concentration of arsenic vacancies, V_{As} . Since Si ions are amphoteric in the GaAs host lattice, Si on a Ga site (Si_{Ga}) becomes a shallow donor, and Si on an As site (Si_{As}) becomes an acceptor. Therefore a more negative V_{th} in regions of high EL2 results from a higher activation efficiency due to the $(Si_{Ga} - Si_{As})$ net donor concentration in the same part of the wafer.

These considerations are in good agreement with the results for wafers 2 and 3, where indeed locally high EL2 concentration is connected to more negative V_{th} , and I_{ass} shows the opposite trend. Wafer #1 on the contrary is not consistent with the others, but it is to be considered that the range of deviation of EL2 is quite small, and that the very small mean I_{ass} suggests that the FET production was

affected by processing problems.

Keeping in mind that regions of high EL2 concentration are often found in areas of high dislocation density, our results allow interpretation of all the reported results. The effect of proximity to a dislocation is regarded as a very likely coincidence, where the controlling parameter is the locally high EL2 concentration, while the apparent absence of this proximity effect in other samples is explained by assuming that in such wafers N^0 is so uniform that it cannot appreciably modify the device performances. Such an interpretation applies to results for the In-doped samples of Ref. 4, where the EL2 variance is algebraically smaller than in undoped wafers.

As far as the uniformity of devices in annealed substrates is concerned, again we know that thermal annealing can profoundly affect the EL2 distribution, and in the best cases it can make the EL2 distribution more uniform [16], while no corresponding effect is seen in the dislocation pattern [2,16].

It is finally worth noting an interesting work [17] where four samples of LEC SI substrates from different, unspecified suppliers were tested for correlation between

electrical properties and dislocations. Not to our surprise, the authors find that while two samples show a definite correlation between EPD and electrical parameters as mobility and resistivity, two other substrates do not show any such correlation. Is the EL2 distribution different within the four samples ?

REFERENCES

1. S. Miyazawa, Y. Ishii, S. Ishida, and Y. Nanishi, Appl. Phys. Lett. 43, 853 (1983)
2. Y. Ishii, S. Miyazawa, and S. Ishida, IEEE Trans. Electron. Devices ED-31, 800 (1984)
3. S. Miyazawa, T. Honda, Y. Ishii, and S. Ishida, Appl. Phys. Lett. 44, 410 (1984)
4. H. V. Winston, A. T. Hunter, H. M. Olsen, R. P. Brian, and R. E. Lee, in Semi-Insulating III-V Compounds: Kah-nee-ta 1984, edited by D. C. Look and J. S. Blakemore, (Shiva, 1984),
5. G. M. Martin and S. Makram-Ebeid, Physica B 116, 371 (1983)
6. J. Lagowski, M. Kaminska, J. M. Parsey, H. C. Gatos, and M. Lichtensteiger, Appl. Phys. Lett. 41, 1078 (1982)
7. W. B. Leigh, J. S. Blakemore, and R. Y. Koyama, J. Appl. Phys. 57, 2721 (1985)
8. W. B. Leigh, J. S. Blakemore, and R. Y. Koyama, IEEE Trans. Electron. Devices ED-32, September (1985)

9. A. Rode, A. McCamant, G. McCormack, and B. Vetanen, 1982 IEEE Electron. Device Meeting, San Francisco, Dec. 1982, p. 162
10. Y. Matsuoka, K. Ohwada, and M. Hirayama, IEEE Trans. El. Dev. ED-31, 1062 (1984)
11. Y. Nanishi, S. Miyazawa, and Y. Matsuoka, in Defect Recognition and Image Processing in III-V Compounds, edited by J. P. Fillard (Elsevier, Amsterdam, 1985), p. 225
12. H. V. Winston, A. T. Hunter, H. M. Olsen, R. P. Bryan, and R. E. Lee, Appl. Phys. Lett. 45, 447 (1984)
13. S. M. Sze, Physics of Semiconductors, (J. Wiley, New York, 1981)
14. J. Lagowski, H. C. Gatos, J. M. Parsey, K. Wada, M. Kaminska, and W. Walukiewicz, Appl. Phys. Lett. 40, 342 (1982)
15. S. Miyazawa and K. Wada, Appl. Phys. Lett. 48, 905 (1986)
16. S. Martin and M. Duseaux, in Defect Recognition and Image Processing in III-V Compounds, edited by J. P. Fillard (Elsevier, Amsterdam, 1985), p.287
17. A. Tamura and T. Onuma, Jpn. J. Appl. Phys. 24, 510 (1985)

CHAPTER 5

CONCLUSIONS

The principal goal of this work, the realization of a system capable of quantitatively mapping the EL2 concentration in thin GaAs wafers, has been fully achieved. While the interest in such mapping systems remains high, other researchers still find great difficulties in handling 0.5 mm thick wafers [1,2]. It is likely that this set-up will not remain alone in its mapping capabilities, but at the same time it is more than likely that the design of similarly good systems will be close to the one here developed.

The basic simplicity of this apparatus has not forbidden -and probably has helped- to extend its use in mapping other extrinsic parameters of LEC GaAs wafers. The

capability to map the dislocation distribution seems far from trivial, especially if the performances of the present system are compared to other systems [3], painfully designed only to provide dislocation maps.

To this author, the most interesting and exciting application of the transmittance mapping system has been the detection of low-visibility interferograms evidencing contours of constant stress. Together with the first direct verification of thermoelastic models [4-6] of stress generation in LEC pulled GaAs, our findings have contributed a clarification of stress-birefringence phenomena in this material, which had previously been badly misinterpreted [2,7,8].

As far as the mechanism responsible for the macroscopic EL2 distribution is concerned, many problems remain unsolved. While some gettering of EL2 around lineages of dislocations has been detected, the ensemble of our data does not support the hypothesis, often advertised as already proven [9,10], that enhanced EL2 concentration is spatially connected to individual dislocations. In fact our data suggest that the particular four-fold spatial distribution of EL2 in (100) plane perpendicular to the growth axis is

independent from other parameters, being detectable in samples whose dislocation and stress distributions do not show the same symmetry.

We believe that other mechanisms, such as hydrodynamic flow in the melt or some specific segregation process, as well as intrinsic properties of GaAs, are more likely candidates to the controlling role for the large scale EL2 distribution.

At the time of this writing the microscopic identity of EL2 remains as unclear as it was almost three years ago; the results here reported do not specifically support the identification of EL2 with the arsenic antisite defect [11], since that hypothesis is mostly based on the occurrence of EL2 at dislocation sites. Nevertheless, the antisite defect could be produced independently from dislocations, and in this sense our results do not exclude such identification.

Regarding the relative effect of dislocations and EL2 on device performances, it appears likely that the effect of dislocations [12,13] has been overestimated. Some evidence of an effect of EL2 alone on the FET threshold voltage and saturation current has been found in this work, but a definitive answer to the question of what controls the

uniformity of devices built on SI GaAs substrates cannot be given due to limited number of wafers that have been processed to yield FET arrays on EL2 characterized substrates.

REFERENCES

1. J. Windscheif, M. Baeumler, and U. Kauffmann, *Appl. Phys. Lett.* 46, 651 (1985)
2. T. Katsumata and T. Fukuda, *Rev. Sci. Instrum.* 58, 202 (1986)
3. N. Toyoda, Y. Aota, and N. Takahashi, in Defect Recognition and Image Processing in III-V Compounds, edited by J. P. Fillard (Elsevier, Amsterdam, 1985), p. 141
4. A. S. Jordan, R. Caruso, and A. R. Von Neida, *Bell Syst. Tech. J.* 59, 593 (1980)
5. N. Kobayashi and T. Iwaki, *J. Crystal Growth* 73, 96 (1985)
6. G. Szabo, *J. Crystal Growth* 73, 131 (1985)
7. M. Yamada, *Appl. Phys. Lett.* 47, 365 (1985)
8. C. R. Elliott, D. L. Murrell, M. H. Lyons, and B. H. Conen, in Defect Recognition and Image Processing in III-V Compounds, edited by J. P. Fillard (Elsevier, Amsterdam, 1985), p. 87
9. D. J. Stirland and M. R. Brozel, in Symposium on the

- Microscopic Identification of Electronic Defects, (MRS, Pittsburgh, PA, 1985), p. 213
10. D. J. Stirland, M. R. Brozel, and I. Grant, Appl. Phys. Lett. 46, 1066 (1985)
 11. E. R. Weber, H. Ennen, U. Kaufmann, J. Windschief, J. Schneider, and T. Wosinski, J. Appl. Phys. 53, 6140 (1983)
 12. S. Miyazawa, Y. Ishii, S. Ishida, and Y. Nanishi, Appl. Phys. Lett. 43, 853 (1983)
 13. Y. Nanishi, S. Miyazawa, and Y. Matsuoka, in Defect Recognition and Image Processing in III-V Compounds, edited by J. P. Fillard (Elsevier, Amsterdam, 1985), p. 225

VITA

Paolo Dobrilla was born in Trieste, Italy, on May 1, 1956, and received a doctoral degree in Physics (Laurea in Fisica) from the University of Milano in 1980. He worked three years at Italtel Spa., expanding his dissertation work on AlGaAs laser diodes. In late 1983 the author began his study on nondestructive characterization of semi-insulating GaAs at the Oregon Graduate Center, presenting first meaningful results at the Conference on Semi-Insulating III-V Compounds held in Kah-nee-ta in April 1984.

In the course of the dissertation project the author has been a consultant for Varian Associates, providing the know-how to set up a mapping system similar to the one developed at OGC. Publications by the author are:

P. Dobrilla and J. S. Blakemore. "Experimental requirements for quantitative mapping of midgap flaw concentration in semi-insulating GaAs wafers by measurement of near-infrared absorption", J. Appl. Phys. 58, 208 (1985)

J. S. Blakemore and P. Dobrilla, "Factors affecting the spatial distribution of the principal midgap donor in semi-insulating GaAs wafers", J. Appl. Phys. 58, 204 (1985)

P. Dobrilla, J. S. Blakemore, A. J. McCamant, K. R. Gleason, and R. Y. Koyama, "GaAs field-effect transistor properties, as influenced by the local concentration of midgap native donors and dislocations", Appl. Phys. Lett. 47, 602 (1985)

P. Dobrilla, "A simple technique to evaluate the density of etch pits in GaAs", Materials Lett. 3, 299 (1985)

P. Dobrilla, "A vapor-phase KOH dislocation etch for GaAs", Materials Lett. 4, 17 (1985)

P. Dobrilla and J. S. Blakemore, "Optical mapping of residual stress in Czochralski grown GaAs", to be published in the May 12, 1986 issue of Appl. Phys. Lett.

P. Dobrilla and J. S. Blakemore, "Distributions of residual stress, dislocations, and EL2 in Czochralski grown semi-insulating GaAs", to be published in the July 1, 1986 issue of J. Appl. Phys.

The author has contributed papers at the following conferences and meetings:

3rd International Conference on Semi-Insulating III-V Materials: Kah-nee-ta 1984

Mat. Res. Soc. Spring Meeting: San Francisco 1985

5th International Conference on Deep-Level Impurities in Semiconductors: St. Andrews 1985

Defect Recognition and Image Processing in III-V Compounds: Montpellier 1985

Mat. Res. Soc. Spring Meeting: Palo Alto 1986

4th International Conference on Semi-Insulating III-V Materials: Hakone 1986

The Electrochemical Soc. Spring Meeting: Boston 1986